CHARACTERIZATION AND OPTIMIZATION OF GEOMETRICAL ACCURACY AND MECHANICAL PROPERTIES OF SPECIMENS PREPARED BY FUSED FILAMENT FABRICATION

by

Lichen Fang

A dissertation submitted to Johns Hopkins University in conformity with the requirements for the degree of Doctor of Philosophy

Baltimore, Maryland
April 2020

© 2020 Lichen Fang
All rights reserved

Abstract

Fused filament fabrication (FFF), also known as fused deposition modeling (FDM), is one of the most popular additive manufacturing processes. This low-cost technology gives more flexibility in designing complex three-dimensional (3D) structures and allows users to easily transform digital designs into physical items. However, advanced applications of FFF are still limited by the large variability of mechanical property and structural geometry of printed parts. It has been known that those printing qualities are highly dependent on the processing parameters, including layer height, print speed, nozzle temperature as well as environmental factors like chamber temperature and relative humidity. Still, there is a lack of fundamental understanding of those effects.

To address this knowledge gap, we used X-ray micro-computed tomography (micro-CT) to perform full 3D geometrical characterizations on printed Polycarbonate specimens with different printing parameters. The results showed significant geometry variations depending on different printing conditions. We demonstrated the effects of reducing layer height, increasing nozzle temperature, as well as compensating material extrusion rate to improve geometric precision to a minimum of 0.8 % deviation compared to the original digital design.

In addition to geometry variations, the environmental conditions could introduce multiple printing defects. In-situ infrared imaging analysis revealed the presence of up to 5 °C/mm thermal gradient when printing using an open-chamber printer and a heated build

plate. Further experiments showed that this undesirable thermal gradient, as well as the corresponding warping defects, can be mitigated by adding a closed chamber and elevating the chamber (environmental) temperature. Regarding the environmental humidity, analysis of micro-CT scans showed up to 11.7 % porosity, which is caused by polymer water content absorbed from environmental moisture. Meanwhile, tensile tests showed the mechanical strength loss associated with those defects. Further experiments showed that this undesirable porosity could be minimized by drying filaments before printing and printing in a dry environment.

We also conducted numerical studies by using finite element analysis based on material properties and CT-scanned geometries and found that the numerical model can accurately capture the modulus change brought by geometrical variations. Inspired by that, an empirical method is proposed to estimate the effective elastic modulus of the printed specimen.

This study serves as a guideline for future FFF characterization and optimization, demonstrating a method of how to obtain the modulus of FFF specimens and improve both mechanical performance and geometrical accuracy by parameter selections. Meanwhile, the findings about environmental factors can help to enhance printing quality when applied in various locations and weather conditions. Furthermore, our experimental efforts can be integrated with advanced thermo-mechanical computational models to provide insight into the FFF process.

Advisor: Professor Sung Hoon Kang

Readers: Professor Kevin J. Hemker and Dr. Jonathan E. Seppala

Acknowledgments

To me, scientific research has never been a lonely pathway. Numerous people have helped me, enlightened me, and encouraged me during the five-year journey. Here I would like to express my sincere gratitude to all those people:

Firstly, Professor Sung Hoon Kang, who has always been a great advisor and a great friend since the time we met in 2014. Back at that time, I was still a naïve senior undergrad who just had a first glance at science. Over these years, his guidance equipped me with knowledge; his curiosity pointed/guided me to the direction I shall proceed, and his kindness and optimism empowered me to overcome all the obstacles along the way. Outside the lab, he dedicatedly supported my career development and provided me with countless opportunities to interact with the professional communities. It is my great honor and pleasure to work together with Prof. Kang. I am very grateful that I could have you as my advisor, thank you!

Next, I would like to appreciate my committee members, Professor Kevin J. Hemker and Dr. Jonathan E. Seppala. They have provided tremendous help to my research; without them, I will never be able to finish this thesis. I would also like to thank other faculties within our big research project: Professor Thao D. Nguyen, Professor Mark Robbins, and Professor Peter Olmsted. From their helpful comments, my approaches are clarified, and my works are polished.

I want to thank all my collaborators: Dr. Jing Li, Mr. Ojaswi Agarwal, Mr. Zheliang Wang, Mr. Shuyang Chen, Mr. Marco Galvani Cunha, Dr. Ozan Erol, Dr. Santiago Orrego, and Dr. Seung-Yeol Jeon. Cheers for all the achievements we have made! I also want to thank my mentees, Ms. Yishu Yan, Ms. Shengyu Yao, Mr. Shaoyang Qu, and Mr. Zeyu Zhu. Together we learned from each other and made all the things happen.

I appreciate all the people who have helped me with the experimental facilities. I would like to thank Prof. Stavros Gaitanaros and Ms. Sirui Bi for allowing us to use their micro-CT machine; Prof. Ryan Hurley and Dr. Chongpu Zhai for providing help on humidity control equipment; Dr. Luoning Ma, Mr. Hao Sheng, and Mr. Bohan Sun for assistance with SEM imaging; and STEGO, Inc. for donating the space heater.

Labmates and friends are also essential parts of an enjoyable and fruitful Ph.D. life. Thanks to those wonderful people, who have shined into my journey: Dr. Jiayu Liu, Mr. Xiangyu Sun, Mr. Liujiang Yan, Ms. Bo Yuan, Mr. Yancheng Du, Mr. Bohan Wang, Mr. Peisheng He, Mr. Yitao Chen, Mr. Emilio Bachtiar, Ms. Shangtong Li, Mr. Junjie Pan, Mr. Boliang Wu, Ms. Urszula Krekora, Mr. Khalid Elawad, Mr. Daniel Wang, Mr. Decheng Hou, Mr. Shichen Xu, Mr. Adebayo Eisape, Ms. Beijun Shen, Ms. Runhan Tao, Mr. Zhezhi Chen, Dr. Shu Guo Dr. Ugur Erturun, Dr. Sicong Shan, Mr. Nan Xue, Mr. Zizhang Hu, and Mr. Hongtao Xue.

A special thank is given to my funding agencies, the Johns Hopkins Whiting School of Engineering (start-up fund), and the National Science Foundation (DMREF-1628974).

Finally, this thesis is dedicated to my parents, Shunshui Fang and Xiaodan Zhang, and my girlfriend, Ruisu Chen. Your love is the dawn appearing at the horizon, piercing all the darkness over the sky.

Contents

List of Tables

List of Figures

Chapter 1 : Introduction

This chapter provides the objectives of this work and a review of the development and advances of fused filament fabrication (FFF) processes. Attentions are given to the previous studies of characterizing and improving FFF quality by changing processing parameters and environmental conditions. At the end of this chapter, the organization of this thesis is introduced.

1.1 Motivation

Additive manufacturing (AM) represents a revolution in fabrication methodology. After thousands of years of manufacturing goods by cutting excessive materials off or pouring melts into molds, scientists and dreamers started to think about another way: what if we can put materials at arbitrary locations and add them up? In 1974, Dr. David E. H. Jones firstly discussed the possibility of using lasers to selectively cure photopolymers and form arbitrary three-dimensional (3D) shapes [1]. Later in the early 1980s, this concept came true. Pioneers like Hideo Kodama, Bill Masters, and Chuck Hull, started to build early prototypes of stereolithography 3D printers [2]–[4]. Since then, multiple AM approaches were developed and commercialized, several most famous examples and their mechanisms are summarized in Figure 1.1, including powder bed fusion, which is driven by laser melting; fused deposition modeling (FDM), which heats and liquefies materials for deposition; binder jetting, which injects glues to join the powder-form materials; etc.

[5]. After twenty years of development, the early patent for FDM expired in 2009, and numerous companies started to sell their FDM-mechanism printers, but under another name: fused filament fabrication (FFF) [6] to avoid trademark issues.

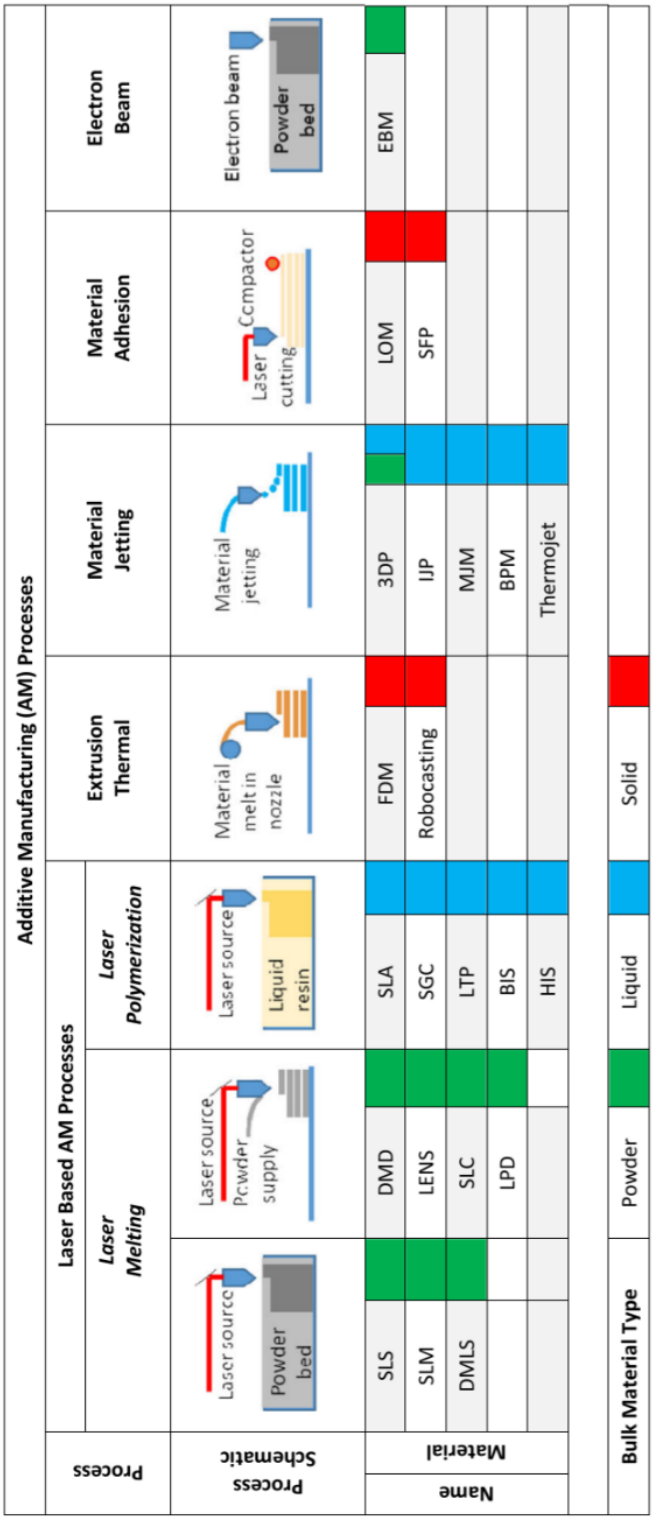

Figure 1.1: Additive manufacturing process categorization, reproduced from [5], use permitted under the Creative Commons Attribution License CC BY.

Among the various AM methods, FFF is one of the most popular processes [7]. The underlying mechanism and setup of FFF is shown in Figure 1.2, which melts and extrudes filament material to weld with previously deposited material and form 3D shapes. FFF's low cost and straightforward operation significantly lowers the bar for both professionals and nonprofessionals to manufacture prototypes, compared with using traditional manufacturing methods that generally require extensive training, expensive equipment, and long lead times due to fabrication of casting molds, etc. [8]. However, the quality of FFF produced products are generally inferior to those of traditional manufacturing methods and heavily influenced by multiple processing parameters [9], which further limits more structural applications of this technology [10].

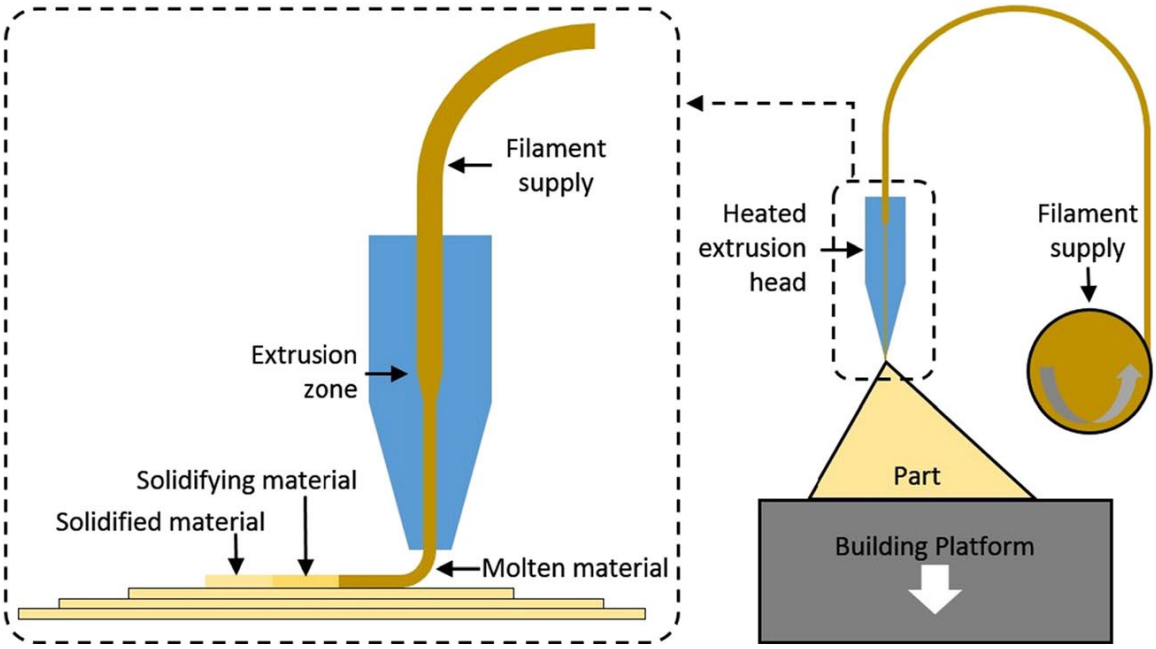

Figure 1.2: Schematic of FFF systems, reproduced from [5], use permitted under the Creative Commons Attribution License CC BY.

This dissertation summarizes our efforts on addressing those printing problems and optimizing the FFF quality. We performed a combination of analytical, numerical, and novel experimental approaches on characterizing and understanding the factors that impact the FFF process. With that knowledge, practical guidelines for obtaining better printing quality were provided. In this dissertation, particular attention has been given to three common processing parameters (layer height, nozzle temperature, print speed) [9] and two environmental conditions (environmental temperature, environmental humidity).

1.2 Background

In the past few decades, a large number of studies have investigated the effects of different printing factors on geometrical and mechanical properties of FFF produced parts. In this section, those efforts have been reviewed and summarized.

1.2.1 Factors that impact printing quality

The most common variables include geometrical parameters (layer height, road width, gap between roads), thermal profiles (nozzle temperature, print bed temperature), and deposition rate (print speed, material feed rate), as illustrated in Figure 1.3 [11]–[15]. Besides these parameters that influence a single extrudate property, the tool path or strategy of how to stack up extrudates also contributes to the overall mechanical performance of the part. Thus, relevant parameters, including raster angle, infill density, and infill pattern, have been studied as well [16], [17].

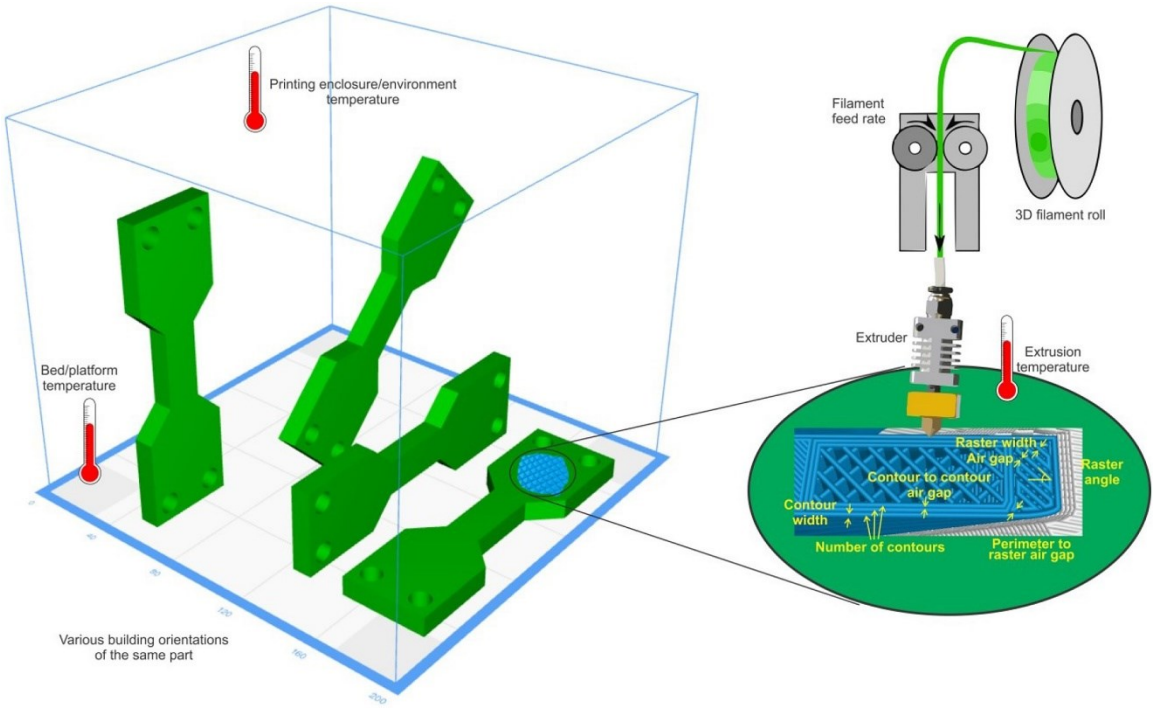

Figure 1.3: FFF process parameter – illustration, reproduced from [18], copyright 2018, with permission from Elsevier.

When varying geometrical parameters like layer height and road width, it will directly impact the single extrudate's geometry: lower values will result in higher tensile strength and finer geometrical accuracy [19]. However, this will also slow down the printing process and may cause higher time cost, so there is a tradeoff between the speed and quality [20]. In addition, considering the strategy of patterning and stacking each single extrudate, the raster angle plays an important role. Since the welding strength cannot exceed the material's intrinsic tensile strength, specimens will always have higher tensile strength along the aligned raster [21]. If the anisotropy is not desired, then 0°/90° or 45°/-45° depositing strategy could be applied [22]. In the meantime, the road gap and infill density can generate structural porosity, which will reduce the strength, but in return give faster

printing speed [23], [24]. Thus, in practical applications, typically the shell is printed with finer quality to have a smooth surface, while the interior has highly hollow infill patterns to save the material and time cost of the printing, as Figure 1.4 shows.

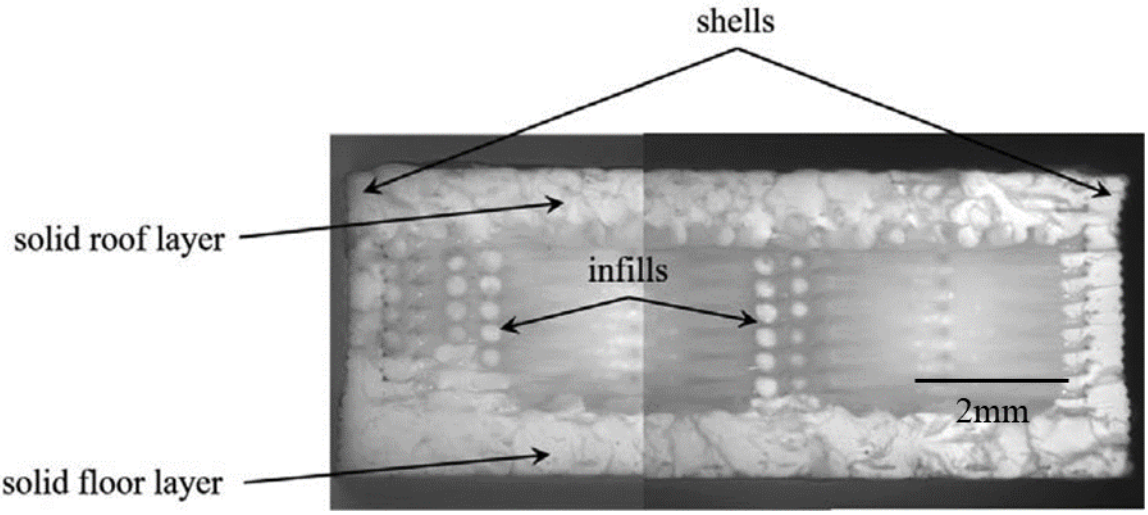

Figure 1.4: Cross-section of a printed specimen with a solid shell and 45°/-45° infill pattern, reproduced from [23], copyright 2002, © Emerald Publishing Limited all rights reserved.

Despite those geometrical factors, the thermal profile also plays an important role in printing quality. In principle, lower nozzle temperature and build plate temperature could make the extruded materials cool faster and give less time for welding, which has already been investigated by both numerical [25] and experimental studies [14]. Next, the shorter welding time (the duration that the interlayer region remains hotter than the glass transition temperature) could significantly reduce the welding quality between two adjacent layers as the polymer chains don't have enough time to form entanglements [26]–[29]. Experiments on printing ABS and PLA have shown that the mechanical properties (strength and tear energy) increase with higher nozzle temperatures, as Figure 1.5 shows [14], [30].

Additionally, there is an interesting slow-down in the increase when reaching certain temperature points, which is due to the full development of chain entanglements [31], [32].

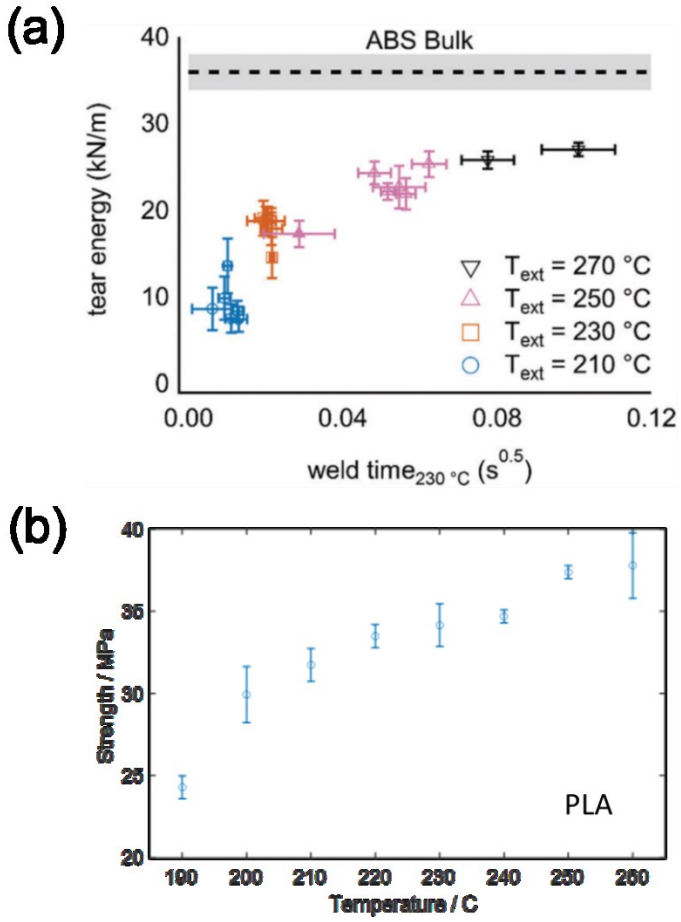

Figure 1.5: (a) Comparison of tear energy to equivalent isothermal weld time. At the top of the figure, the bulk tear energy from a pressed ABS sheet is shown. Horizontal error bars are calculated from the standard deviation of 3 replicates. Vertical error bars are calculated from the standard deviation of 5 to 10 replicates. Republished with permission of the Royal Society of Chemistry, from [14]; permission conveyed through Copyright Clearance Center, Inc. (b) The tensile strength of PLA specimens fabricated with different

nozzle temperatures, reproduced from [30], copyright 2019, use permitted under the Creative Commons Attribution License CC BY.

Finally, there are the environmental factors such as chamber temperature and humidity [33], which have long been insufficiently studied even though it was reported that they could significantly impact the printing quality: including introducing geometrical defects like warping and porosity, and reducing mechanical performance like strength (Figure 1.6) [34], [35].

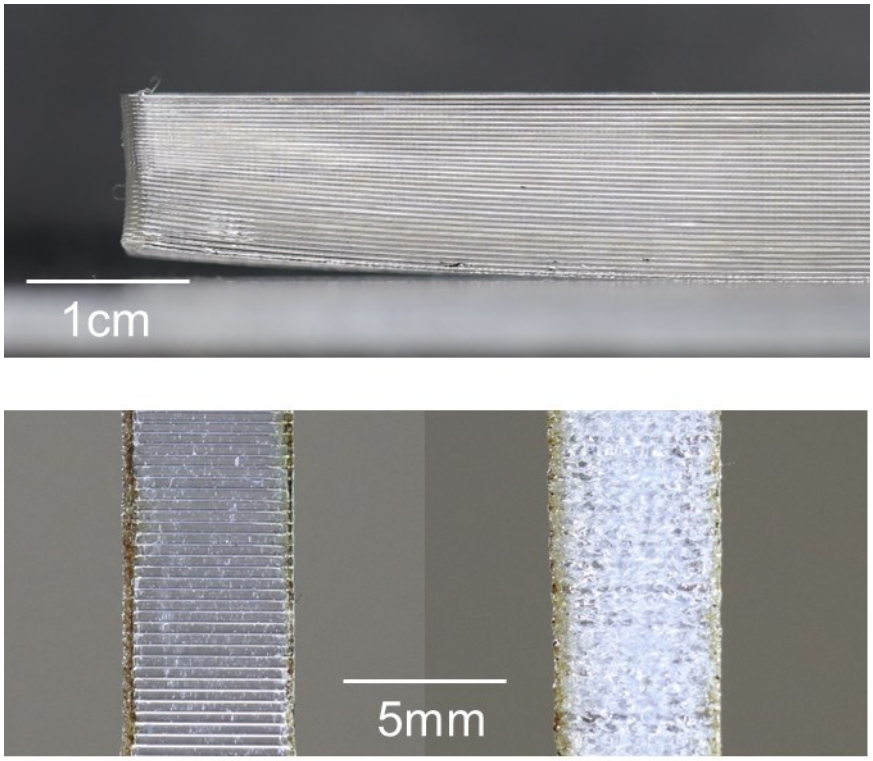

Figure 1.6: Typical defects induced by environmental conditions. Above is the warping defect caused by low environmental temperature; bottom is the comparison between

printing under dry (left) and humid (right) environment, which has a significant difference in surface finish.

To mitigate temperature-induced defects, a low cost and straightforward solution is adding a heated build plate to keep the specimen warm during printing. However, it was shown that a heated build plate could not provide a uniform temperature field across the entire building area (Figure 1.7), so that there still existed thermal-induced defects [9]. Then, the more expensive while effective solution is controlling the printing chamber's temperature, and there have been multiple numerical studies focusing on its effects. Xia *et al.* studied the interactions between the polymer and the ambient air, showing that hot air can slow down the cooling of the extruded polymer [36] and give more time for welding [37]. Costa *et al.* looked into more details of the heat exchange process, including the heat conduction between materials as well as the heat convection and radiation with the environment, showing the convection and conduction have the highest impact [38]. Wang *et al.* [39] and Liu *et al.* [40] simulated the specimen distortion during the FFF process and showed that keeping a high environmental temperature can reduce the warpages. However, since most open-source FFF printers do not have temperature-controlled chambers, there are much fewer experimental efforts reported. Sun *et al.* built a chamber for printing PEEK, which requires a high environmental temperature to print, and they did find a significant improvement in specimen strength [41]. Spoerk *et al.* printed polypropylene filled with glass spheres, which showed better annealing quality and dimensional accuracy with elevated chamber temperature [13], [42]. Carneiro *et al.* found a 20 °C increase in environmental temperature could reduce the structural porosity of printed ABS by 50 %

[43]. Armillotta *et al.* studied the specimen warpage with both analytical and experimental approaches and stated a high chamber temperature close to glass transition temperature could significantly reduce the warpage [44].

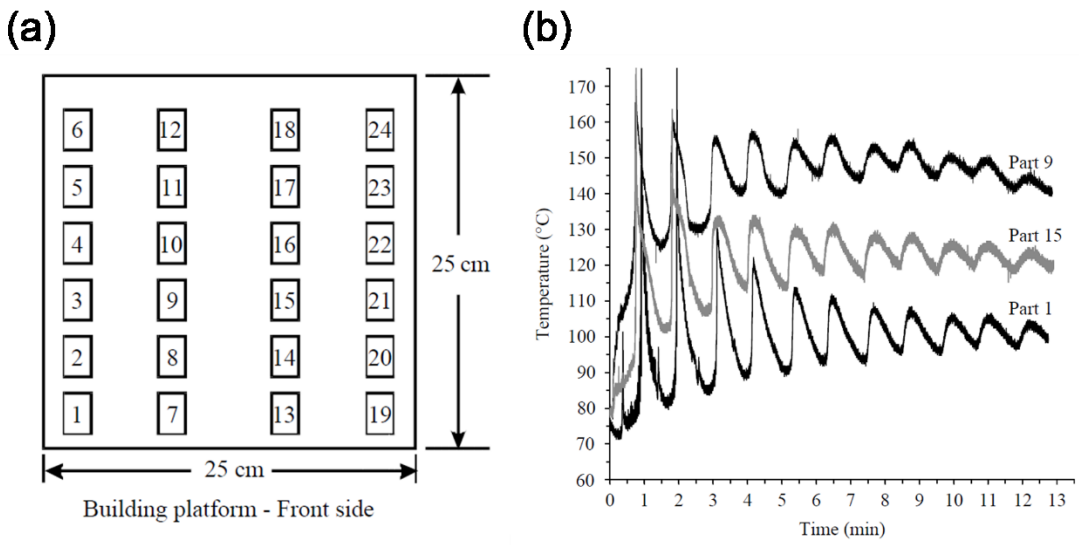

Figure 1.7: (a) Location of parts built on the platform (top view); (b) Variation in temperature profiles when varying the part building locations, Reproduced from [12], copyright 2008, © Emerald Publishing Limited all rights reserved.

Environmental humidity is another primary source of printing defects, while it is highly varied from material to material, considering their different water absorption properties [45]. For the polycarbonate (PC) that we are interested in, there have been some studies of its water absorption decades ago, investigating the physical property changes [46], and influences to the application of injection molding [47]. As Figure 1.8 shows, Ito *et al.* found PC could absorb up to 0.2 wt% of water within 3 hours under 24.5 °C and 88 % RH [48]. And multiple studies have shown that the PC's mechanical properties will drop

upon water absorption, for which the primary reason is the microstructural defects: the absorbed water clusters can lead to the formation of microcracks [47], [49], [50].

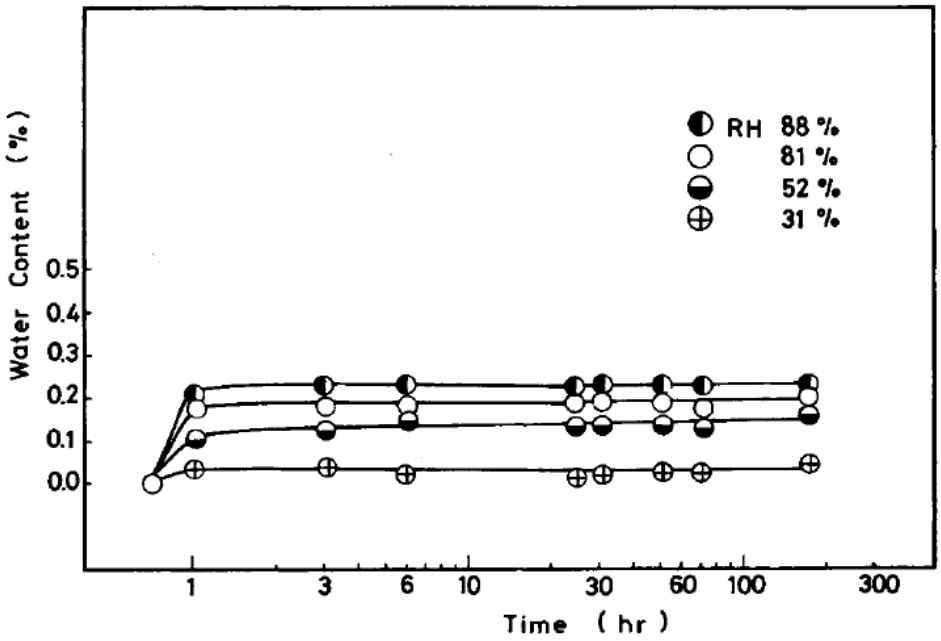

Figure 1.8: Changes in absorbed water content at various relative humidity values at 24.5 °C with time, reproduced from [48], copyright 2003, with permission from John Wiley and Sons.

However, the water absorption is closely related to the material geometry (cylindrical filaments in our case), and the FFF process is also different from injection molding considering the heating time, material quantity, and seal. Thus, a study specifically designed for FFF is required. There have been very few papers published in this area. Halidi *et al.* have studied the moisture sorption effects on ABS filaments and confirmed it would not cause nozzle clogging [51]. Kim *et al.* studied the water absorption of printed ABS specimens and their corresponding property changes. The humidity was introduced

together with a higher temperature, showing the printed parts have significant aging effects, and the strength is reduced when storing in hot and humid conditions [52]. Valerga *et al.* studied the effects of humidity on PLA printing, and they found the material could degrade during storage and create bubbles when printing (Figure 1.9), hence reducing the mechanical strength of printed parts [53].

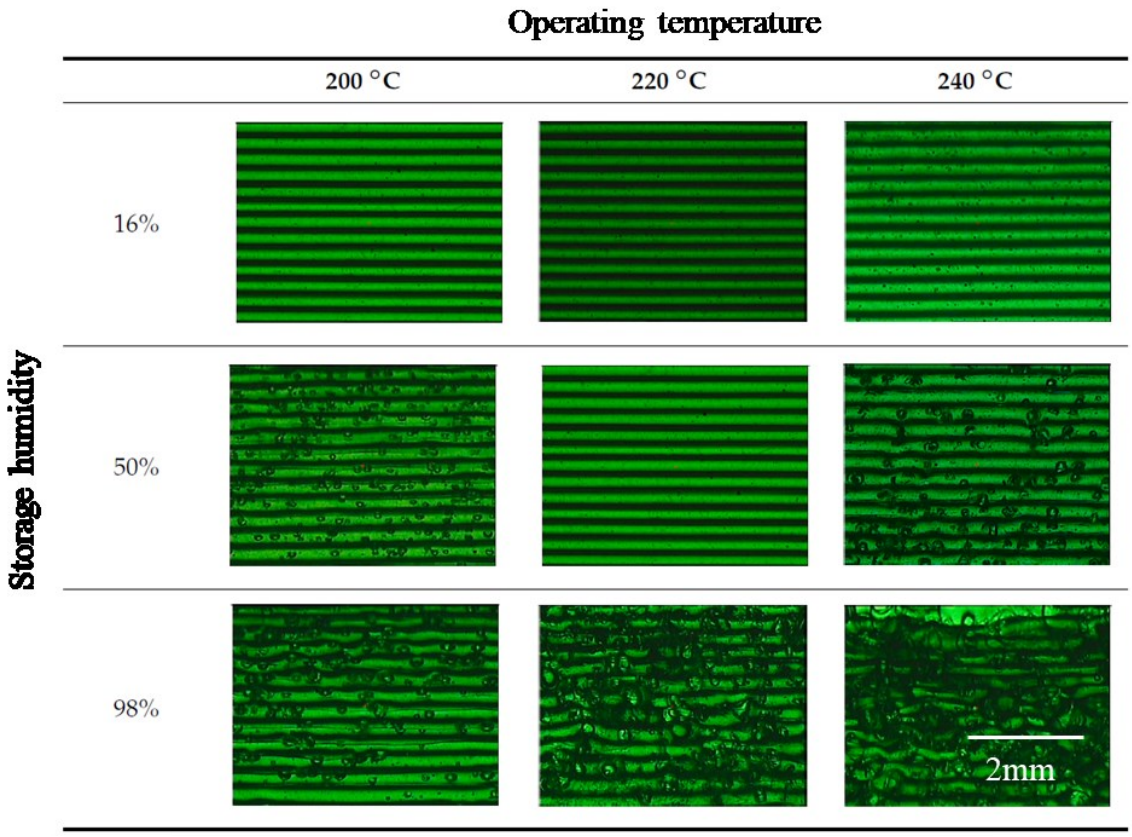

Figure 1.9: Influence of storage conditions and operating temperature on the surface finish of printed green PLA specimens, reproduced from [53], use permitted under the Creative Commons Attribution License CC BY.

1.2.2 Characterization of mechanical properties

In previous works, the most common experimental method for characterization of the printed part is the uniaxial tensile test. From the uniaxial tensile test and fractographic analysis, the failure modes of FFF products were studied, showing the strong anisotropy in both failure strength and fracture mechanisms [54]. Furthermore, by rotating the build orientation with respect to the loading direction, it is possible to measure the anisotropy of FFF specimens [55]. If using 0°/90° raster angles (Figure 1.10) to mitigate the anisotropy, then the strength will be compromised since the 0° raster (printed perpendicular to the tensile test direction) carries much weaker loads than the 90° raster (printed along the tensile test direction) [56].

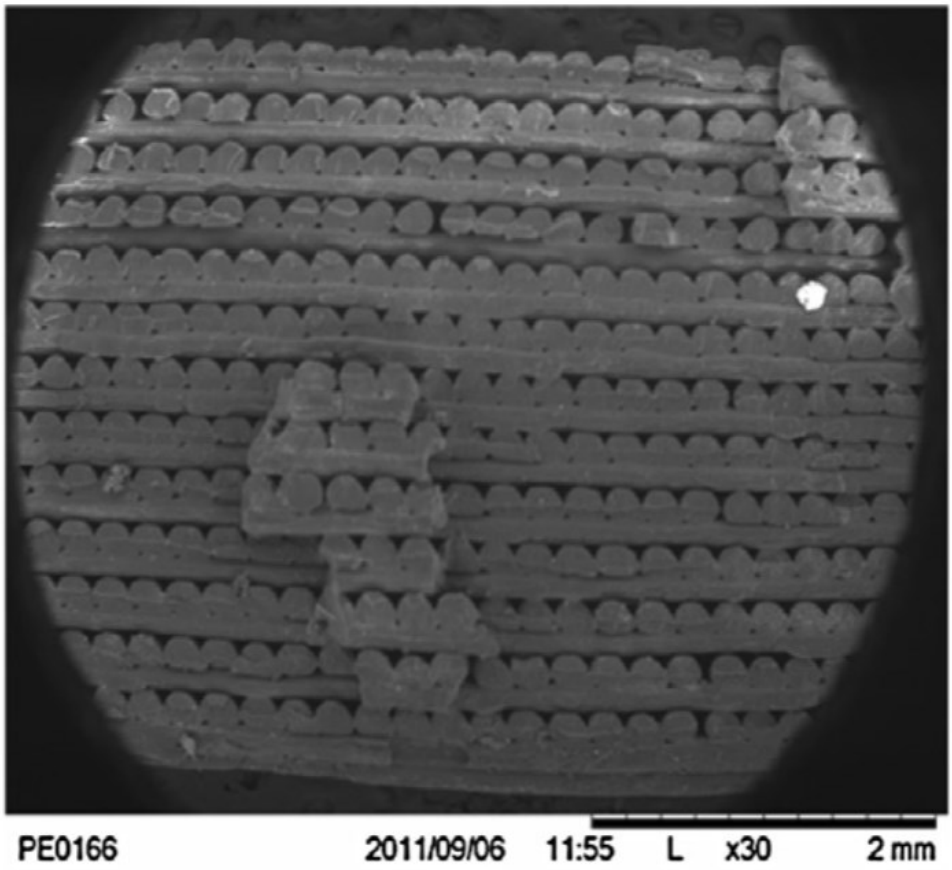

Figure 1.10: Fracture surface of a 0°/90° orientation specimen, reproduced from [56], copyright 2016, with permission from Elsevier.

To focus on the bonding quality between two adjacent extrudates, peeling tests [57] and Graves tear tests [58], [59] have also been reported, as shown in Figure 1.11. The tear tests suggested a strong relationship between nozzle temperature and tear strength, since high temperature can lead to longer welding time and better welding quality between the layer interfaces.

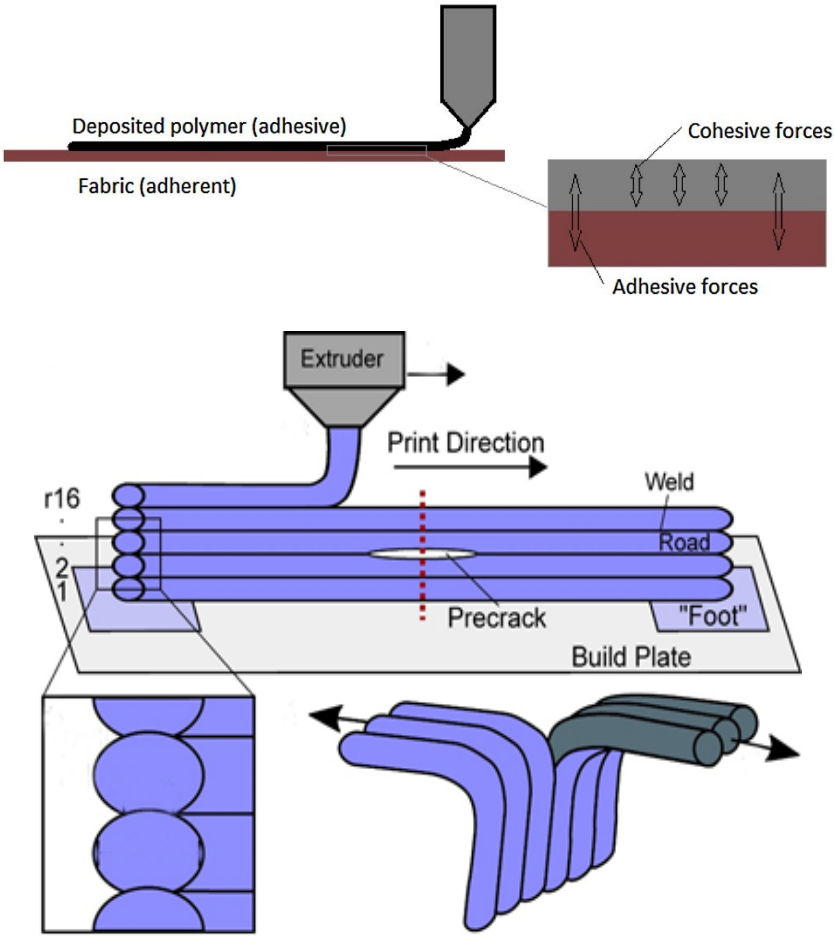

Figure 1.11: Schematic of sample preparation and experimental setup of peel test (top), reproduced from [57], use permitted under the Creative Commons Attribution License CC BY; and illustration of tear test (bottom), reproduced from [59], copyright 2017, with permission from Elsevier.

Nevertheless, only a few studies have quantitatively investigated the elastic response upon changing printing conditions, despite the common knowledge of additive manufactured parts have lower modulus. Studying Young's modulus, the important material property used for material design and selection, of 3D-printed parts is especially important when considering the elastic response of a printed thin wall, which has a highly non-uniform cross-section geometry and very different mechanical performance [60]. Among the few studies that have addressed the elastic behavior of printed parts, most of them concluded that the tool path [61]–[64] and infill density [65], [66] are the critical factors that impact the modulus, as they could influence the effective loading area. Additionally, Park *et al.* [67] also indicated the geometrical non-uniformity brought by printer mechanical inaccuracy could further decrease the modulus as well (Figure 1.12).

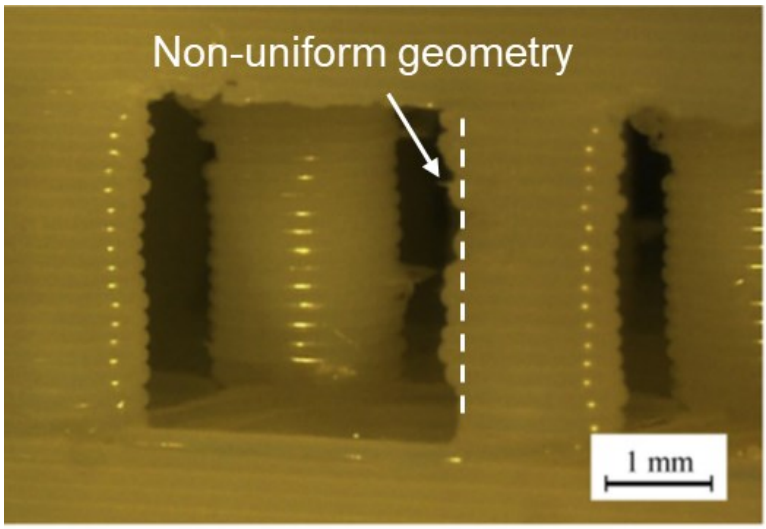

Figure 1.12: The geometry non-uniformity in FFF specimen, reproduced from [67], copyright 2014, with permission from Elsevier.

1.2.3 Characterization of geometry

Besides mechanical properties, another important quality issue is the dimensional accuracy and stability. To characterize the dimension of FFF products, there have been various studies applying different techniques, including optical microscopy [68], flatbed scanning [69], scanning electron microscopy (SEM, Figure 1.13) [9] and profilometer [70]. However, these methods are limited to 2D geometries like dimensional accuracy and surface roughness, and it is impossible to obtain interior information without sectioning, which will destroy the specimen [71]. To non-destructively obtain the 3D structure of the printed sample, X-ray micro-computed tomography (micro-CT) is a suitable tool.

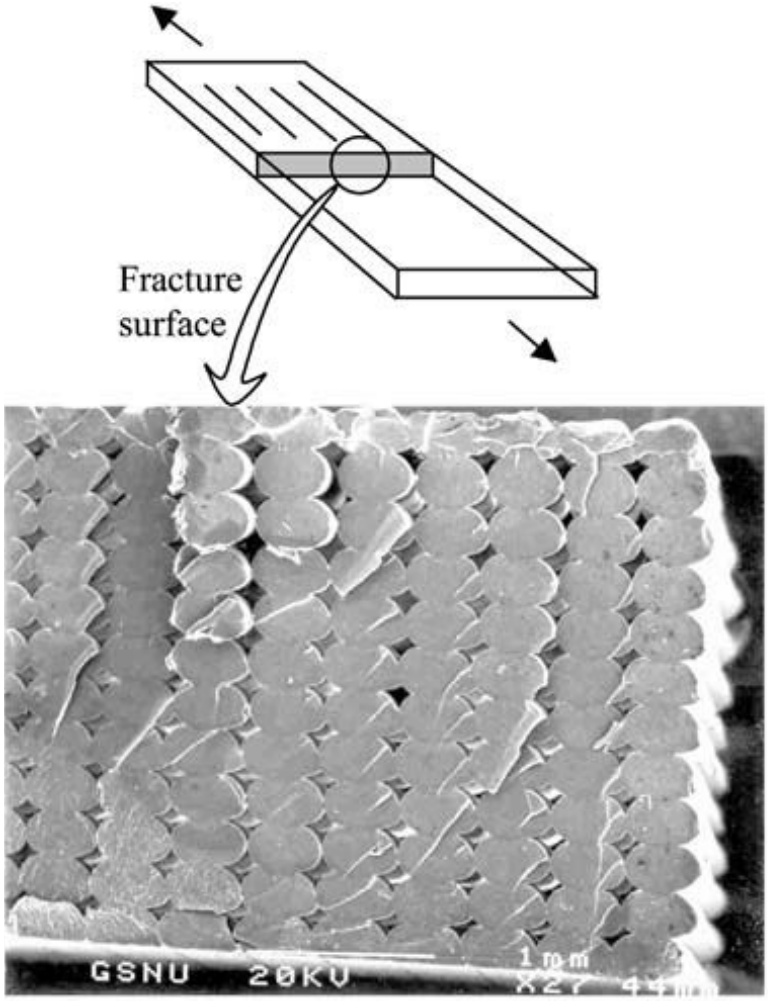

Figure 1.13: Fracture surface under SEM, reproduced from [9], copyright 2002, © Emerald Publishing Limited all rights reserved.

As shown in Figure 1.14, micro-CT can generate 3D digital models of a specimen by taking multiple X-ray images from different angles and reconstructing its 3D profile from the cross-sectional images, with up to micron-level resolution [72]. Micro-CT was identified as a method to assess the quality of the 3D printed part in the early 90s [73] with the first application of this concept to the AM process in 1997 [74]. Subsequently, micro-CT has been utilized in powder-based AM, which has inevitable pore defects, to study its

influence on geometry and hence the mechanical properties [75]–[77]. More recently, micro-CT technologies have been utilized for various studies of FFF prints [78], including studying the structural voids caused by road gaps and infill patterns [79], [80]; characterizing air bubbles trapped inside printed specimens [81]; assessing the dimensional accuracy (deviation between scanned geometry and digital design) and inner defects of AM products applied in engineering [82], [83]; investigating anisotropic effects driven by pore percolation of samples with different raster directions [79], [84]; characterizing microstructural features of multi-directional preform [85] and fiber-reinforced composites [83], [86]; and understanding failure mechanism combined with in-situ tensile tests [66]. Recently, there is a study focusing on the effects of fabrication temperature, studying the relationship between mechanical strength and internal geometry [30].

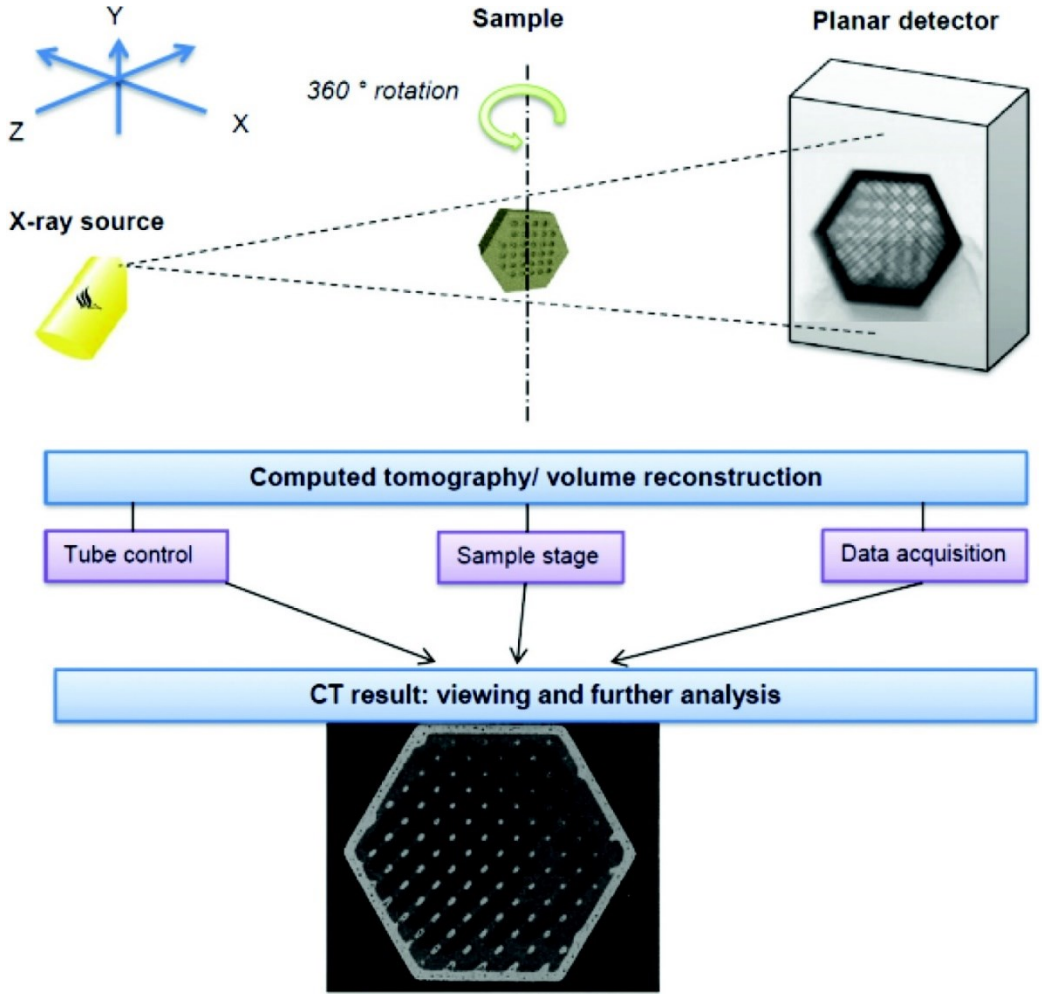

Figure 1.14: Schematic of an X-ray micro-CT scan, reproduced from [78], copyright 2018, with permission from Mary Ann Liebert, Inc.

1.3 Thesis Overview

This thesis is a part of a collaborative project to uncover the relationships between key processing parameters and the anisotropy, strength, and toughness of FFF printed materials. The team consists of scientists and engineers from Johns Hopkins University, Georgetown University, and the National Institute of Standards and Technology, and the project is funded by the National Science Foundation.

The overall objective of this study is using a combination of analytical derivation, finite element analysis, and experimental tools to reveal the relationship between processing parameters, as-printed structures, and specimen properties. The subsequent structural and material property changes due to varied processing parameters could be explained with analytical models and further experimental validations. Then, the structure - mechanical property relationship could be simulated by finite element analysis. By linking those relationships, the guideline of optimizing parameters and improving printing quality could be proposed, more practical recommendations could be provided to printer users, and the data could work as references and help future studies.

The thesis is organized in the following manner. Chapter 1 introduces the motivation of performing this study and outlines the background of this field, discusses the current research progress and the limitations. Chapter 2 describes the general fabrication and characterization techniques used in this study, including material characterization, FFF printer system setup, micro-CT scan, and mechanical tensile tests. Chapter 3 details the geometrical and mechanical impacts of varying common FFF processing parameters, including layer height, nozzle temperature, and print speed, explaining the mechanisms behind property changes. Chapter 4 discusses the influence of changing environmental conditions (temperature and humidity) and proposes models to help to understand the relationship between temperature - thermal gradient - warping, as well as the relationship for humidity - porosity - mechanical properties. Chapter 5 focuses on characterizing the effective Young's modulus of printed specimens, utilizing both numerical and empirical methods to provide insights on the mechanical behaviors as well as gives practical

suggestions for engineering applications. Chapter 6 concludes the key findings of this dissertation and discusses future research directions.

Chapter 2 : Sample Preparation and Characterization

This chapter describes the general fabrication and characterization methods we are using, introducing printing material, printer setup, micro-CT scans, and mechanical tensile tests. Other than those specified, all specimens are fabricated and characterized by the following procedures.

2.1 Fabrication

2.1.1 Materials

In this study, 2.85 mm bisphenol-A-polycarbonate (PC) filament from Ultimaker was used to fabricate all the specimens. PC is one of the most popular FFF printing materials due to its high strength and high thermal resistance, compared to other common printing polymers like PLA and ABS, according to Ultimaker's specification; and it's also printable at lower temperatures (compared to PEEK) and only requires lower-cost hardware. Here we have two additional considerations of choosing PC as the target material system: firstly, it is an amorphous linear homopolymer, so no crystallinity / material blend / polymer branching needs to be considered; secondly, the PC filament is transparent so that it is easier to visually observe and check internal printing defects.

First of all, the glass transition temperature of the PC filaments was measured. 10 mg of PC was cut and heated from 50 °C to 250 °C with a 5 °C/min heating rate in the TA Instruments DSC Q20 Differential Scanning Calorimeter. As shown in Figure 2.1, the

peak of specific heat was observed at 114 °C, which indicates our PC's glass transition temperature. This also matches well with the data from the manufacturer.

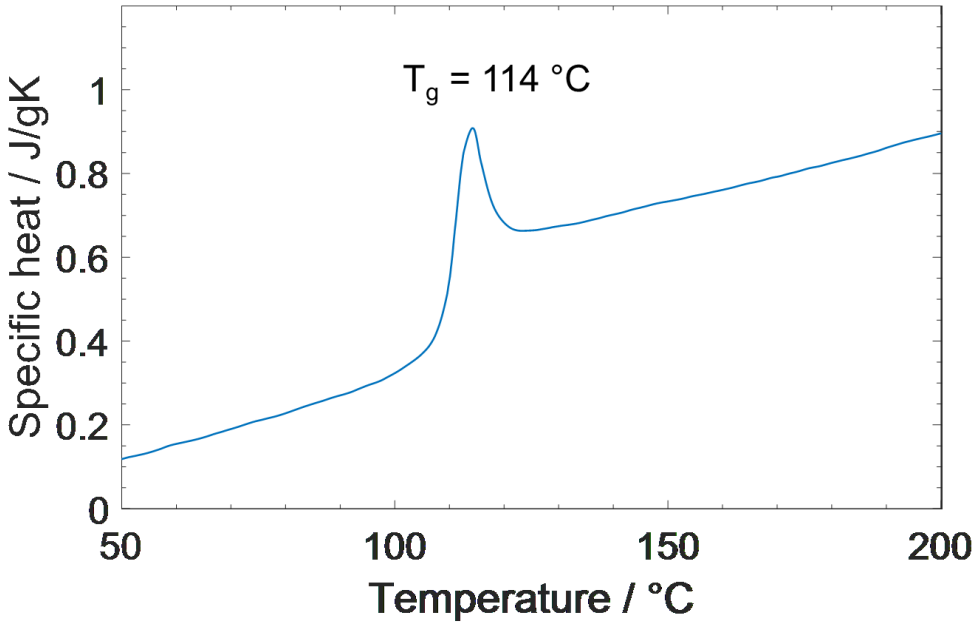

Figure 2.1: Glass transition temperature revealed from the DSC scan.

Then with assistance from Mr. Ojaswi Agarwal, tensile strength and Young's modulus of PC filaments were measured with uniaxial tensile tests (Figure 2.2).

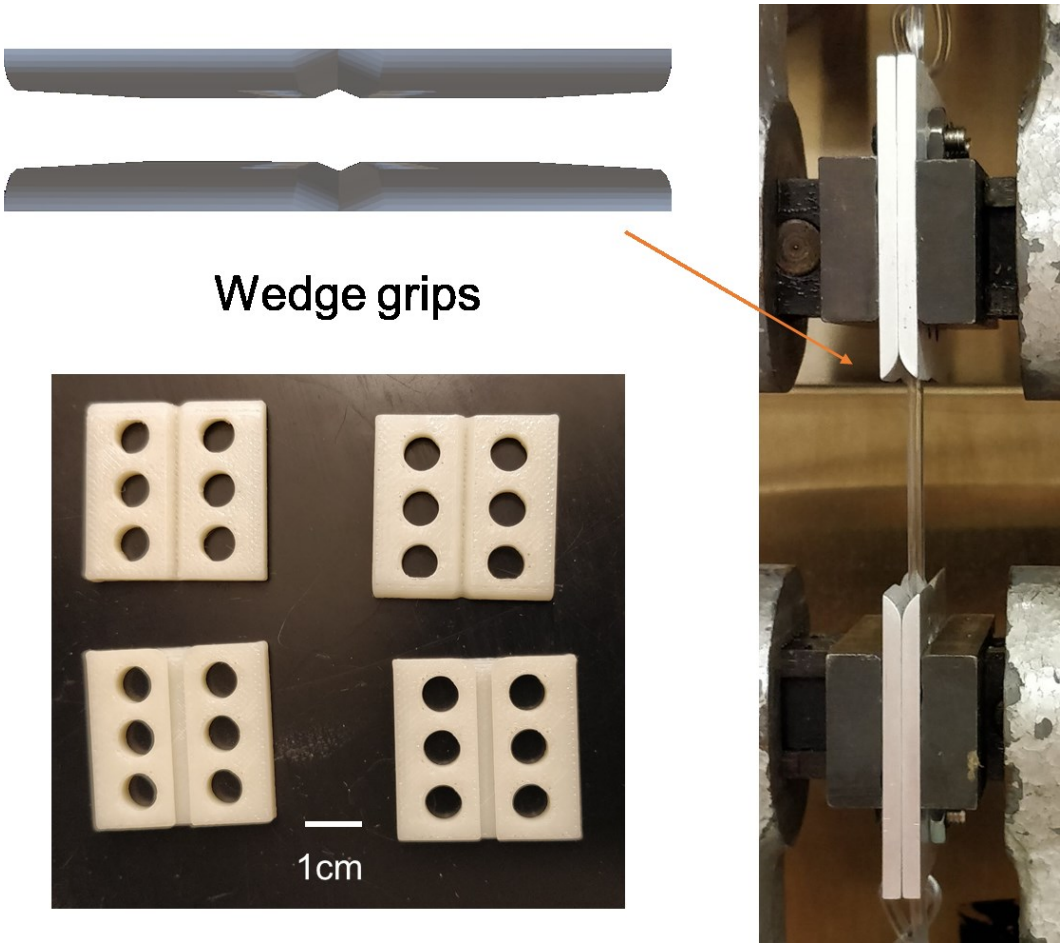

Figure 2.2: Setup of filament tensile tests, courtesy: Ojaswi Agarwal.

The Ultimaker filament was annealed at 140 °C (above the glass transition temperature) for 1 h, then clamped with serrated wedge grips (the Advantage Wedge 10 with serrated wedges) for round specimens and pulled at a quasi-static strain rate of 10^{-3} s^{-1}. The Young's modulus and the peak stress are shown in Figure 2.3 (a plot of engineering stress vs. engineering strain). The values are taken from the average of 5 samples each, and the range reported is one standard deviation (tabulated in Table 2.1). The printed filament was printed from the stress relieved Ultimaker filament (i.e., without curvature) from a 0.5 mm wide nozzle in a LulzBot TAZ Single Tool Head v2.1. The

nozzle was heated to 280 °C and suspended 30 cm above the print bed. The filament was extruded at a rate of 3 mm^3/s into a chamber held at 22 °C in ambient condition. This filament was cut into straight 30 mm length sections and held with Bionix Vise grips and EnviroBath Optional Grip 0.9. They were pulled with a quasi-static strain rate of 10^{-3} s^{-1}. Both tests were run on an MTS Criterion Series 40 at ambient laboratory conditions right after the specimen preparation.

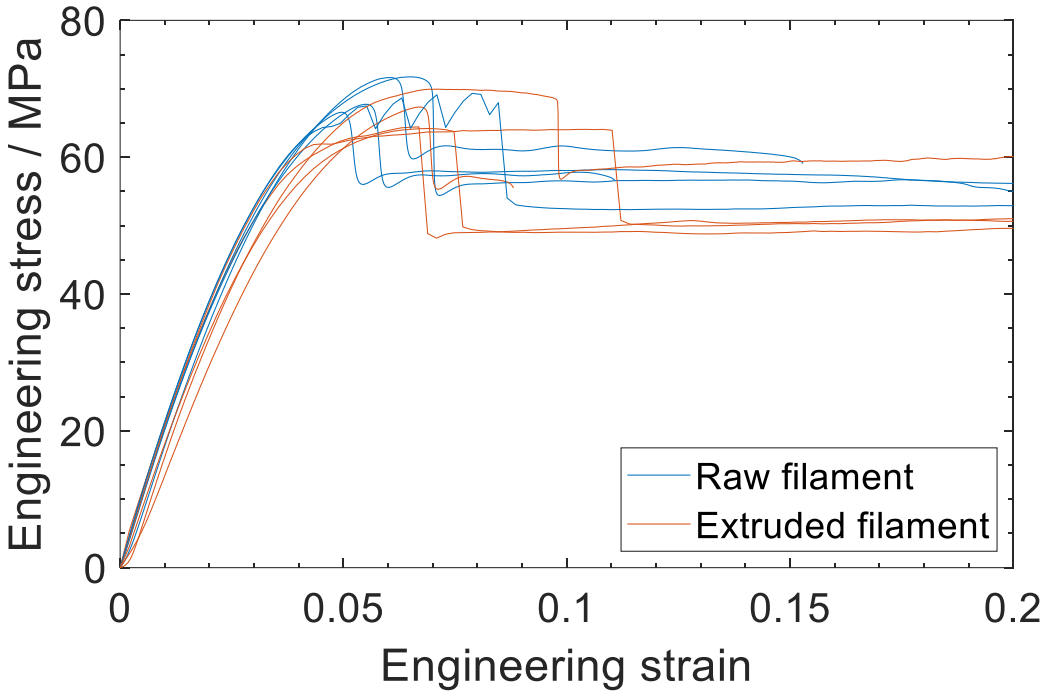

Figure 2.3: Uniaxial tension plot of Ultimaker filaments before and after printing, five repeating tests for each case.

Table 2.1: Tabulated values of uniaxial tension specimens.

	Diameter (mm)	**Young's Modulus (GPa)**	**Peak Stress (MPa)**
Bulk Filament	2.85 ± 0.02	1.87 ± 0.13	71.6 ± 3.6
Printed Filament	0.46 ± 0.03	1.82 ± 0.05	66.4 ± 3.0

2.1.2 FFF process procedures and conditions

An open-source Lulzbot TAZ6 3D printer with 280 mm × 280 mm × 250 mm printing volume was used for sample fabrication. The print head we used is a LulzBot hexagon hot end tool head with 0.5 mm nozzle diameter. This printer extruder, equipped with an all-metal hot end, could heat up to 300 °C, and the build plate could heat up to 120 °C. For better heat uniformity across the build plate surface, we replaced the original one with Lulzbot TAZ modular print bed heater. To have a low humidity environment for printing, a commercially available 3 mm-thickness acrylic enclosure (Printed Solid safety enclosure kit for Lulzbot TAZ 6) was added to the printer. To easily load and fetch the materials, we customized the front panel of the enclosure by making a 341 mm × 241 mm door through laser cutting (Figure 2.4).

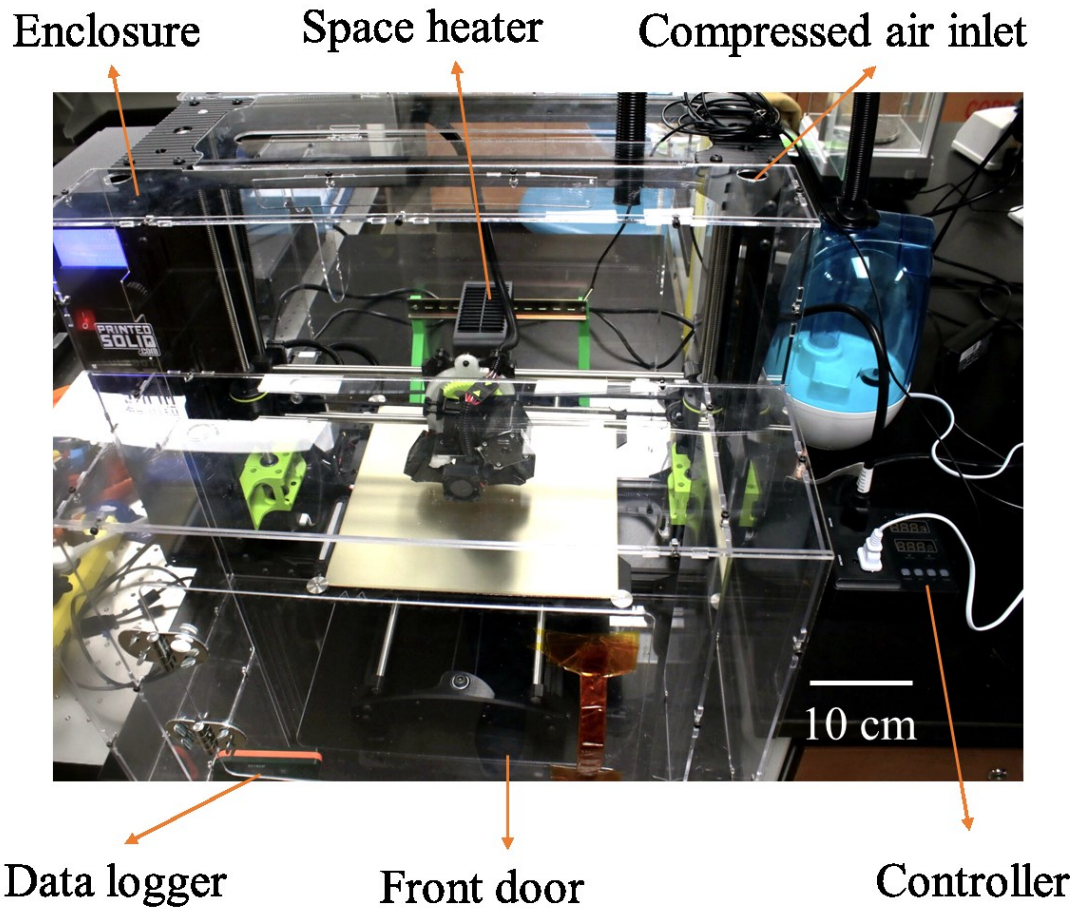

Figure 2.4: Picture of the printer set-up used in this study.

To reduce printing defects, the polycarbonate filaments were dried in an oven (Lindberg/Blue M Vacuum Oven VO914C) at 100 °C for one hour before each printing process. During printing, the in-house compressed air line was connected to the enclosure to continuously provide dry air into the system. Our experiments showed that the relative humidity (RH) inside the enclosure could be reduced to 10 % RH within 10 min after turning on the compressed air. To monitor real-time environmental temperature and humidity during the printing process, a USB multifunction datalogger (EXTECH Model RHT35) was added to this system. The data logs showed that all sample fabrication

processes were conducted at room temperature (22 °C) and low humidity environment (≤ 10 % RH).

2.1.3 Specimen geometry

As Figure 2.5 shows, a hollow box geometry (70 mm by 70 mm by 50 mm) was used to prepare tensile and micro-CT specimens in this study. Each side of the box represents a single extrudate wide wall, formed by multiple extrudates stacking up one over another: within each layer, there is only one continuous extrudate deposited as a hollow square. The width of the wall equals the width of a single extrudate, which is set to be the same with the nozzle diameter of 0.5 mm.

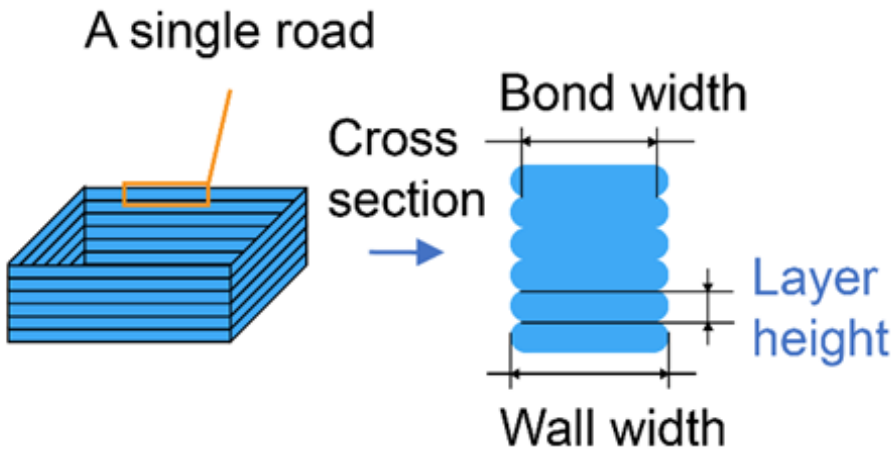

Figure 2.5: Schematics of printed geometry of one-layer wide hollow box.

2.2 Characterization

2.2.1 Geometrical characterizations

As Figure 2.6 shows, a 10 mm by 10 mm piece of single filament wall was cut and scanned by Bruker Skyscan 1172 Micro-CT scanner. With a resolution of 4.87 μm/pixel, the relevant geometric information, including wall width and bond width, could be measured and extracted by image analysis with MATLAB. The scanned geometry was further compared with the original design and other specimens with different processing conditions to gain a better understanding of how processing parameters influence printing geometry. Additionally, to verify the accuracy of micro-CT measurement results, dimensions were compared against optical microscope measurements.

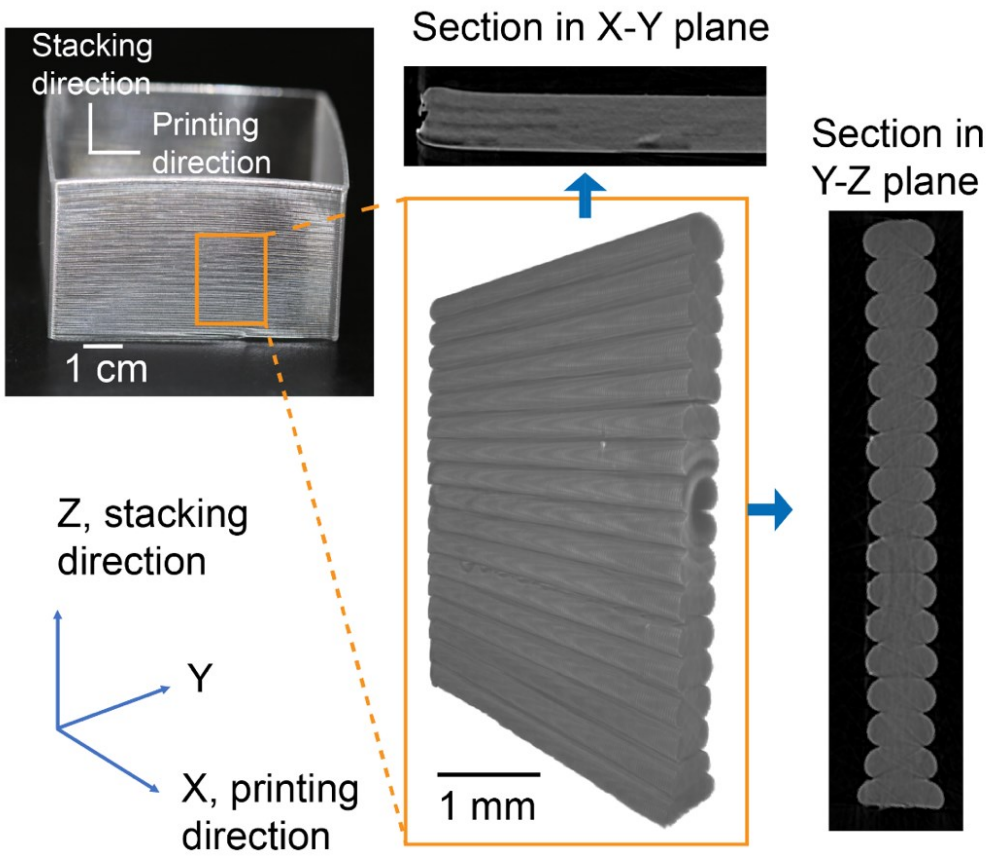

Figure 2.6: Reconstructed 3D geometry from micro-CT scans and its projections to two planes.

To validate the micro-CT measurements based on post-processing, the cross-sections of the printed parts were characterized by an optical microscope. After micro-CT scans, a key parameter for post-processing is the threshold, which defines the signal level used in post-processing: if a region has higher-than-threshold readings, it is considered to be solid material; otherwise it is considered to be air. As Figure 2.7(a) shows, different threshold selections can lead to significant differences in reconstructed geometry. To validate our results, we used an IsoMet 1000 diamond blade sectioning saw to section our printed samples. The flat cross-section planes were then observed and captured with a

Leica DM2700M optical microscope. The exact width was measured by counting pixels, which has a resolution of 1.07 μm per pixel, much better than 4.87 μm per pixel resolution of the micro-CT. The comparison between the two results are plotted in Figure 2.7(b). Both results converged together within a range of threshold from 0.13 to 0.16. This indicates that we could get satisfactory micro-CT measurements using any of the thresholds within the optimal range. While there are still little discrepancies (up to the size of one pixel) between different layers and thresholds, we chose 0.15 as the threshold in this study to get the highest accuracy across all conditions.

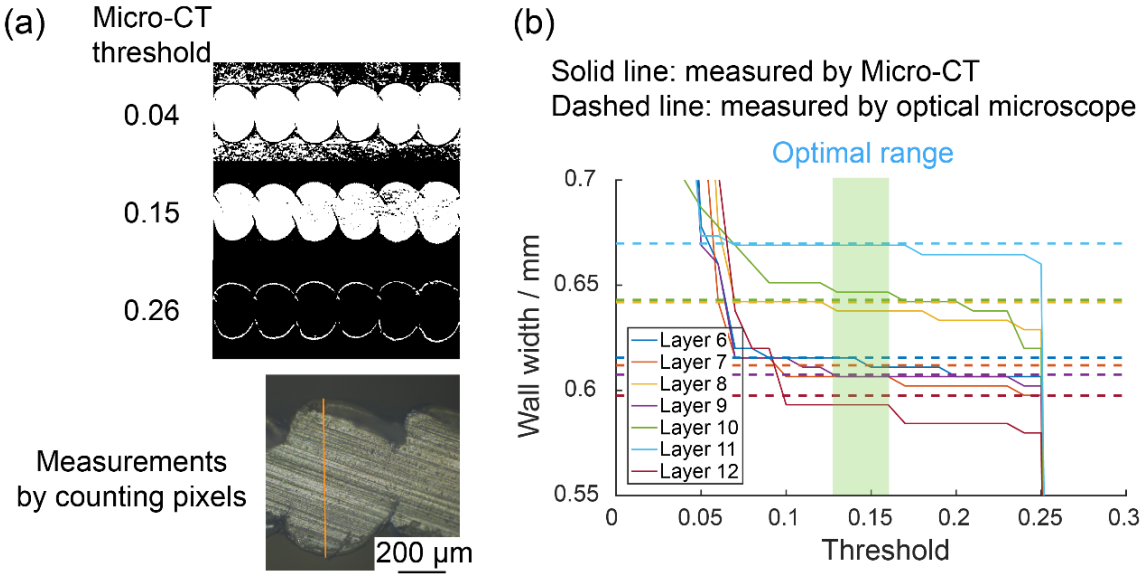

Figure 2.7: Validation of micro-CT results. (a) The reconstructed geometry from micro-CT varies with the post-processing threshold. To validate the results, the exact filament width was measured using an optical microscope. (b) The CT results converge with the microscope-measured results within an optimal range of thresholds.

2.2.2 Mechanical tensile tests

Uniaxial tensile tests were performed with an Instron ElectroPlus E1000 tester based on the ASTM D1708 standard. As Figure 2.8 shows, dogbone tensile specimens with 12 mm by 5 mm gauge area were fabricated with a VLS 6.60 laser cutter. Since heat from laser cutting can bring significant thermochemical effects like surface browning, painter's tape was attached on both sides of the single filament wall to shield the specimens and mitigate those effects.

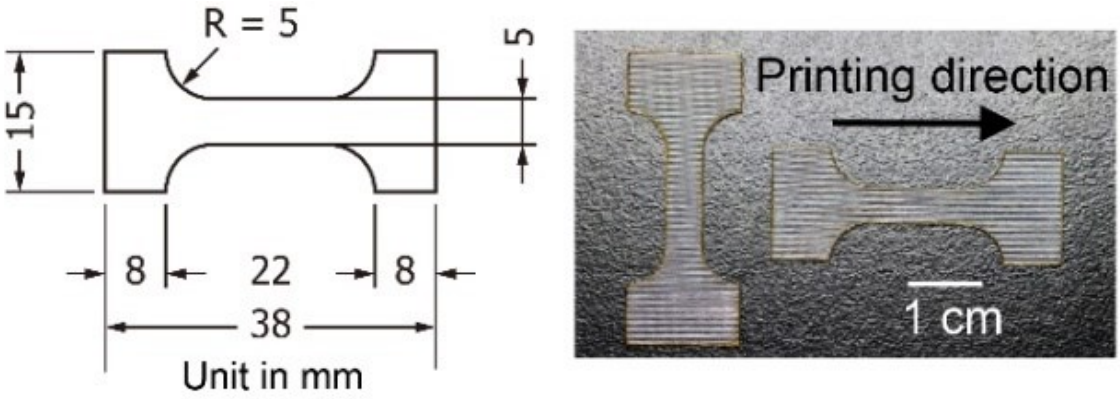

Figure 2.8: Geometry of tensile specimens.

Through observation (Figure 2.9), the browning was significantly reduced (while not entirely eliminated). For the cut edges, the polymer was molten and smoothed by laser cutting, which would minimize stress concentrations. For each set of processing parameters, at least 10 tensile specimens were fabricated and tested, with 5 specimens tested along printing direction (longitudinal test) and 5 specimens tested perpendicular to printing direction (transverse test).

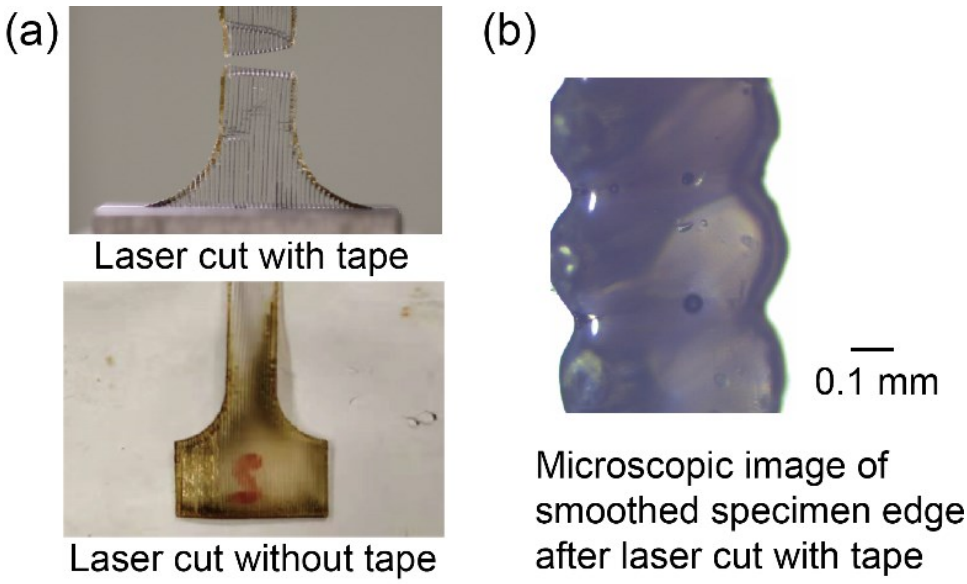

Figure 2.9: (a) Comparison between different laser cut processes. (b) The microscopic side view of the cut showing the materials are molten and smoothed by laser cut with protective paper tape.

According to the ASTM D1708 standard, the speed of testing is set to be 0.01 mm/s for quasi-static conditions (less than 0.001/s strain rate), and the yield point was reached around 100 s. During the tests, the strain within the gauge area (where the tensile specimen has a constant width of 5 mm) was captured by Digital Image Correlation (DIC). To be noted here, as the surfaces of tensile specimens are not flat, DIC of speckle patterns did not work well in this study. Through some preliminary trials, the DIC of speckles generally had bad correlations, and it would give stochastic surface strain readings, which could not represent the real strain of test specimens. Thus, for here we made two marks within the gauge area and tracked their movements via recorded video.

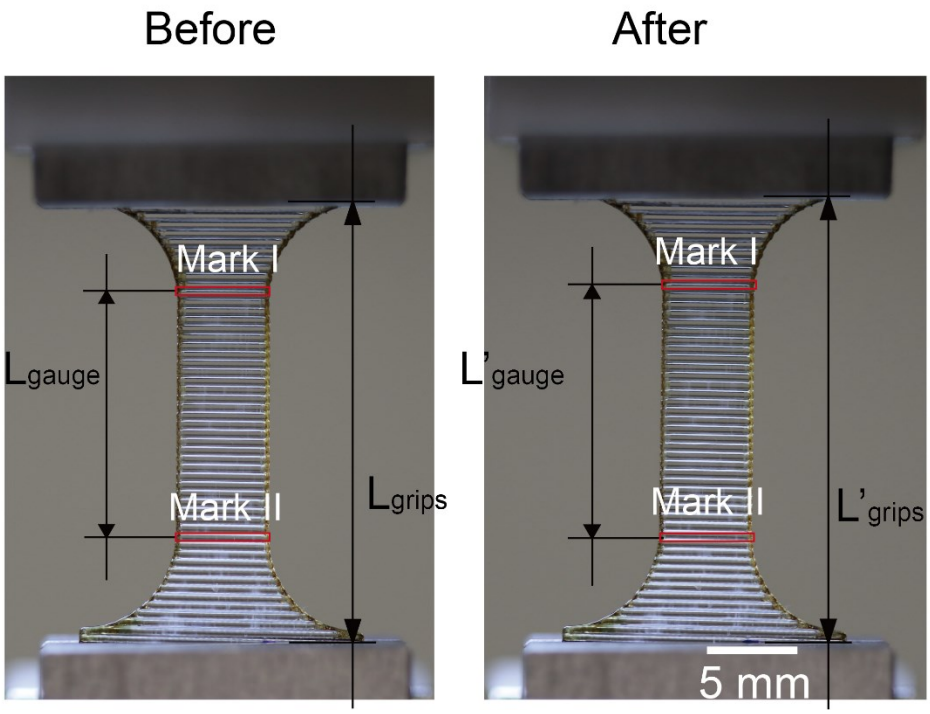

Figure 2.10: Measurement of gauge area strain.

30 frames-per-second videos were taken on a Canon EOS 80D digital single-lens reflex (DSLR) camera, and the 1920*1080-pixel videos could provide a resolution of 18.5 μm/pixel. Figure 2.10 shows the measurements we have done during this process. Firstly, before tests, the distance between two marks and the distance between two grips were measured. Then, the image was captured at the time of interest, and the distances between two gauge area marks and two grips were measured again. From those numbers, engineering strain values in the gauge area were calculated as Equations 2.1:

$$\varepsilon_{gauge} = (L'_{gauge} - L_{gauge})/L_{gauge} \tag{2.1}$$

Further from video analysis, the relationship between time and gauge area strain ε_{gauge} could be calculated, and correlated with the force-time curve recorded by the tensile machine.

After the tests, Young's modulus and mechanical strength were calculated based on force-displacement curves and specimen geometry. To be noted here, two different calculation approaches were used regarding different application scenarios. For engineering applications that do not account for the specimen's internal geometries, the tensile specimen is considered as a flat plate. Here the nominal tensile strength is calculated as the fracture force divided by the measured average initial cross-sectional area. Similarly, for the nominal Young's modulus, the stress was calculated as force divided by measured average initial cross-section area, while the strain was analyzed from the pictures taken during tests (Equation 2.1 and Figure 2.10). On the other hand, if we want to characterize the bonding quality, we need to look into the detailed structures.

Chapter 3 : Effects of Printing Parameters

In this chapter, we focused on the interlayer bonding region of bisphenol-A-polycarbonate samples and studied the effects on changing printing parameters on their properties. The results showed significant geometry variations depending on different printing conditions, including print speed, layer height, and nozzle temperature. Based on the results, we demonstrated the effects of reducing layer height, increasing nozzle temperature as well as compensating material extrusion rate to improve geometric precision with a minimum of 0.8 % deviation.

3.1 Introduction

As stated in Chapter 1.2, there have been many works studying the geometrical and mechanical effects of changing processing parameters. However, most studies experimentally investigated the mechanical properties of bulk cubic structures or multi-layer dogbone tensile specimens, rather than focusing on welding zones between adjacent layers, which are crucial for gaining a fundamental understanding of the relationship between process and property. Meanwhile, there is no quantitative study systematically covering all the major processing parameters in FFF, investigating the 3D geometry of the interlayer bonding region, and analyzing its correlation with mechanical performance.

In this study, we selected some of the most important processing parameters: print speed, layer height, and nozzle temperature, and investigated how these parameters affect

the geometrical and mechanical quality of FFF products. We extracted the geometrical data of FFF samples fabricated with different processing parameters by using micro-CT and further analyzed the data. Then, we combined the geometrical analysis with the uniaxial tensile test results to study the effects of processing parameters on the bonding quality and the resulting geometrical and mechanical quality. Finally, we optimized the processing parameters based on the results from the study to produce FFF samples with better geometrical precision and mechanical performance.

3.2 Materials and Methods

3.2.1 Processing parameters

Three different processing parameters were separately varied during printing: layer height (0.05 mm to 0.45 mm), nozzle temperature (230 °C to 290 °C), and print speed (5 mm/s to 30 mm/s). As a result, the volumetric flow rate will vary upon the changes of layer height and print speed. While all other parameters, including 0.5 mm road width, 115 °C build plate temperature, and 100% flow index (also known as extrusion multiplier), were set to be constant during this study.

3.3 Geometrical and Mechanical Effects of Varying Processing Parameters

Throughout the tensile tests, longitudinal tests (along printing direction) and transverse tests (perpendicular to printing directions) showed different failure modes. As shown in Figure 3.1, longitudinal samples had ductile failure. The specimen firstly yielded, formed a necking zone, then the crack initiated at one side and propagated until the entire

sample reached a complete failure. Conversely, the transverse samples fractured much faster. From the videos, there was no sign before the specimen reached a sudden catastrophic failure, while more details could potentially be revealed from high-speed imaging. As observed after the tests, the cracks in transverse samples formed along the bonding interface, which is an expected result since the bonding zone has minimal area and strength. Since the transverse tensile specimen will fracture along the weakest bonding region, the measured bond width was used to calculate mechanical strength at the bonding region, which equals to fracture force divided by measured bonding area of 5 mm by bond width (< 0.5 mm, depending on printing parameters).

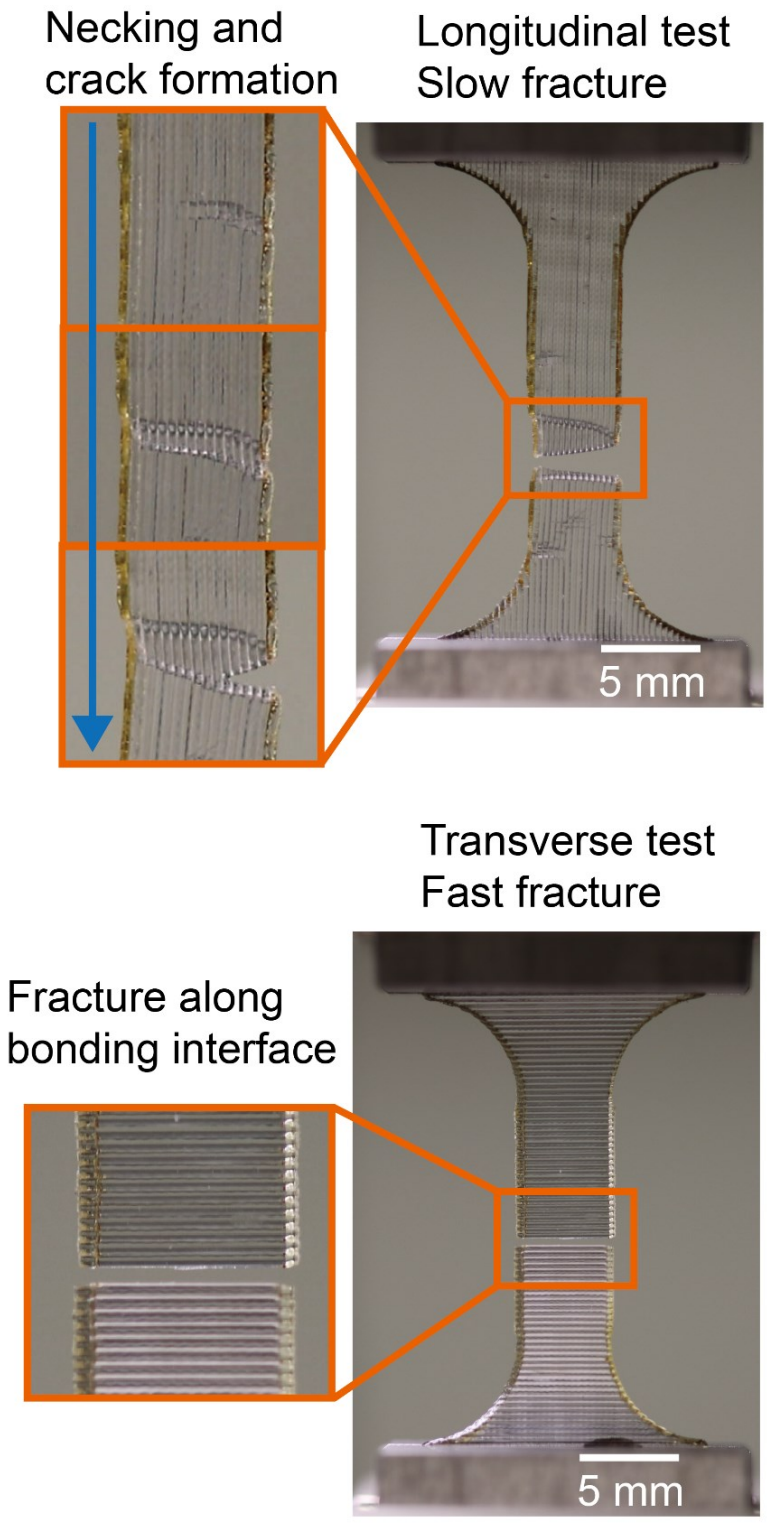

Figure 3.1: Sample fracture modes.

To get a better understanding of the microscopic fracture mechanism, SEM scans were performed on the fracture surfaces using Tescan Mira-3. With assistance from Mr. Bohan Sun, Mr. Hao Sheng, and Dr. Luoning Ma, 5 nm of Pd-Au were deposited on the specimens via sputter coating, and multiple SEM images were taken. For the longitudinal direction tests, we could see the river patterns across the entire fracture surface, showing the crack propagation direction, as Figure 3.2 shows.

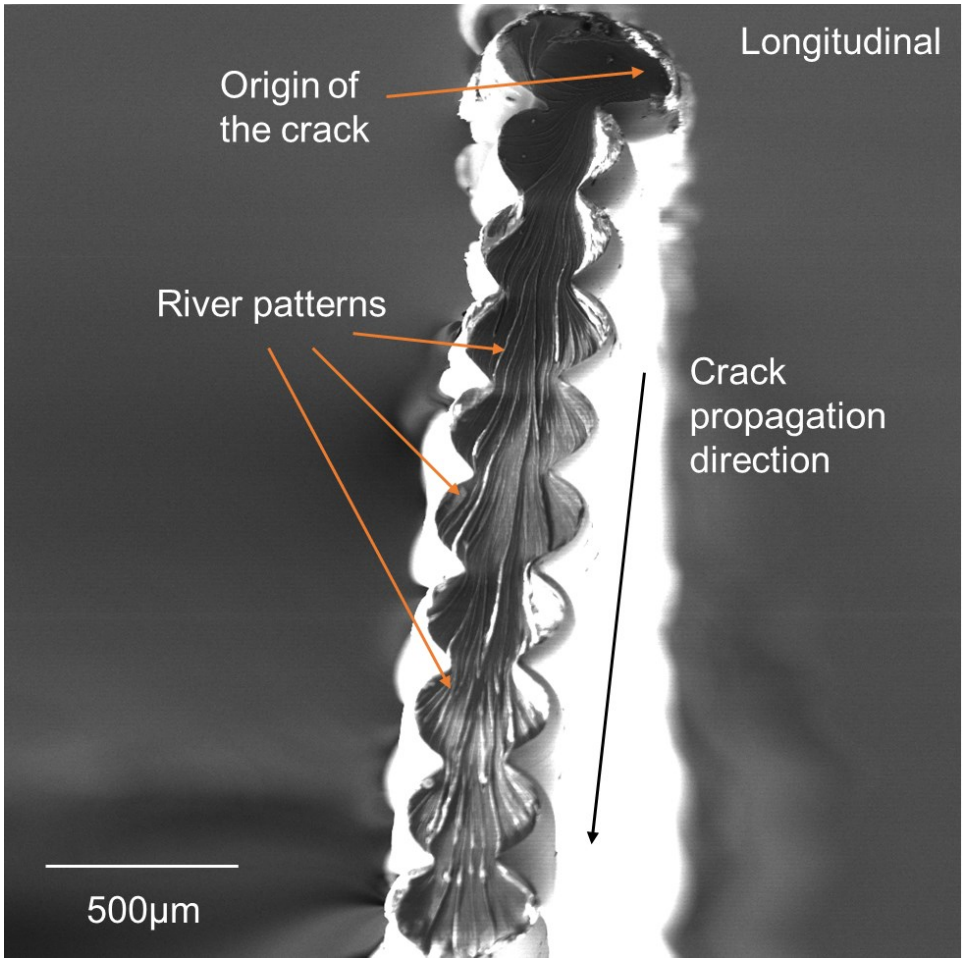

Figure 3.2: SEM image of the fracture surface after longitudinal test.

From fractography theory, the river patterns are formed due to localized plastic deformation, and they could occur in both fast, brittle fractures and in slow, more ductile fractures [87]. While as mentioned above, from macroscopic observation, here the longitudinal tensile specimens exhibit ductile fractures. Tracing back from the crack propagation direction, we could identify a relatively smoother region as the crack origin. An SEM image with higher magnification is shown here (Figure 3.3), from which we could see the flat and smooth mirror zone followed by the river patterns. In fractography, the mirror zone represents the remnant of a ruptured craze (pre-crack structure), which eventually grows and becomes crack under the mechanical loading [87].

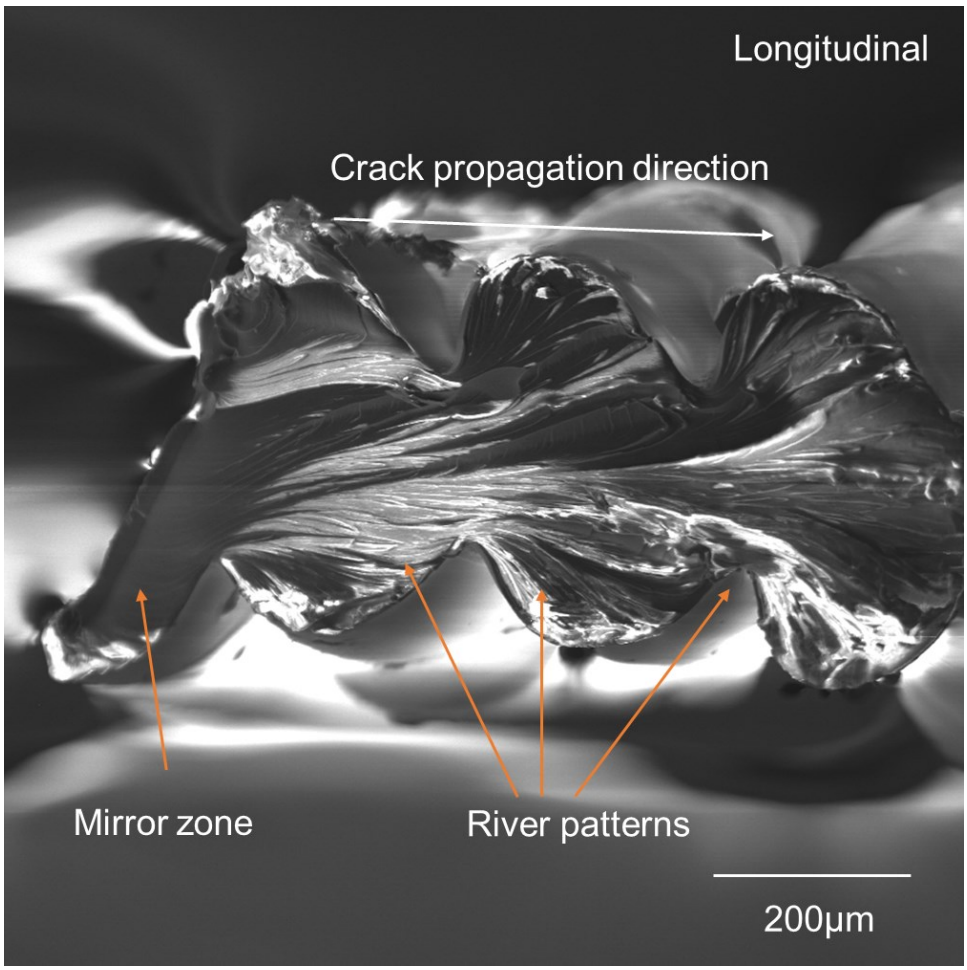

Figure 3.3: Magnified SEM image of the fracture surface after longitudinal test.

For transverse tests, both mirror zone (low plasticity) and non-smooth regions (high plasticity) are observed within the fracture surface, as Figures 3.4 and 3.5 show (two SEM images were shown for each case to show the reproducibility, same in Chapter 4). However, compared to the longitudinal tests, there is less plastic deformation, and hence the macroscopic fracture behavior is more like a brittle material. Previous literature has suggested that there could be mixed stress states (plane stress and plane strain) at the crack front [87], which could be one of the potential reasons of the different failure modes.

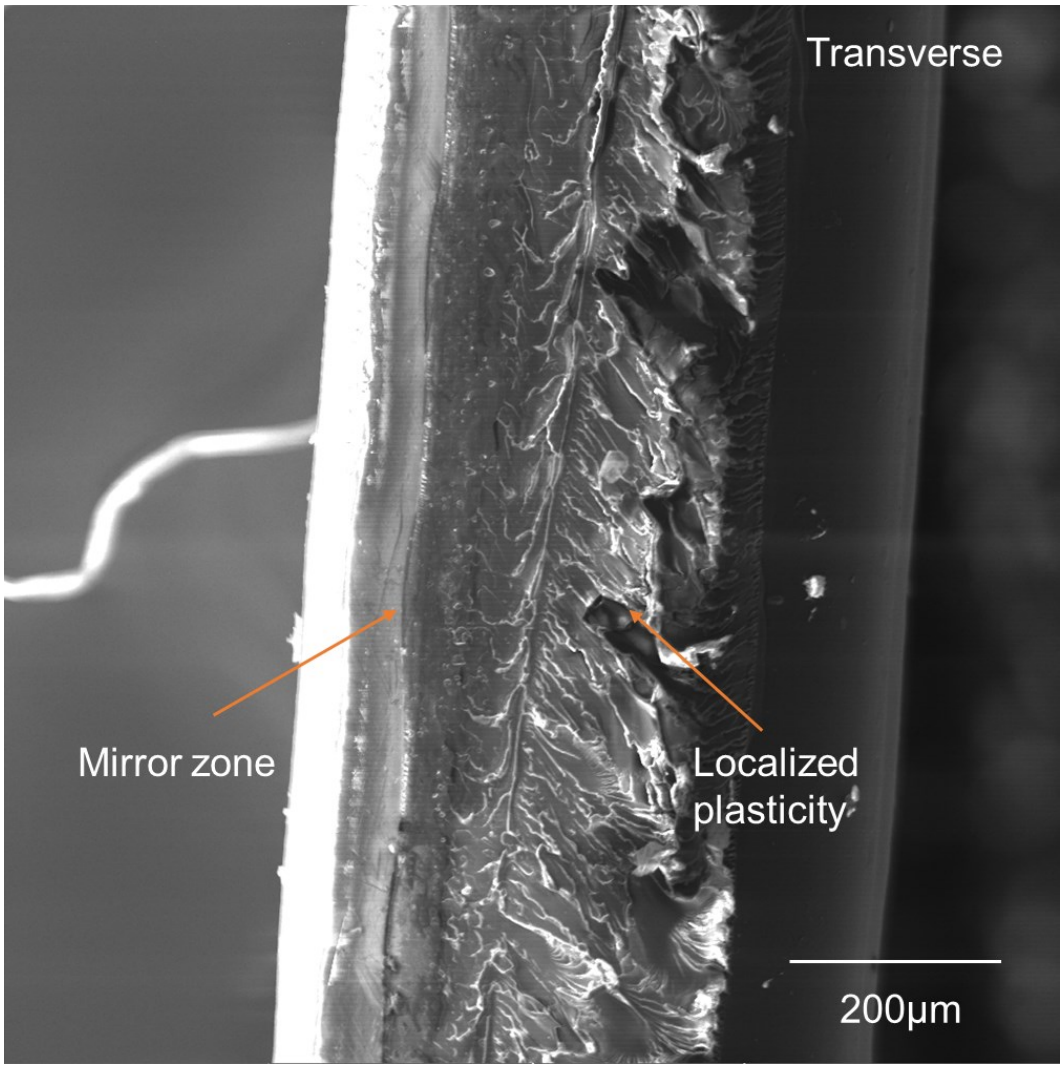

Figure 3.4: SEM image of the fracture surface after the transverse test.

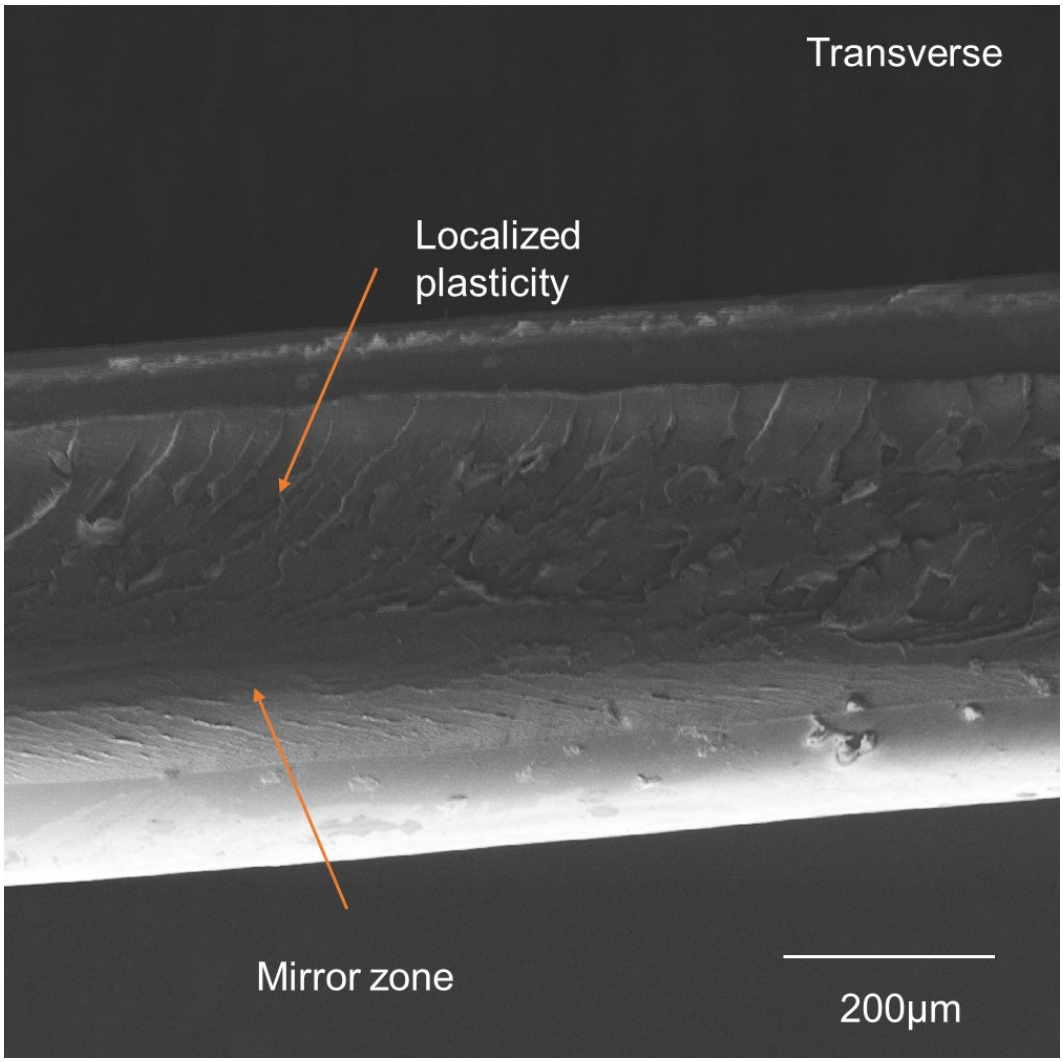

Figure 3.5: SEM image of another fracture surface after the transverse test.

3.3.1 Effects of varying layer height

Samples with different layer heights ranging from 0.05 mm to 0.45 mm were prepared and scanned by micro-CT. From Y-Z cross-sections of the reconstructed 3D model, we could obtain the pixel-to-pixel distribution of road widths along the stacking direction (Z direction). As shown in Figure 3.6, the maximum road width (the maximum value of the average road width within each layer) remained almost constant across different layer heights, while the average bond width decreased slightly with increase of

layer height. For all scanned samples printed at 100% flow index, the average widths were always larger than the designed wall width of 0.5 mm, indicating over-extrusion, which could be compensated by tuning flow parameters, as discussed in Chapter 3.3.4. The most significant change happened on the bond width (minimum road width within two adjacent layers). The bond width decreased steadily as layer height increased: since material sections were circular when extruded, and they will have less contact with larger layer height. The reduction of bond width influences the mechanical behavior of printed products, reducing both Young's modulus and tensile strength.

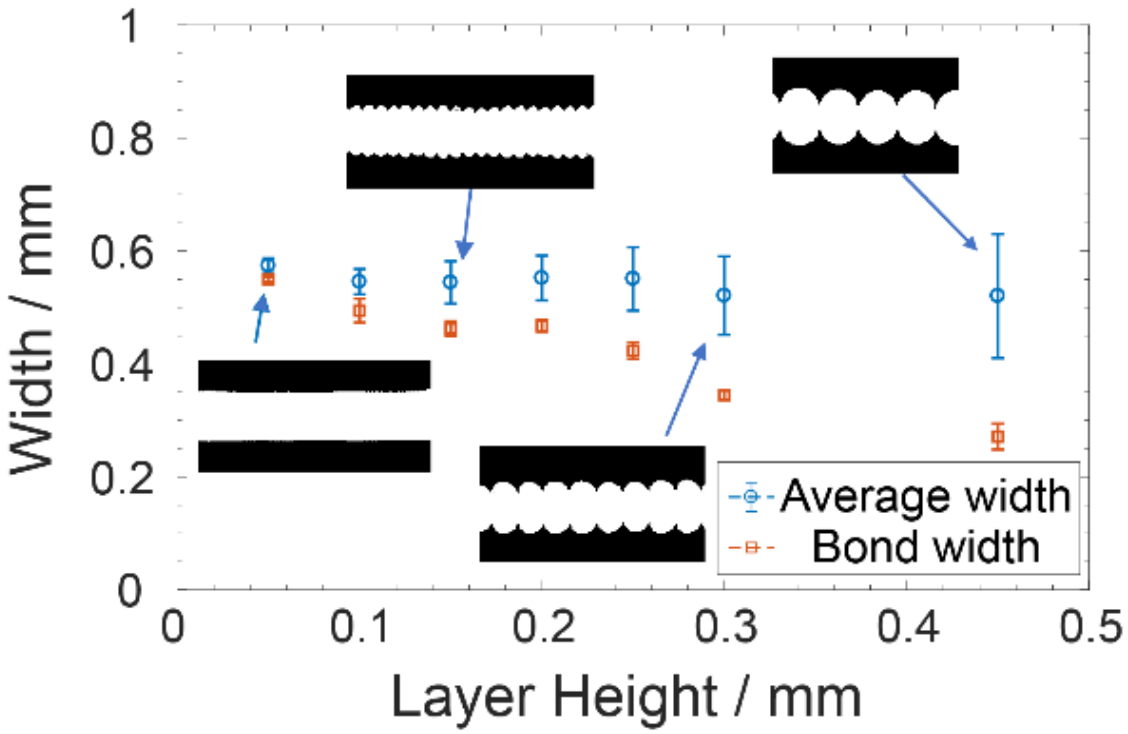

Figure 3.6: Geometrical effects of changing layer height. The error bars are from standard deviations of data obtained from 5 specimens.

Uniaxial tensile tests were performed on samples with 0.15 mm, 0.30 mm, and 0.45 mm layer height, and results were given in Table 3.1. For longitudinal tests along the printing direction, all stress-strain curves were calculated and plotted in Figure 3.7(a). All fifteen tested samples showed very similar stress-strain relationships, and the nominal ultimate tensile strengths (UTS) were 6 % smaller than that of the bulk PC, while the Young's moduli were close to that of the bulk PC, as Figure 3.7(b) shows.

Table 3.1: Tabulated results of uniaxial tensile tests on specimens with different layer heights.

Layer height	**Nominal UTS (MPa)**	**Young's Modulus (GPa)**
0.15 mm - longitudinal	65.80 ± 3.27	1.76 ± 0.02
0.3 mm - longitudinal	64.46 ± 2.49	1.79 ± 0.05
0.45 mm - longitudinal	66.66 ± 1.88	1.81 ± 0.05
0.15 mm - transverse	39.67 ± 1.99	1.79 ± 0.03
0.3 mm - transverse	32.01 ± 2.45	1.52 ± 0.06
0.45 mm - transverse	25.56 ± 1.02	1.22 ± 0.08

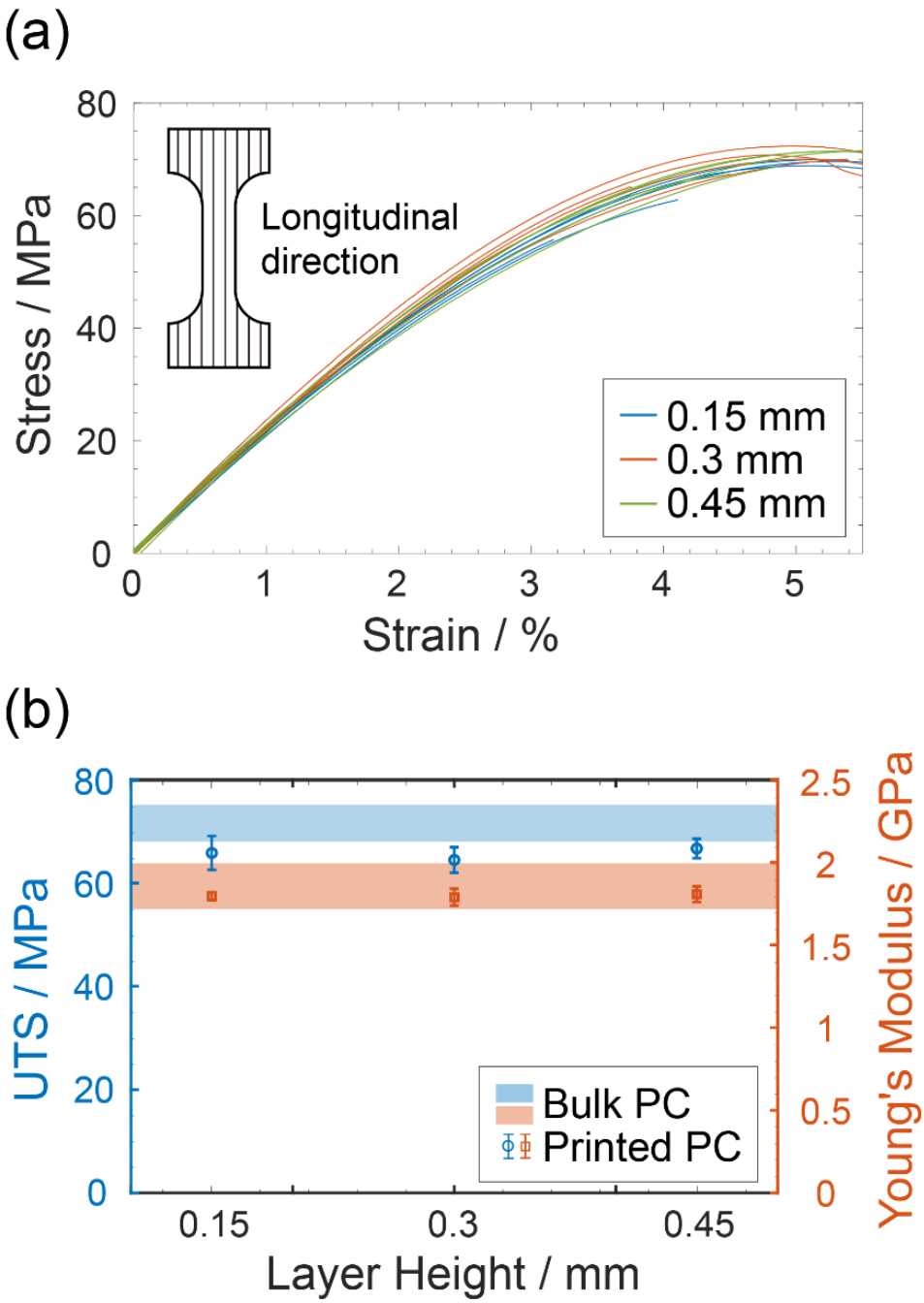

Figure 3.7: Mechanical effects of changing layer height. (a) Stress-strain curves of longitudinal tests. (b) Ultimate tensile strength and Young's modulus results of longitudinal tests. The error bars are from standard deviations of data obtained from 5 measurements.

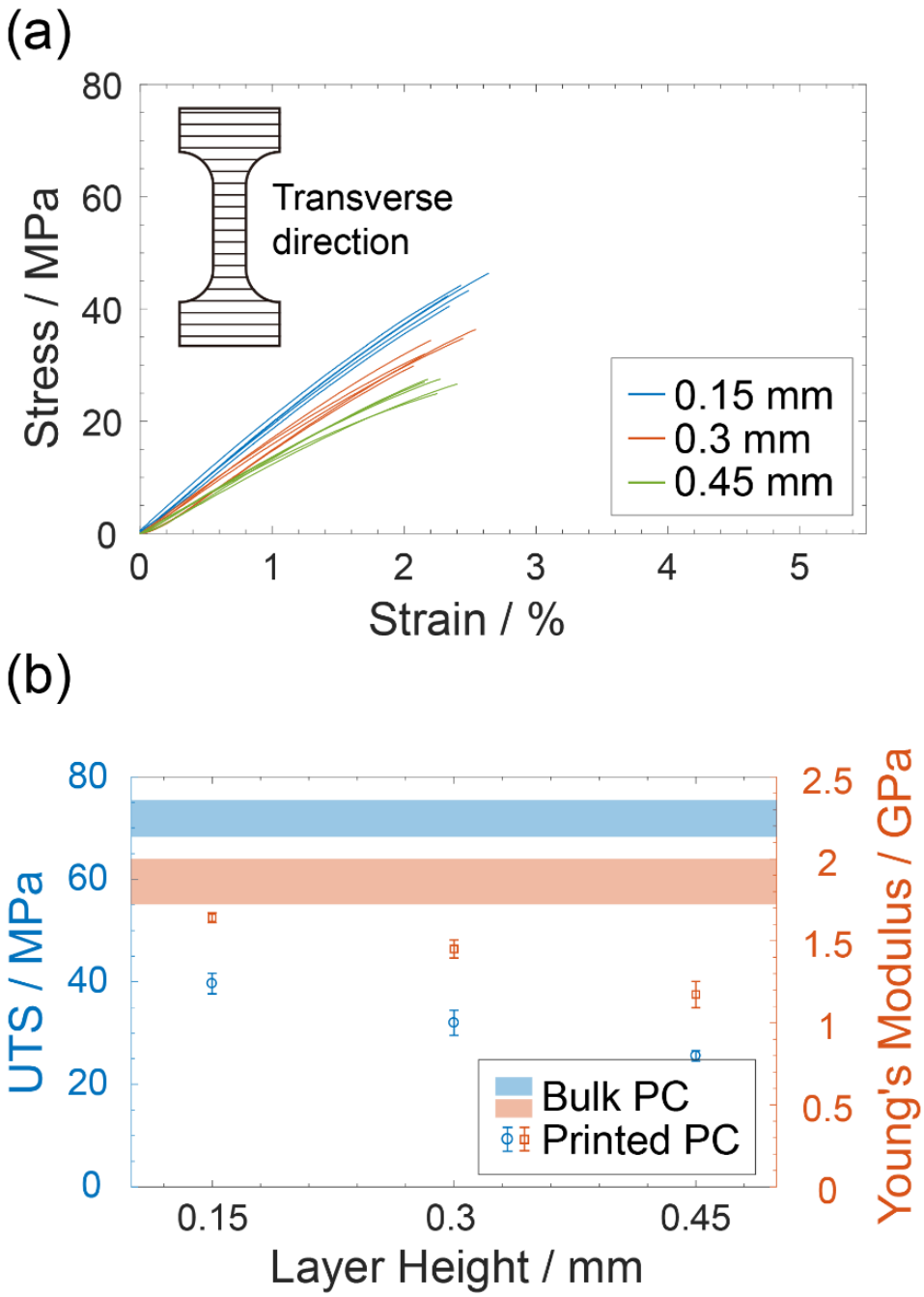

Figure 3.8: Mechanical effects of changing layer height. (a) Stress-strain curves of transverse tests. (b) Ultimate tensile strength and Young's modulus results of transverse tests. The error bars are from standard deviations of data obtained from 5 measurements.

For transverse tests perpendicular to printing direction, the stress-strain curves for three different layer heights tend to group by layer height, as shown in Figure 3.8(a). For nominal UTS (equal to fracture strength here) and Young's moduli, both values decreased with increasing layer height (Figure 3.8(b)), which is consistent with the bond width decrease observed above. To correct for the decrease in bond width, the area measured from micro-CT was used to calculate an actual UTS and Young's modulus (Figure 3.9(a) and Table 3.2). Interestingly, we found that for different layer heights, there is only a slight increase of the mechanical strength at the bonding region, and the absolute values are around 30 % smaller than bulk PC's strength while the fracture strain was approximately 2.4 % for all samples, as plotted in Figure 3.9(b). This indicates the bonding area change is the main reason for strength reduction for different layer heights, and we could potentially predict the strength change by measuring the area of the bonding region. While for the Young's modulus, all sections contribute to it, so that using bond width to normalize it will give unrealistic high values, this will be discussed more in Chapter 5.

Table 3.2: Tensile test results normalized by bond width.

Layer height	**Normalized UTS (MPa)**	**Fracture strain (%)**
0.15 mm - transverse	49.46 ± 2.48	2.48 ± 0.13
0.3 mm - transverse	50.08 ± 3.83	2.30 ± 0.19
0.45 mm - transverse	54.13 ± 2.15	2.25 ± 0.10

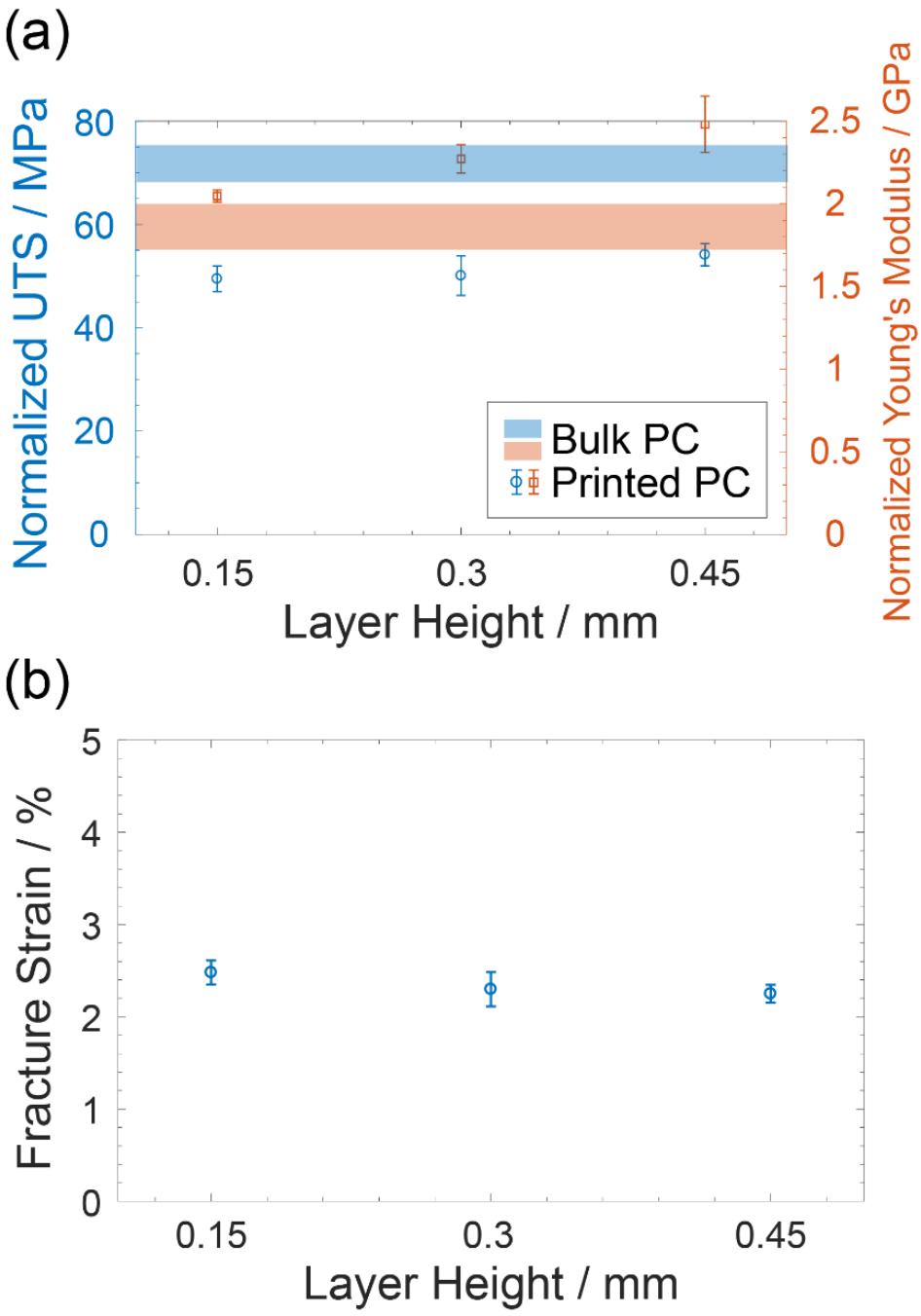

Figure 3.9: Mechanical effects of changing layer height. (a) Transverse tests ultimate tensile strength normalized by scanned cross-section area. (b) Fracture strain of transverse tests. The error bars are from standard deviations of data obtained from 5 measurements.

For nominal UTS, the fracture happens at the narrowest bond so that the bond width could be utilized to explain the mechanical change and calculate the mechanical strength at the bonding region (Figure 3.9(a)). For the reduction of modulus, the qualitative reason is the same: the narrower bond decreases the entire specimen's stiffness. However, the quantitative explanation of modulus change is much harder, as both narrow and wide parts contribute to elastic deformation: neither the average width nor bond width completely capture the elastic response. As shown in Figure 3.6 and Figure 3.8(b), The change of Young's modulus is not a simple linear function of bond width: for the 0.15 mm layer height, the modulus is similar to that of bulk PC; for the 0.45 mm layer height, the modulus is reduced by 30 %, but the bond width is reduced by 60 %. As mentioned in the literature, multiple factors could influence the as-printed modulus, including geometrical dimensions and nozzle exit pressure [15], [88]. For this modulus change, further analysis is described in Chapter 5.

3.3.2 Effects of varying nozzle temperature

To study the effects of changing nozzle temperature, samples printed between 230 °C and 290 °C with 10 °C increments were scanned by micro-CT and analyzed. As Figure 3.10 shows, there was no significant change in the exterior geometry within this temperature range. Both the average and extreme values of road width remained similar.

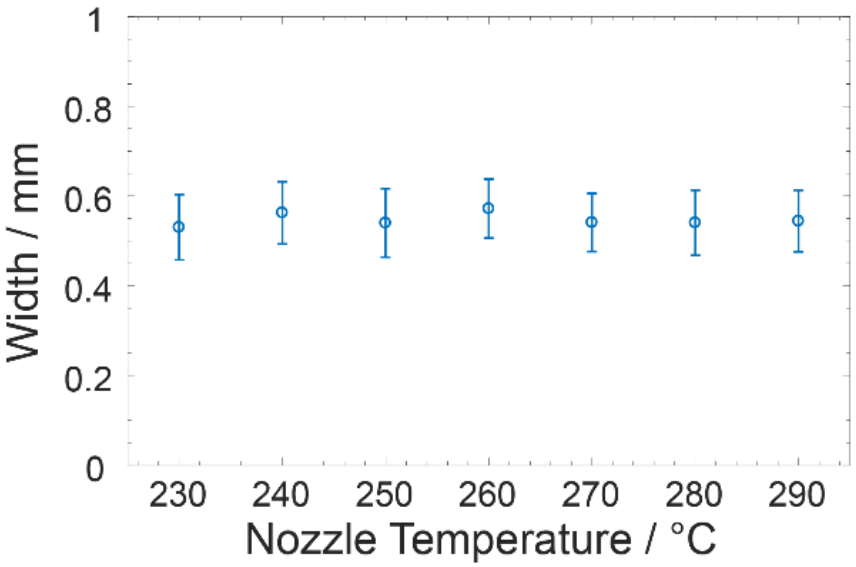

Figure 3.10: Geometrical effects of changing nozzle temperature. The error bars are from the standard deviation of data obtained from 5 measurements.

For each nozzle temperature, ten dogbone specimens were prepared and tested, with five of them stretching along the printing direction (longitudinal) and the others perpendicular to the printing direction. For longitudinal tests, similar stress-strain curves were observed, and no significant influence on nominal UTS and Young's modulus was found (Figure 3.11(a)-(b) and Table 3.3). The values of strength and modulus were close to those of bulk PC. However, the nozzle temperature affected the mechanical properties of samples loaded perpendicular to the print direction. As shown in Figure 3.12(a)-(b) and Table 3.4, Young's moduli did not show a clear trend with increasing nozzle temperature, while the nominal UTS increased with nozzle temperature at first, then reached a plateau after 250 °C. As shown in Figure 3.10, no significant bond width change was observed for those samples, so that the strength loss below 250 °C should be due to other reasons, for example, the different thermal history. As stated in Chapter 1.2.1, the welding quality

between two adjacent layers heavily depends on the welding time, i.e., the duration that the interlayer region remains hotter than the glass transition temperature [26]–[29].

Table 3.3: Tabulated results of tensile tests on longitudinal specimens printed with different nozzle temperatures.

Nozzle temperature	UTS (MPa)	Young's Modulus (GPa)
230 °C - longitudinal	64.51 ± 2.26	1.69 ± 0.05
240 °C - longitudinal	61.56 ± 1.73	1.78 ± 0.06
250 °C - longitudinal	63.88 ± 0.97	1.74 ± 0.04
260 °C - longitudinal	59.75 ± 1.30	1.65 ± 0.03
270 °C - longitudinal	63.32 ± 2.63	1.71 ± 0.07
280 °C - longitudinal	64.46 ± 2.49	1.79 ± 0.05
290 °C - longitudinal	63.60 ± 1.98	1.69 ± 0.04

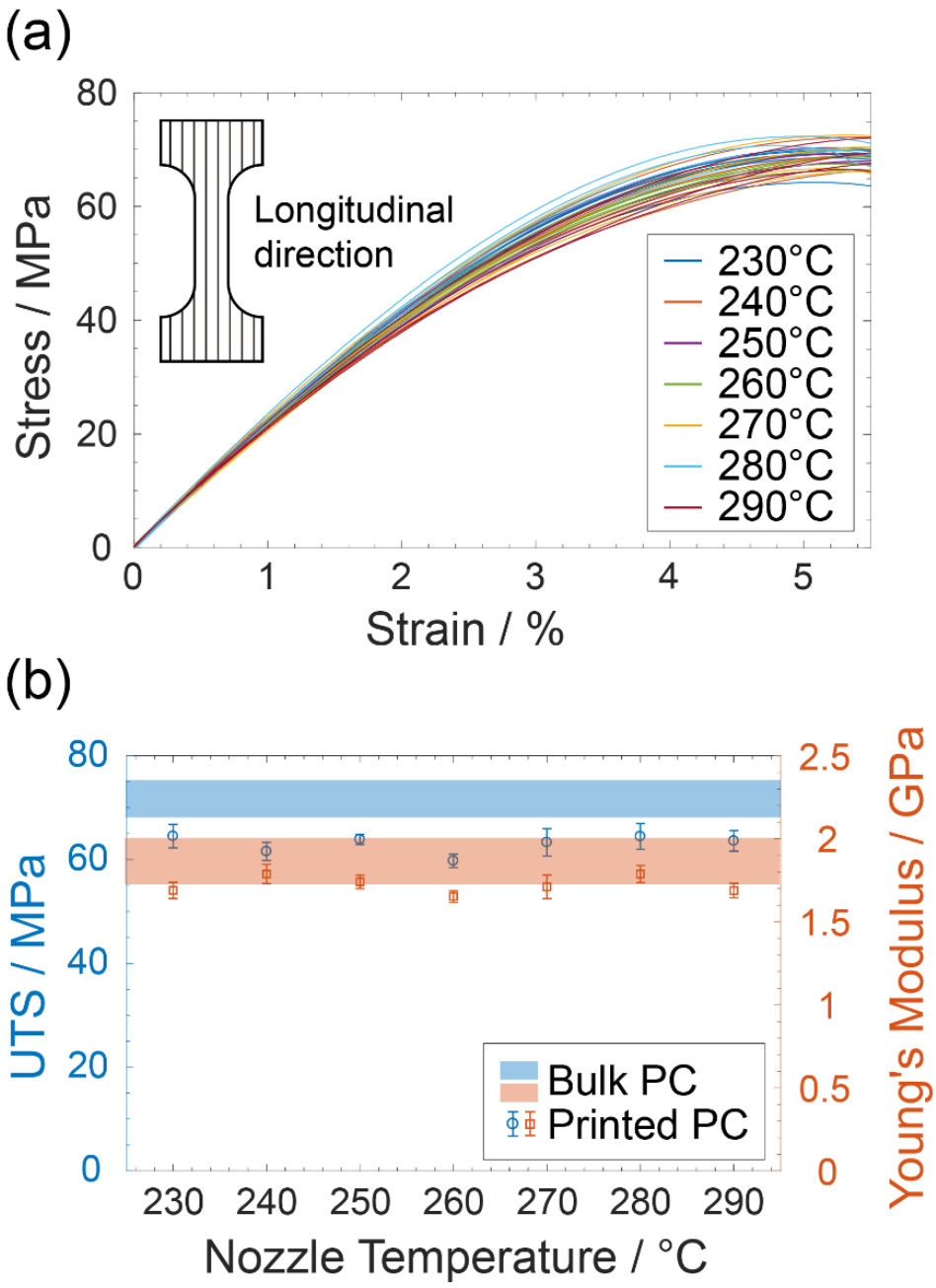

Figure 3.11: Effects of the nozzle temperature on mechanical properties. (a) Stress-strain curves of longitudinal tests. (b) Ultimate tensile strength and Young's modulus results of longitudinal tests. The error bars are from standard deviations of data obtained from 5 measurements.

With higher nozzle temperature, the welding time will be longer, and the weld quality will be better. However, once enough interdiffusion and re-entanglement have occurred across the interface and reached equilibrium, longer welding times will not further increase the strength. Previous literature [14], [30] have shown that for ABS and PLA, there are also similar increasing trends of mechanical strength with higher fabrication temperatures, as well as the slowing down in strength increase at certain temperature points. While the different molecular weights could contribute to the minor deviations in this phenomenon considering the chain mobility differences.

Table 3.4: Tabulated results of tensile tests on transverse specimens printed with different nozzle temperatures.

Nozzle temperature	**UTS (MPa)**	**Young's Modulus (GPa)**
230 °C - transverse	17.63 ± 4.71	1.44 ± 0.03
240 °C - transverse	21.13 ± 3.07	1.60 ± 0.04
250 °C - transverse	31.27 ± 3.76	1.54 ± 0.09
260 °C - transverse	26.16 ± 5.49	1.40 ± 0.04
270 °C - transverse	28.97 ± 3.51	1.55 ± 0.07
280 °C - transverse	32.01 ± 2.45	1.52 ± 0.06
290 °C - transverse	28.02 ± 3.97	1.57 ± 0.05

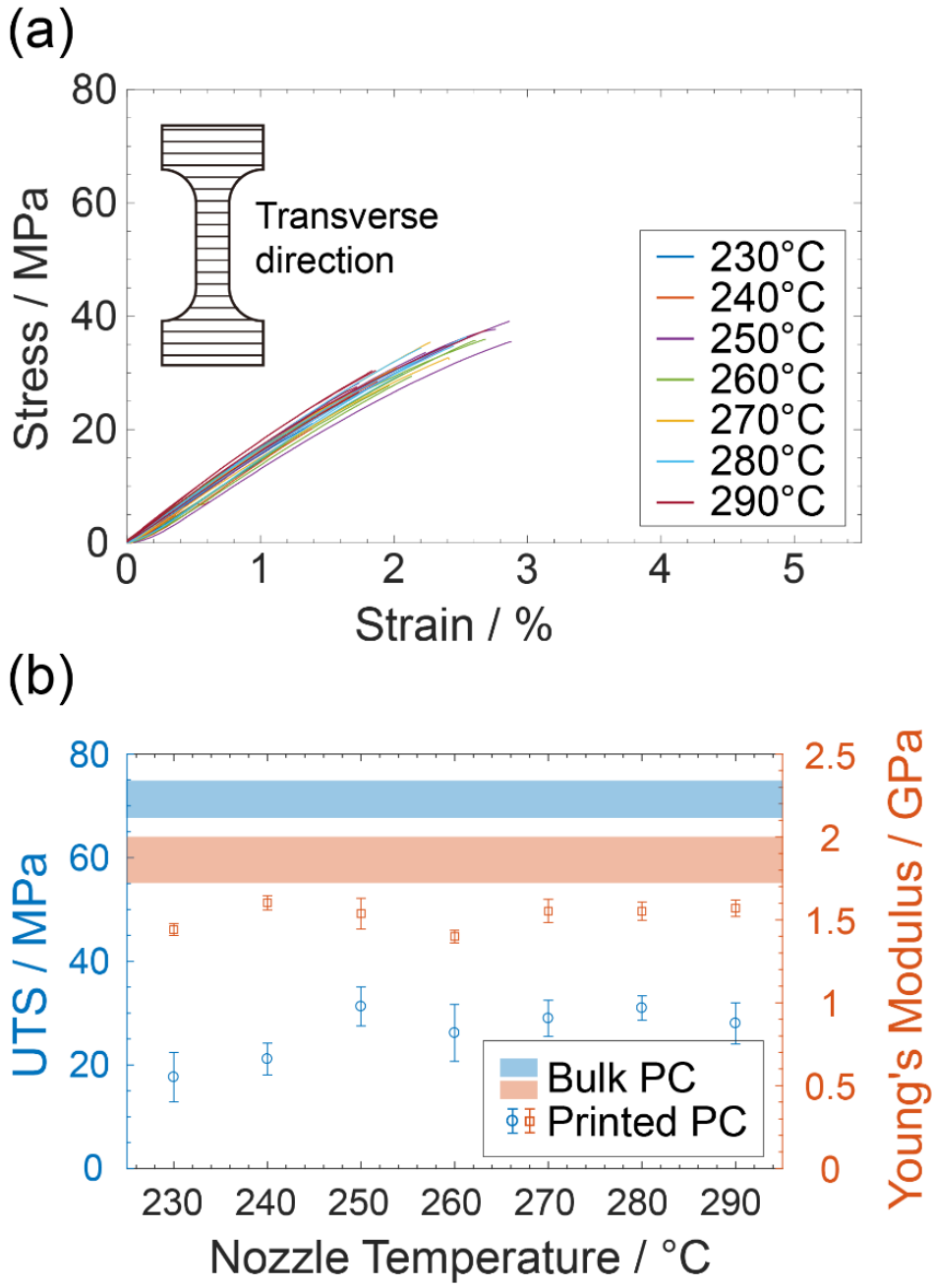

Figure 3.12: Effects of the nozzle temperature on mechanical properties. (a) Stress-strain curves of transverse tests. (b) Ultimate tensile strength and Young's modulus results of transverse tests. The error bars are from standard deviations of data obtained from 5 measurements.

3.3.3 Effects of varying print speed

To study the effects of different print speeds, specimens with print speed ranging from 10 mm/s to 30 mm/s were fabricated, and their geometrical and mechanical properties were characterized. As shown in Figure 3.13, geometrical defects could be visually observed for high print speeds. Visible defects appeared on the surface of 20 mm/s print speed sample, and there was significant waviness when print speed reached 30 mm/s sample. From micro-CT scans, the defects on the 30 mm/s samples could be quantified as the periodical change of road width along the printing direction: the wavelength was around 4 mm, and the amplitude was around 0.2 mm (Figure 3.14). From our speculations, the potential causes of this defect are insufficient bonding between the first layer and the build plate, as well as flow instability. When printing at high print speed, the mismatch between nozzle moving speed and nozzle extrusion speed causes the very first layer to be dragged, experiencing high shear rate between the fast-moving upper part and the static bottom part, which can further cause insufficient bond with the build plate and then the meandering shape of the deposited extrudates.

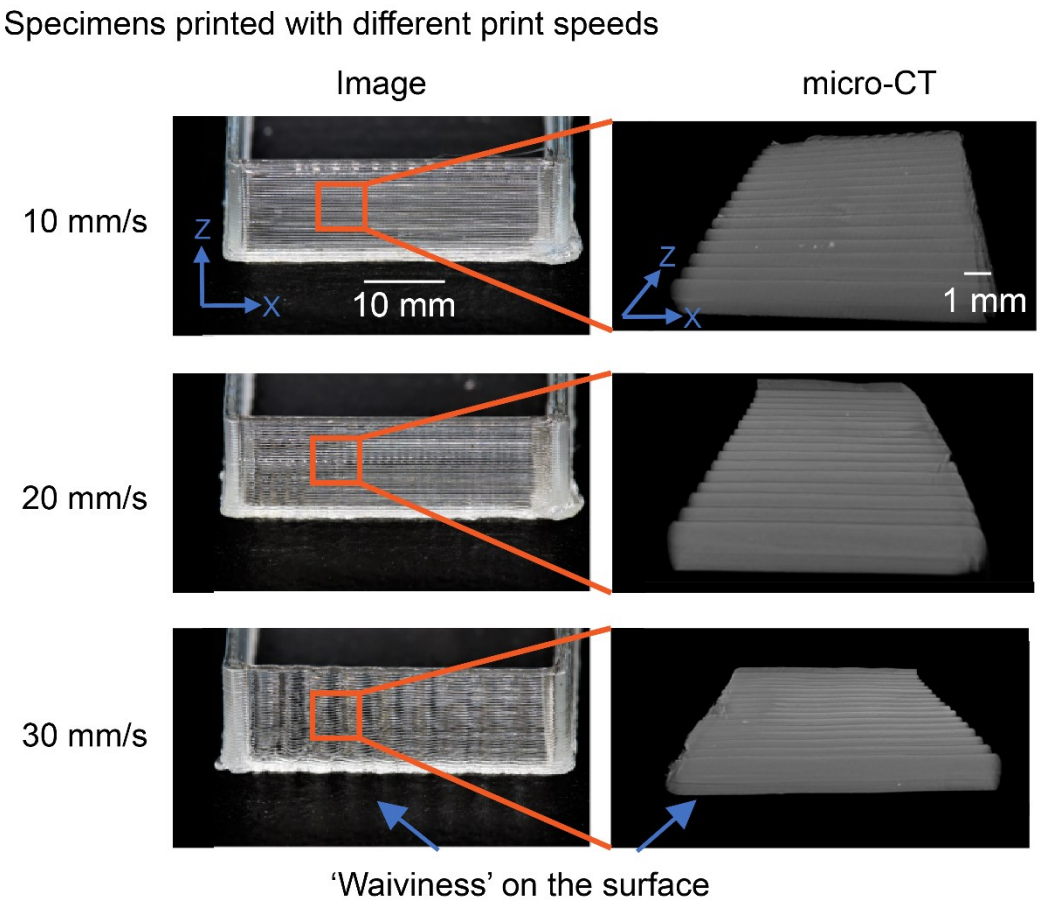

Figure 3.13: Geometrical effects of changing print speed, defects start to appear at higher print speed.

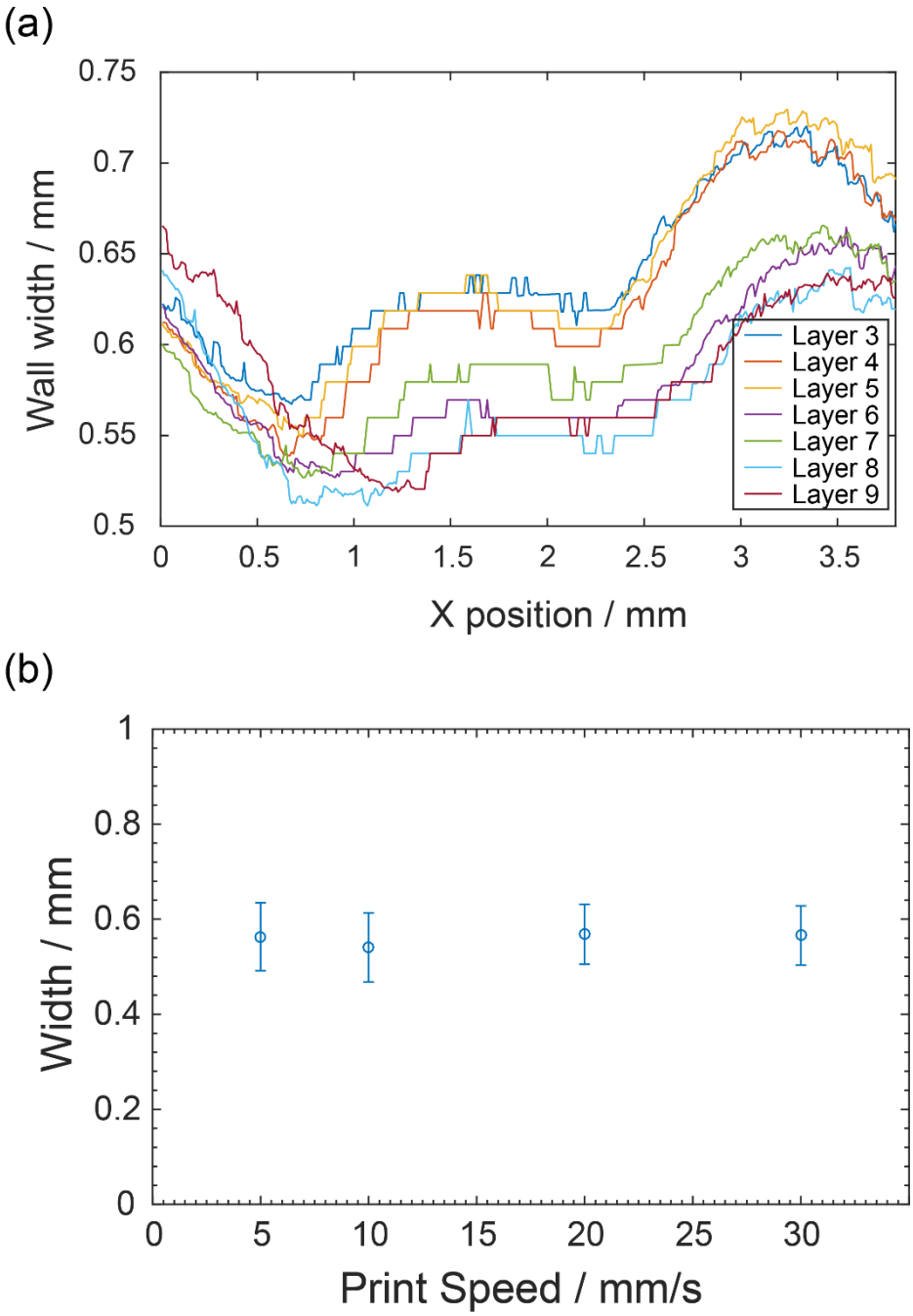

Figure 3.14: (a) The micro-CT analysis of wavy patterns appeared for the 30 mm/s print. (b) Width of the specimens with changing print speed. The error bars are from standard deviations of data obtained from 5 measurements.

Interestingly, no significant mechanical performance change was observed for samples with different print speeds, even with severe geometrical defects (Table 3.5). As Figures 3.15 and 3.16 show, for both longitudinal and transverse tests, the nominal UTS and Young's moduli only have slight changes across multiple print speeds ranging from 10 mm/s to 30 mm/s. These results could be due to the similar bond width and bonding quality within the tested range despite the waviness defects, as shown in Figure 3.14(b). Also, the trends are consistent with previous works [59], which suggests the mechanical performance remains similar before reaching a very high printing speed (~100 mm/s).

Table 3.5: Tabulated results of tensile tests on specimens printed with different print speeds.

Print speed	**Nominal UTS (MPa)**	**Young's Modulus (GPa)**
10 mm/s - longitudinal	64.46 ± 2.49	1.70 ± 0.05
20 mm/s - longitudinal	60.47 ± 0.78	1.75 ± 0.04
30 mm/s - longitudinal	60.15 ± 1.00	1.65 ± 0.03
10 mm/s - transverse	32.01 ± 2.45	1.52 ± 0.06
20 mm/s - transverse	30.55 ± 2.97	1.49 ± 0.06
30 mm/s - transverse	27.45 ± 5.34	1.51 ± 0.05

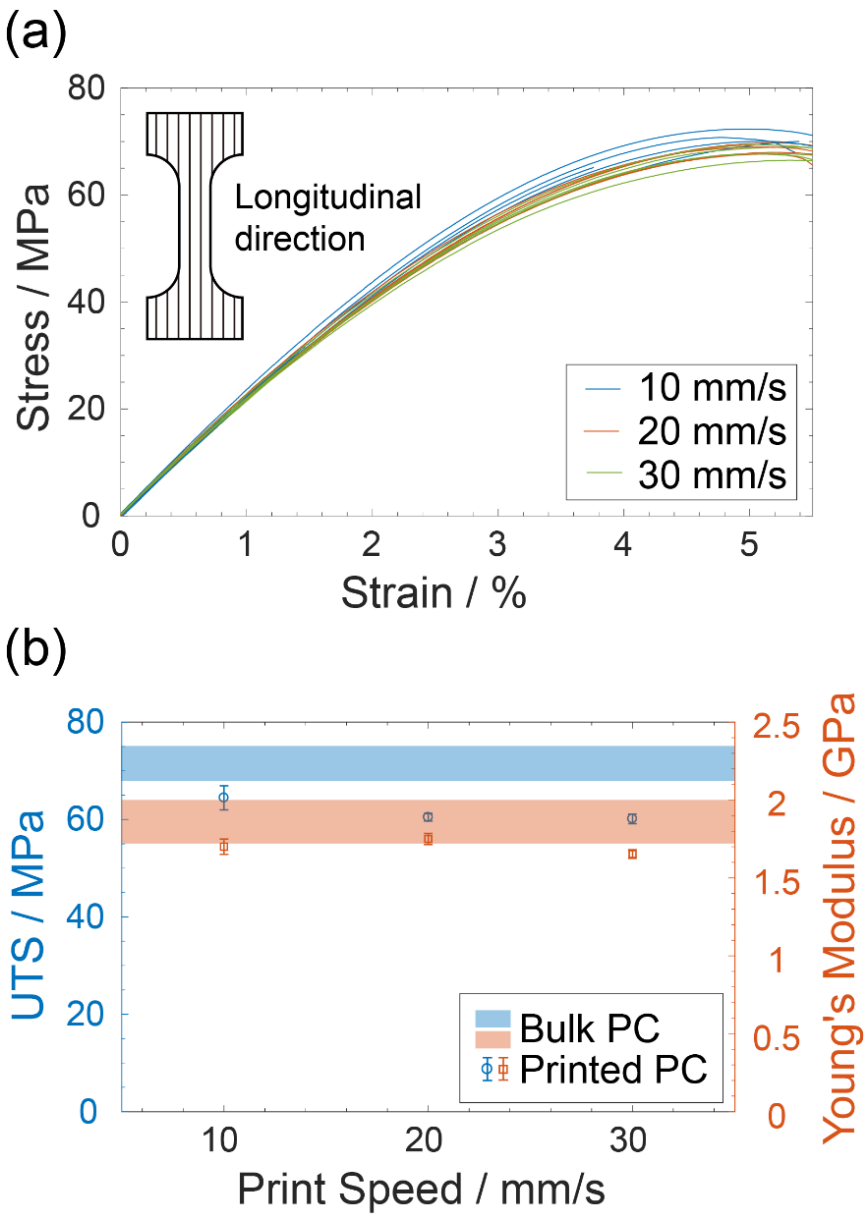

Figure 3.15: Mechanical effects of changing print speed. (a) Stress-strain curves of longitudinal tests. (b) Ultimate tensile strength and Young's modulus results of longitudinal tests. The error bars are from standard deviations of data obtained from 5 measurements.

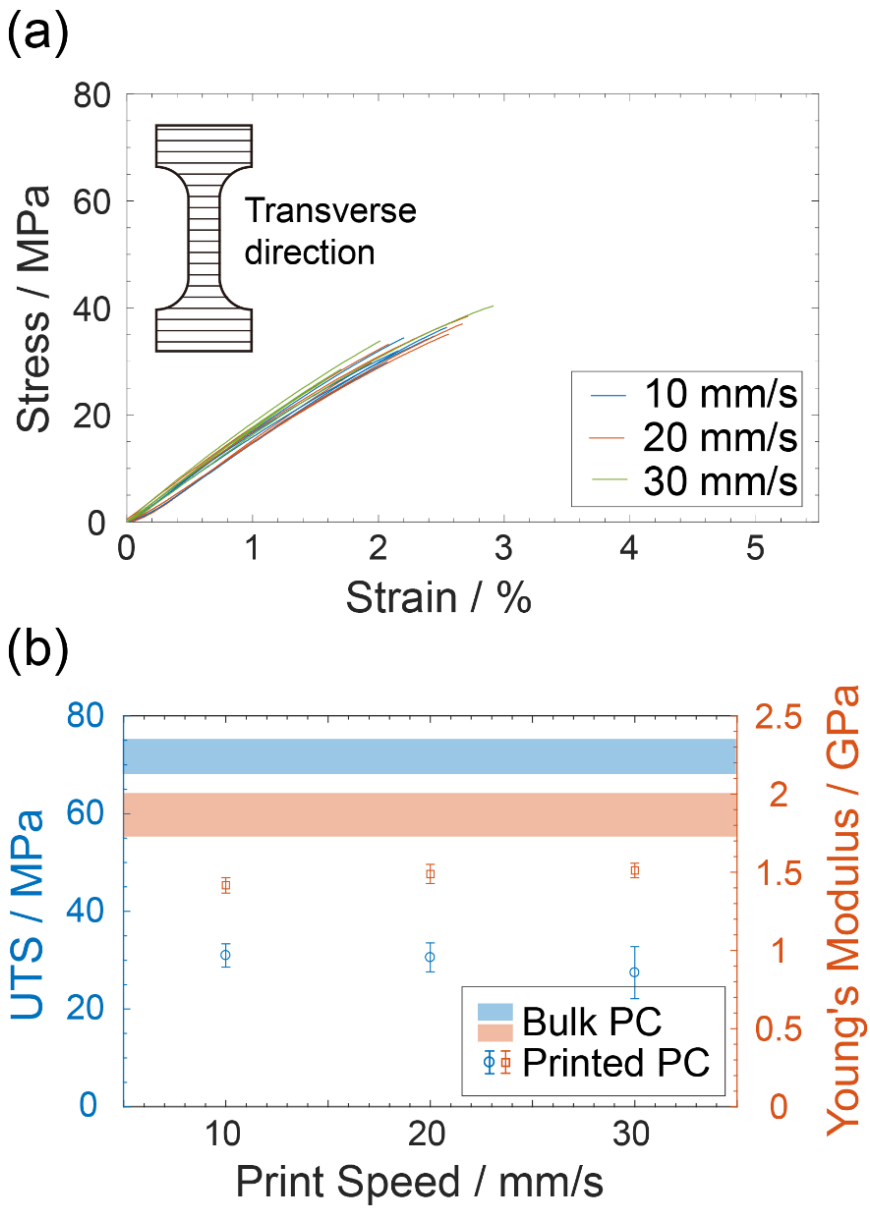

Figure 3.16: Mechanical effects of changing print speed. (a) Stress-strain curves of transverse tests. (b) Ultimate tensile strength and Young's modulus results of transverse tests. The error bars are from standard deviations of data obtained from 5 measurements.

3.3.4 Compensation of over-extrusion

As mentioned in Chapter 3.3.1, over-extrusions have been found in all printed samples. It could be a fabrication defect that varies from machine to machine. Due to die-

swell effects, the volume control of extruded polymer is very sensitive to the normal stress, which is in turn sensitive to the capillary contraction, feed rate, and temperature [88]. Hence small geometry or control errors in mechanical assembly or/and stepper motors could result in significant over-extrusions. To compensate for those errors, we tuned the printing parameters as follows. For example, for the target width of 0.5 mm, the average road width measured by micro-CT was 0.523 mm. Since there is 4.6 % over-extrusion compared with the target dimension, we tuned the flow index to 95.6 % to limit the material feed and compensate the over-extrusion. After adjusting the flow index, we found the average road width changed to 0.504 mm, which gives much better geometrical accuracy with 0.8% deviation from the intended dimension. As shown in Figure 3.17, the specimen printed with a compensated flow index is slimmer than the original settings. Through micro-CT scans and image processing, its average fiber width (0.504 mm) is much closer to the target width (0.5 mm), which indicates the over-extrusion defect is successfully mitigated. By using this method, both printer users and manufacturers could fine-tune the settings for higher printing precision.

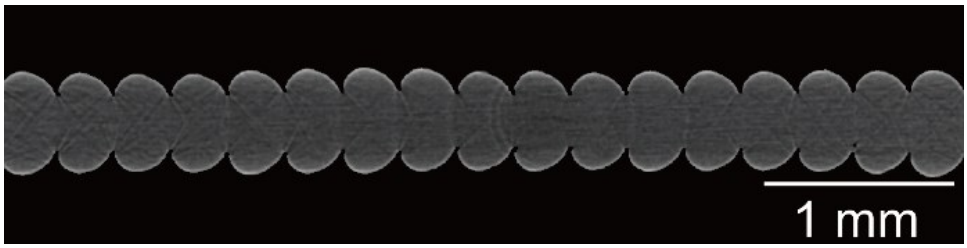

Figure 3.17: Scanned cross-section of a specimen printed with an optimized flow index.

3.3.5 Discussions of results

In Chapter 3.3.1, the increase of tensile strength with decreasing layer height has been quantified and analyzed. From mechanical tests, the mechanical strength at the bonding region is measured to be around 30 % less than PC's intrinsic property, which makes the transverse direction always weaker than the longitudinal direction. Then, combining with the micro-CT scan results, it is found that the geometry change at bonding regions further differentiates the strength of specimens printed with different layer heights. With higher layer height, the scalloping shape gives more variations in the width and produces narrower bonding regions. As a result, the narrow bonds serve as the weakest part with stress concentrated there, and the bonds will deform and fracture earlier and reduce the specimen's strength. Based on the findings, decreases in layer height could be an easy way to improve mechanical performance, while users will suffer from extended printing time. Depending on different applications, a balance between strength and speed can be optimized. Meanwhile, the change in Young's modulus opens a possible method for controlling the modulus of the printed product by varying printing parameters like layer height.

In Chapter 3.3.2, the effects of varying nozzle temperatures were measured. For the PC filaments used in this study, the optimal nozzle temperature is above 250 °C, which is similar to the recommended value from the manufacturer. Lower nozzle temperatures significantly reduce the transverse mechanical strength. In practice, users may find the material is still printable using printers that cannot reach designated nozzle temperature, but the mechanical performance could be compromised.

In Chapter 3.3.3, it is shown that high print speed may lead to periodic geometry variations in printed products, while it did not harm the mechanical performance within the tested range. This finding suggests that if there is less requirement on geometric accuracy, increasing print speed could be a good method to improve printing efficiency while maintaining satisfactory mechanical performance, as the bonding area remains similar. However, if a smooth and flat exterior surface is desired, print speed should be limited to get good geometrical accuracy. Considering the main cause of waviness defect is poor bonding quality of the first layer, a potential solution could be tuning printing parameters of the first layer separately, which is an available function in multiple pre-printing slicer software.

From our perspective, the mechanical performances of FFF specimens are directly controlled by the printed structures as well as the physical and chemical changes that occur during printing. However, the structural and property changes may not be sensitive to some printing parameters, which results in the insensitivity to those parameters. For varying print speed, the waviness defect shown in Figure 3.10 does not influence the bonding area between two adjacent layers within the test range so that there is minimal effect on mechanical properties. For varying nozzle temperature, while the macroscopic geometry remains similar, the strength decreases at lower nozzle temperatures, which is due to the changes in microscopic polymer entanglement according to the literature [26]–[29]. Finally, for the layer height, this parameter strongly impacts the as-printed geometries, changing both the bonding area and the uniformity along the stacking direction (Z direction). Thus, it produces the greatest mechanical property changes among the three printing parameters studied.

From these findings, several suggestions for printing parameter selections can be proposed. First, the experiments further prove that a sufficient nozzle temperature should be used to give long enough welding time for a fully developed interlayer bond to have good geometrical and mechanical properties. For the Ultimaker PC used in this study, the recommended minimum nozzle temperature is 250 °C. Next, machine-related extrusion error may cause under- or over-extrusion of printing materials, and this can be compensated by measuring the extruded volume and tuning the flow index. For our LulzBot TAZ 6 printer and LulzBot Hexagon hot end tool head, reducing the flow index by 4.4 % provided better accuracy, resulting 0.8 % error in geometric dimensions. Last, but most importantly, varying layer height and print speed will have a tradeoff of printing time, geometrical accuracy and mechanical performance. Users need to balance between them based on the constraints such as available print time, mechanical strength, and geometric variability.

3.4 Chapter Summary

In this chapter, we conducted both geometrical and mechanical characterizations of FFF-printed parts with varied processing parameters, then analyzed these results to understand the processing-structure-property relationships. First of all, SEM images on fracture surfaces revealed the different levels of plasticity formed during longitudinal and transverse tests, which explained the different fracture modes (slow fracture for longitudinal, fast fracture for transverse). When increasing layer height, the bonding area reduced, and it caused reductions in transverse tensile strength and Young's modulus. The strength change was correlated with geometry changes quantified with micro-CT scan results: the strength showed a linear relationship with the bonding area, while the modulus

change is more complex and will be discussed in Chapter 5. For varying the nozzle temperature, no significant geometrical difference was found, but a minimum threshold of 250 °C was observed to reach maximum mechanical properties. At lower temperatures, the insufficient welding time could reduce the welding quality as polymer chain entanglements were not fully developed. If print speed is increased, there could be periodical geometry error in printed width due to the weaker bonding between the specimen and the build plate, while this geometrical defect did not influence mechanical performance within the range that we tested.

Chapter 4 : Effects of Environmental Conditions

In this chapter, we investigated the influences of changing environmental conditions. For the environmental temperature, in-situ infrared imaging analysis revealed the presence of up to 5.4 °C/mm thermal gradient across the printed specimens when printing using an open-chamber printer and a heated build plate. For the environmental humidity, analysis of X-ray micro-computed tomography (micro-CT) scans showed up to 11.7 % porosity, which is caused by polymer water content absorbed from environmental moisture. Meanwhile, tensile tests showed the mechanical performance loss associated with those defects, but surprisingly the transverse direction ductility may increase at higher porosity. Furthermore, the experimental results are combined with analytical and parametrical studies to explore quantitative relations between environmental conditions and printing quality. Based on the results, quantitative guidelines for estimation of printing quality based on environmental conditions are provided, which would also help users obtain desired printing results with a better understanding of the effects of environmental conditions

4.1 Introduction

As stated in Chapter 1.2, It is widely known that the printing quality of fused filament fabrication (FFF) could be heavily impacted by environmental temperature and humidity, which creates defects including warping and porosity. However, more thorough

and systematic studies are still needed to quantitatively understand those influences. In this study, we investigated those issues step by step. For temperature effects, we firstly measured the temperature field using an infrared camera, and obtained the thermal gradients within specimens printed under different environmental temperatures. Then, from the thermal gradients, we predicted the warping deflection and compared with experimental measurements. Finally, we performed tests to capture the mechanical property changes. For humidity effects, we started with the water absorption test to quantify how much water printed materials can absorb under different levels of humidity. With the water content, we could estimate the corresponding porosity, which was compared with experimental results obtained from micro-CT scans. Eventually, the uniaxial tensile test results were obtained and analyzed together with pore size data and SEM images of fracture surfaces.

4.2 Materials and Methods

4.2.1 Water absorption test of PC

To find out the water absorption properties of PC, a lab balance attached with a Cellkraft P-2 humidifier was used. As Figure 4.1 shows, 20 g of Ultimaker 2.85 mm polycarbonate printing filaments were dried in a vacuum oven at 110 °C for 1 h, then weighted on an OHAUS Pioneer precision lab balance. The chamber of the lab balance was connected to Cellkraft P-2 humidifier, which controlled the air humidity. The weight reading, chamber temperature, and chamber humidity were continuously monitored by a wireless camera for 24 h. The recorded videos further confirmed the temperature fluctuation is less than ± 0.5 °C, and the humidity fluctuation is less than ± 1 % RH.

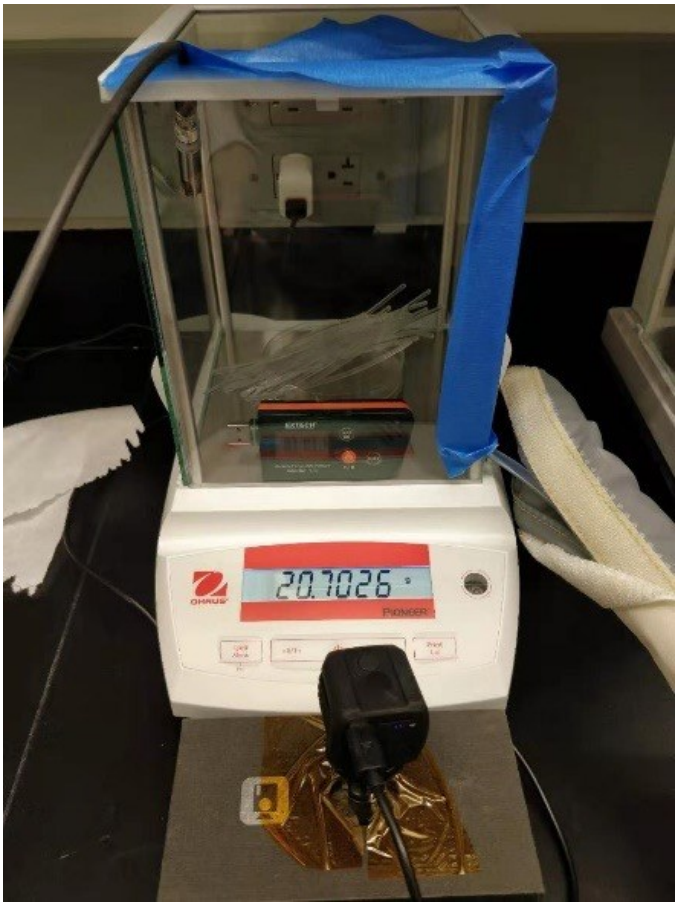

Figure 4.1: Setup of the water absorption test.

Dried PC filaments were then exposed to four different humidity levels (10 % RH, 30 % RH, 50 % RH, 70 % RH) for 24 h to study the water absorption rate, and the resulting filaments with different water contents (0 wt%, 0.05 wt%, 0.10 wt%, 0.15 wt%) were printed and tested.

4.2.2 PC's coefficient of thermal expansion

To model the warping defects, PC's thermal expansion behavior needs to be characterized. A small piece of PC filament was cut out and mounted on TA Instrument Q800 Dynamic Mechanical Analyzer (DMA). The sample was firstly heated up to 140 °C

and then cooled down at a rate of 1 °C/min. The DMA's zero force mode was applied, and the thermal-induced retraction of the specimen was recorded, as plotted in Figure 4.2. Here we could see there is a change in the coefficient of thermal expansion (CTE) around the glass transition temperature due to the phase transition [89], so that the exact CTE at each interested temperature point needs to be fitted. As a reference, it is fitted to be 73 μm/(m·K) below the glass transition region, which correlates well with the data from the manufacturer (70 μm/(m·K)).

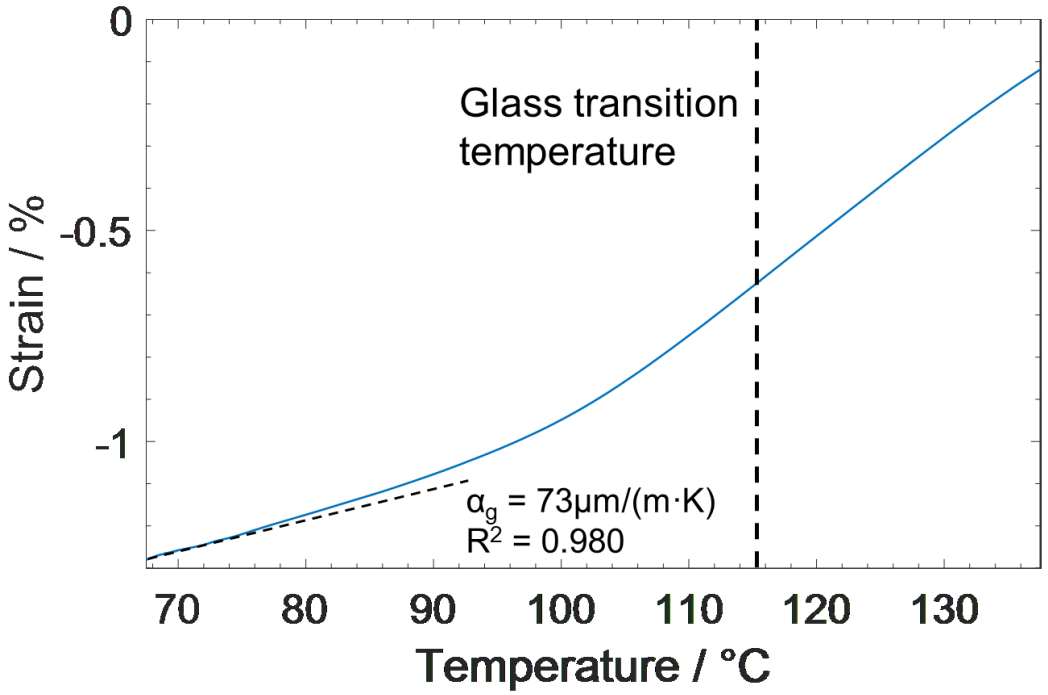

Figure 4.2: Measurements of PC's coefficient of thermal expansion.

4.2.3 Environmental conditions

In addition to the setup described in Chapter 2.1, a space heater (STEGO, Inc.) was mounted inside the chamber and connected to a temperature controller, which can vary the

environmental temperature from room temperature to 90 °C. To study the effects of changing environmental conditions, temperature and humidity were varied separately, i.e., the environment was kept below 10 % RH when studying temperature effects, and the temperature was set at 22 °C when studying humidity effects. Afterward, the corresponding physical and mechanical effects were also investigated. For environmental temperature, four different values (30 °C, 50 °C, 70 °C, 90 °C) were tested: the entire chamber was heated and kept around a target temperature during the printing process. The temperature fluctuation was around ± 5 °C, since the acrylic chamber does not have perfect thermal insulation. Despite the varied environmental conditions, all other printing parameters were kept the same, including layer height (0.3 mm), nozzle temperature (280 °C), print speed (10 mm/s), and build plate temperature (115 °C).

4.2.4 Characterization

In addition to the tensile tests, two other characterization techniques were applied to measure the property changes upon varying environmental conditions. Firstly, for the temperature side, infrared (IR) thermography was used to evaluate the temperature field of the specimen during printing. As Figure 4.3 illustrates, an IR camera (FLIR a6701sc camera with 50 mm F/2.5 lens) was set up in front of the printer, and a round hole was cut out at the front panel of the printer chamber to allow infrared light transmission, since acrylic is not transparent to infrared.

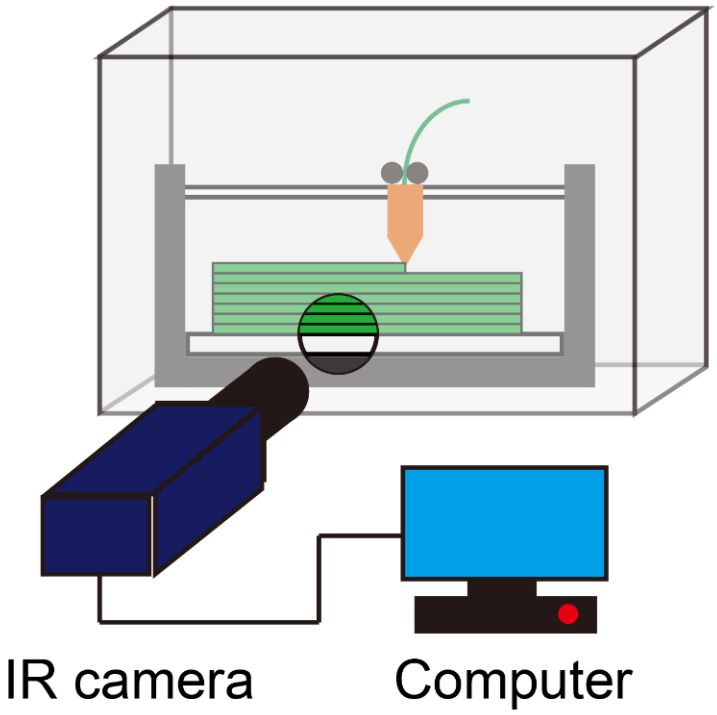

Figure 4.3: Schematic of the infrared thermography system.

To get the best accuracy, calibration of the PC emission spectrum was performed following the procedure described in [90]. As Figure 4.4(a) shows, a small piece of printed PC was put on Linkam THMS600 Thermal Stage, which could precisely control the specimen temperature with 0.1 °C accuracy. The specimen was heated and kept at nine different temperature points, ranging from 100 °C to 300 °C with a 20 °C interval. The infrared emission was recorded by FLIR a6701sc infrared camera at 4.08 ms shutter time and F/2.5 stop, and the obtained infrared counts were analyzed together with hot stage temperature. As Figure 4.4(b) shows, we could successfully capture the relationship between infrared counts and temperature using Planck's law, which is described below:

$$I(T) = C_1 \frac{2hc^2}{\lambda^5} \frac{1}{e^{C_2(hc/\lambda k_B T - 1}} + bkg \tag{4.1}$$

where h is Planck's constant; c is the speed of light; k_B is the Boltzmann constant; λ is the wavelength of the infrared light, which is 4 μm for our camera; I(T) is the infrared intensity, represented as photon count here; T is the specimen temperature. Using MATLAB's curve fitting toolbox, C_1 is fitted to be 3.04E-5, C_2 is fitted to be 0.895, bkg is fitted to be 869.8, with R^2 equals to 0.9999.

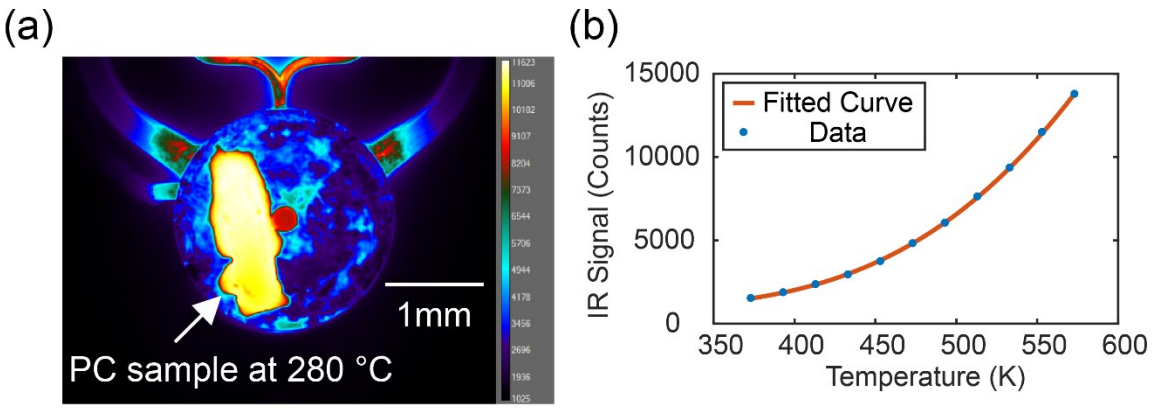

Figure 4.4: Calibration of PC's infrared emission. (a) Pseudo-color infrared image of PC sample on hot stage; (b) Curve fitting of the infrared signal using Plank's law.

Next, considering the IR signal is a combination of material emitted photons and the build plate reflected photons, additional subtraction needs to be done [90]. To eliminate the reflected signals, we measured the reflection by imaging the pass of hot and cold extruder without extruding materials, from which we could see there are reflections in the hot pass while no reflection in the cold pass (Figure 4.5). Subtracting the two signals will give the reflected photon counts, which could be used to eliminate the reflections in measurements.

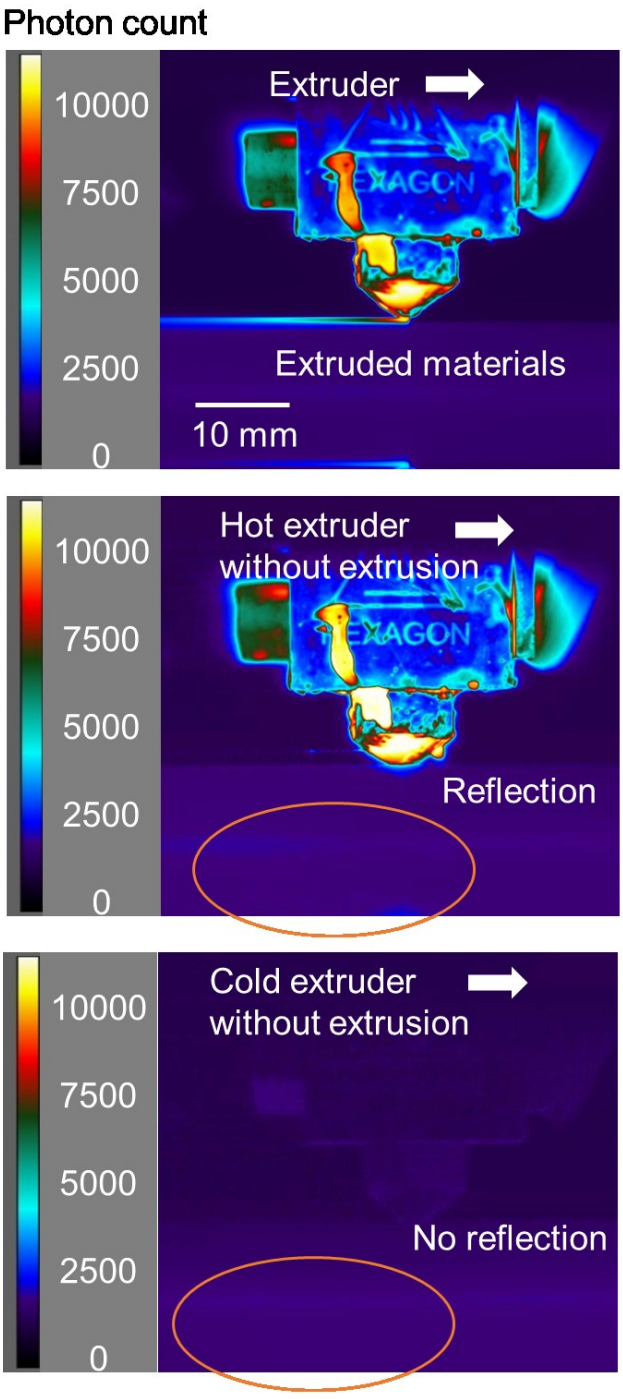

Figure 4.5: From top to bottom, pseudo-color infrared images of extrusion, hot extruder without extrusion, cold extruder without extrusion. Methods adapted from [90].

The same set of infrared camera settings and calibrations were then applied in the measurement of the thermal gradients of specimens during printing. Later, the measured photon counts at regions of interest were imported into MATLAB for converting to the temperature field and performing further analysis. During printing, we found the extruded material temperature could be 15 °C lower than the nozzle temperature set at 280 °C. However, IR thermography could not measure the material temperature when it's inside the nozzle, and the material cools down fast after leaving the nozzle. Thus, the real material temperature shall be between 265 °C and 280 °C.

Then after printing, pictures of the specimens were taken using a Canon EOS 80d DSLR with a 100 mm F/2.8 USM macro lens mounted on Manfrotto 190XPRO3 tripod. The images have resolutions of 15 μm/pixel and were later used to quantify the warping deformation associated with the thermal gradient.

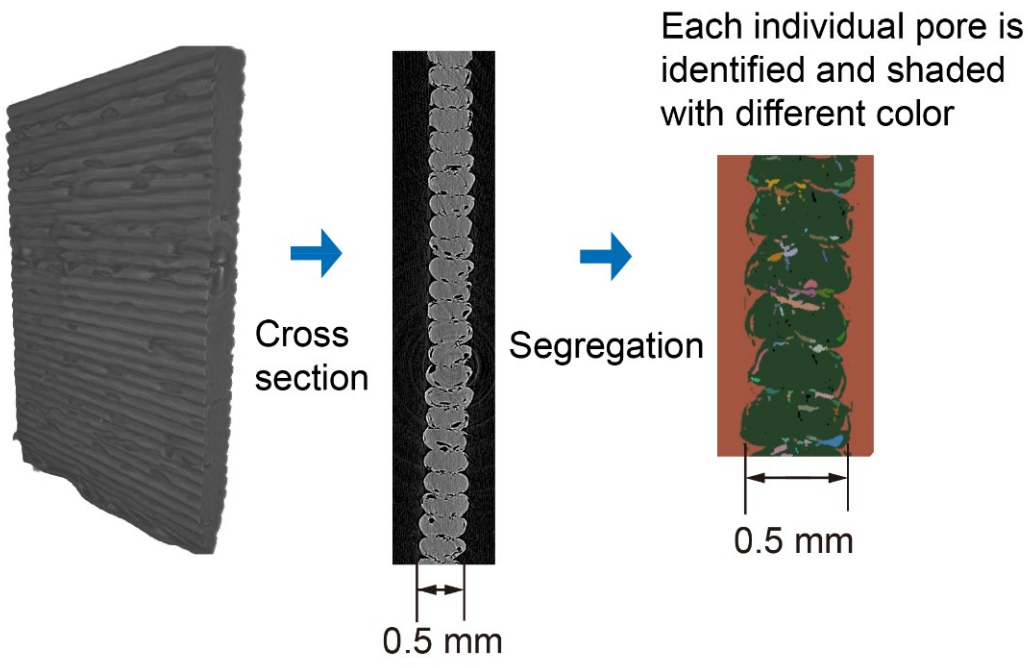

Figure 4.6: Illustration of the void segregation of scanned specimens.

Next, for humidity effect, besides the water absorption test mentioned before, the as-printed specimens were scanned by Bruker Skyscan 1172 micro-CT with 4.87 μm resolution, the calibration process has already been discussed in Chapter 2.2.1. All pores larger than 10 μm could be identified and segregated (smaller pores cannot be detected), using the post-processing software package Dragonfly. As Figure 4.6 shows, each pore was labeled separately using the Watershed transformation algorithm, and then statistics of the pore size distribution and overall porosity could be obtained.

Finally, mechanical tensile tests were performed on all specimens following the procedure described in Chapter 2.2.2.

4.3 Geometrical and Mechanical Effects of Varying Environmental Temperature and Humidity

4.3.1 Effects of varying environmental temperature

In this subsection, the relations among environmental temperature, specimen thermal gradient, warping defects, and mechanical properties were investigated and discussed. An analytical estimation of the warping deformation was also proposed and examined.

4.3.1.1 Characterization of temperature field within the specimen

Using the infrared camera, the pseudo-color thermography images of twenty specimens were plotted and labeled in Figure 4.7, representing the thermal profiles right after finishing printing under four different environmental temperatures. Within the pictures, the bottom part is the build plate, which has a constant temperature; the top part

is the far-side acrylic chamber background (out of focus), which represents the rising environmental temperature; in the middle is the specimen being printed, which has a clear layer-by-layer structure. To be noted here, the bright and dark stripes in specimens do not indicate there are quite different temperatures. They are mostly due to the differences in the surface normal: if the surface is facing the camera, the sensor could receive maximum radiations and get the correct temperature readings; otherwise at the connecting point between two layers, the surface normal is not pointing toward the lens, and the infrared emission received by the lens is smaller so that the temperature reading is lower. Due to similar reasons, we could also see the build plate has a lower temperature reading than its set value.

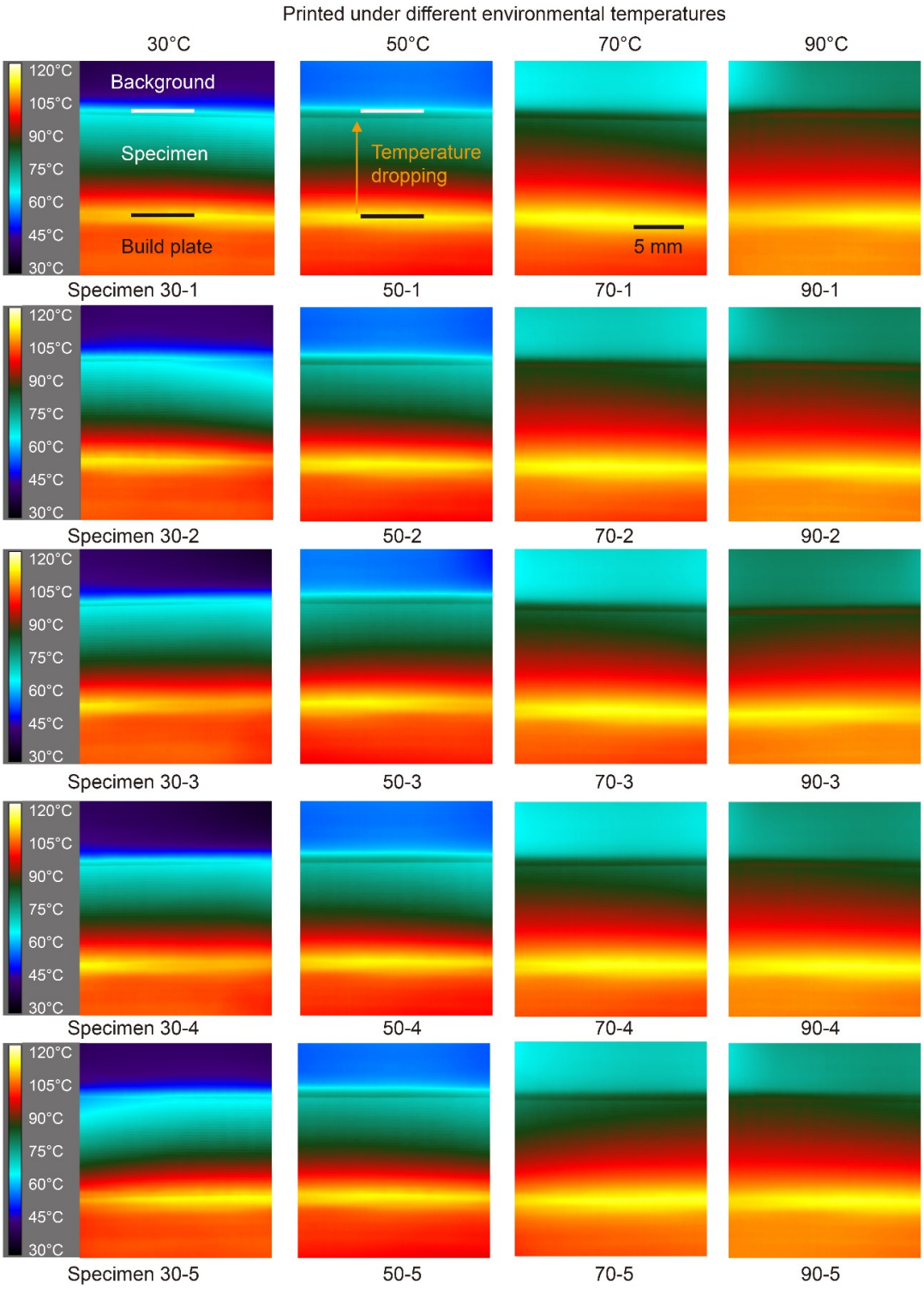

Figure 4.7: Infrared images of specimens just finished printing under four different environmental temperatures, five specimens for each.

In the images, it is obvious that the temperature dropping rate (i.e., thermal gradient) has changed significantly with the change of the environmental temperature. The numbers were quantified and plotted in Figure 4.8, from which we could see the specimen temperature decreasing with the distance from the build plate. At 30 °C, a 5.4 °C/mm thermal gradient was observed; while the thermal gradient was reduced to 2.7 °C/mm when the environmental temperature increased to 90 °C.

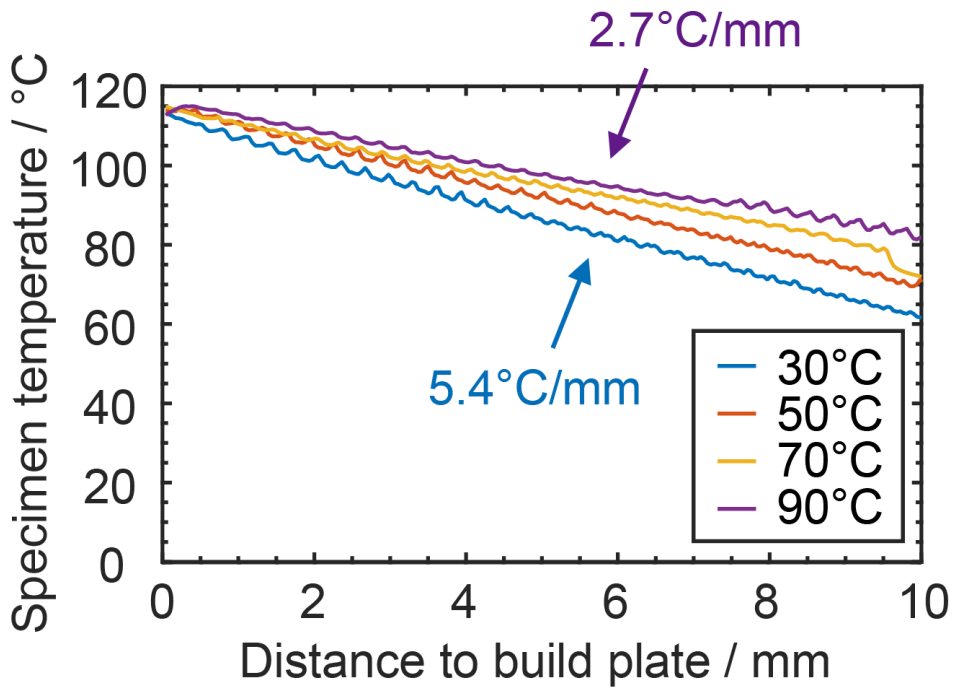

Figure 4.8: The relationship between specimen temperatures and the average thermal gradients at different heights.

4.3.1.2 Warping defect predictions and measurements

With the thermal gradient, strain mismatches were brought by the different thermal expansions in different layers, causing warping defects. From polymer theory, PC is highly

viscous before cooling down to glass transition temperature; after passing that point, any further thermal shrinkage will create corresponding thermal stress [44]. From previous literature, we could consider only elastic and plastic deformations in PC's glassy state, while the viscosity is extremely high (> 10^{21} MPa·s at room temperature) [91]. At higher and colder layers, there is a larger temperature difference between specimen temperature and glass transition temperature, so that PC shrinks more than lower and warmer layers. As a result, the entire printed specimen tends to bend upward, while the deflection could be mitigated with higher environmental temperature, which generates less thermal gradient, as Figure 4.7 shows.

Given the observed thermal gradient, it is possible to analytically predict the corresponding warpages. In our case, the maximum thermal strain is smaller than 2%, which is within the linear region of the stress-strain curve (Figure 2.3), so that no plasticity is involved. For a slender beam without external constraint, the warping-induced curvature could be estimated as:

$$\kappa = \alpha(T)\frac{(T_g - T_{top}) - (T_g - T_{bottom})}{H} = \alpha(T)\frac{dT}{dz}, \tag{4.2}$$

here α(T) is the coefficient of thermal expansion obtained from Figure 4.2, fitted at each interested temperature ranges; L is the beam length (considering the symmetry, we use 35 mm here); H is the beam height; T_g is the glass transition temperature; T_{top} and T_{bottom} are the temperatures at top and bottom of the specimen. The temperature/height term is equal to the thermal gradient along height direction, marked as dT/dz, the measured values have already been given in the Chapter 4.3.1.1.

However, since our specimen is not a slender beam, the shear deformation cannot be ignored. Hence, we applied a correction based on Timoshenko beam theory [92], [93]:

$$\kappa_T = (1 + \frac{2EI}{KL^2AG})\alpha(T)\frac{dT}{dz}, \tag{4.3}$$

where E is the elastic modulus, G is the shear modulus (E/G = 2.7 for PC), I is the second moment of area, A is the cross-section area, K is the Timoshenko shear coefficient (equals to 5/6 for a rectangular section).

As a comparison, we took pictures of the specimens printed with different environmental temperatures, shown in Figures 4.9 - 4.12 (increased contrast). The curvatures were then extracted via MATLAB processing of converting to binary figures and fitting to circles. To be noted, in real practices there are some common measures to mitigate warping defects, including gluing the specimens to the build plate and intentionally increasing the first layer's width for better bonding. Here we did not apply any of those measures, and the pictures were taken after releasing the specimens from the build plate, so that their true curvatures could be reflected.

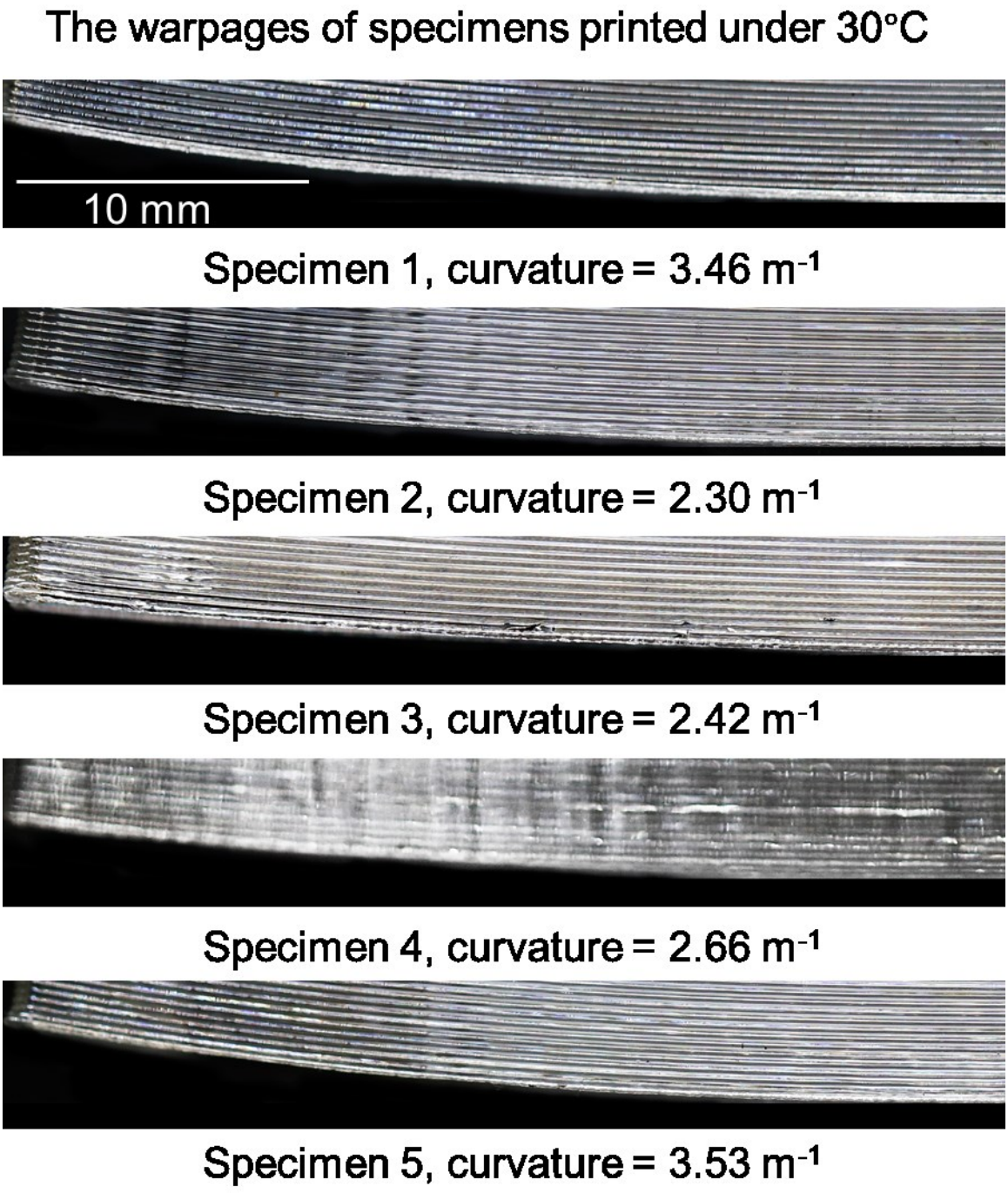

Figure 4.9: Warpages of specimens printed under 30 °C environmental temperature.

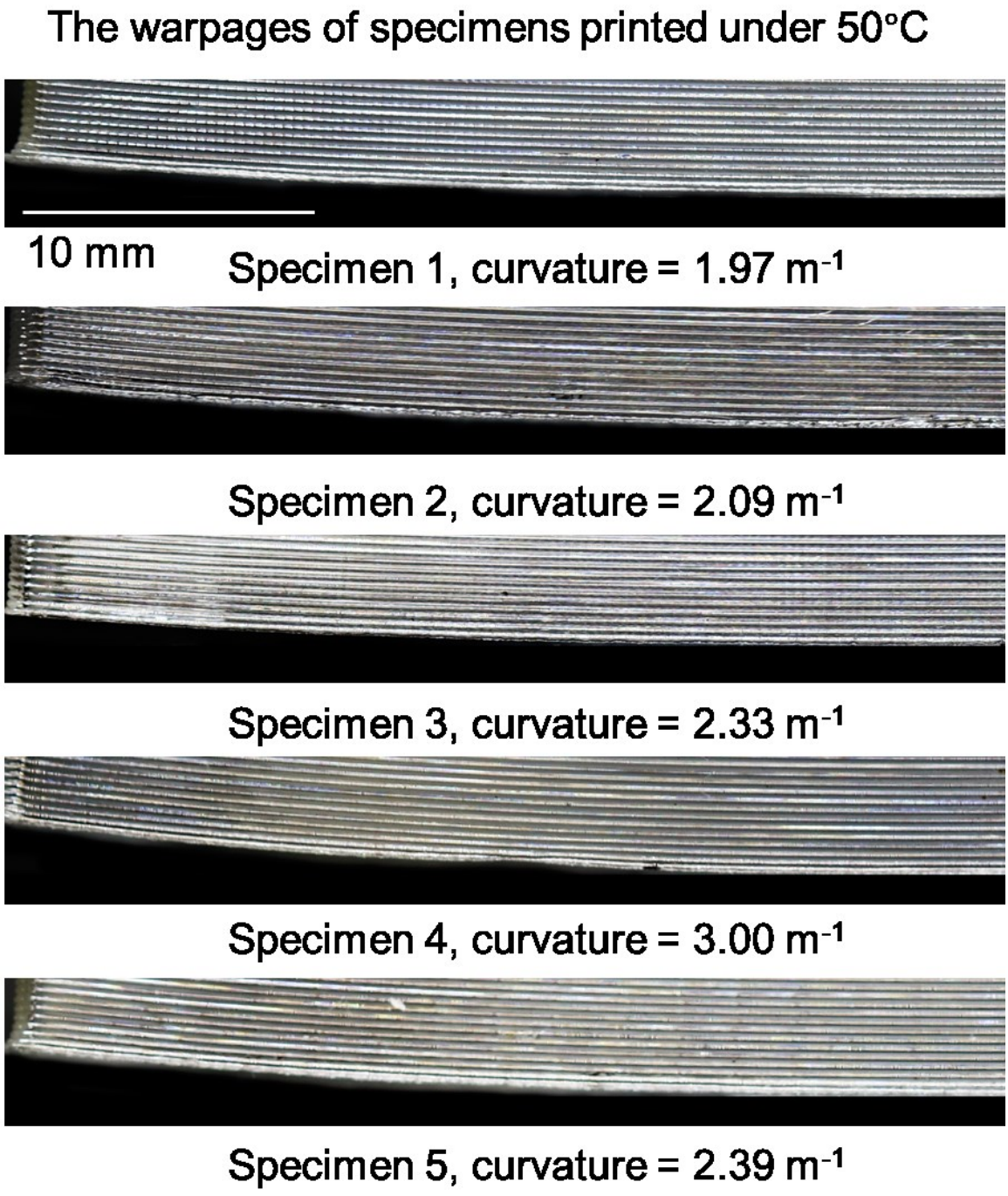

Figure 4.10: Warpages of specimens printed under 50 °C environmental temperature.

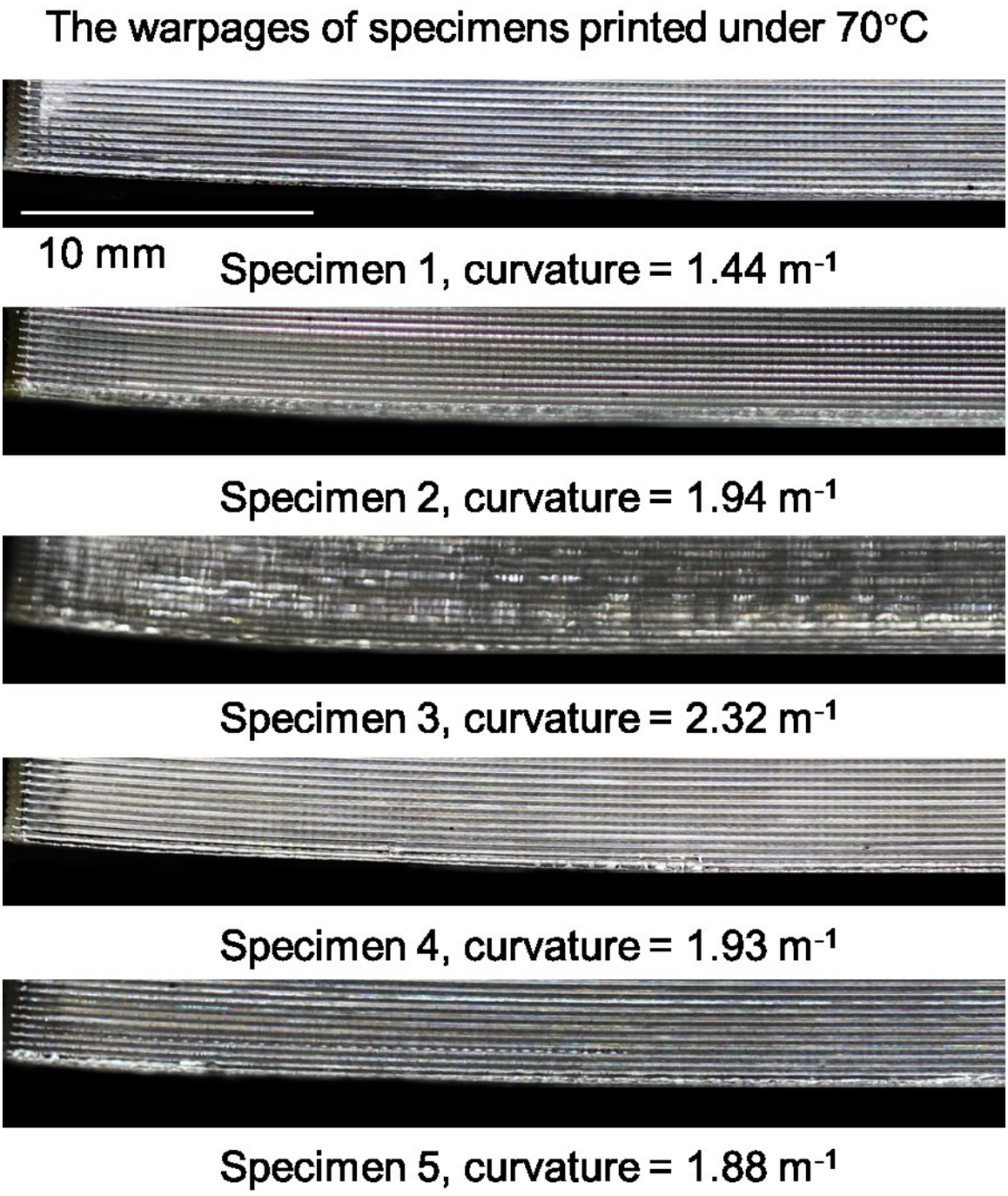

Figure 4.11: Warpages of specimens printed under 70 °C environmental temperature.

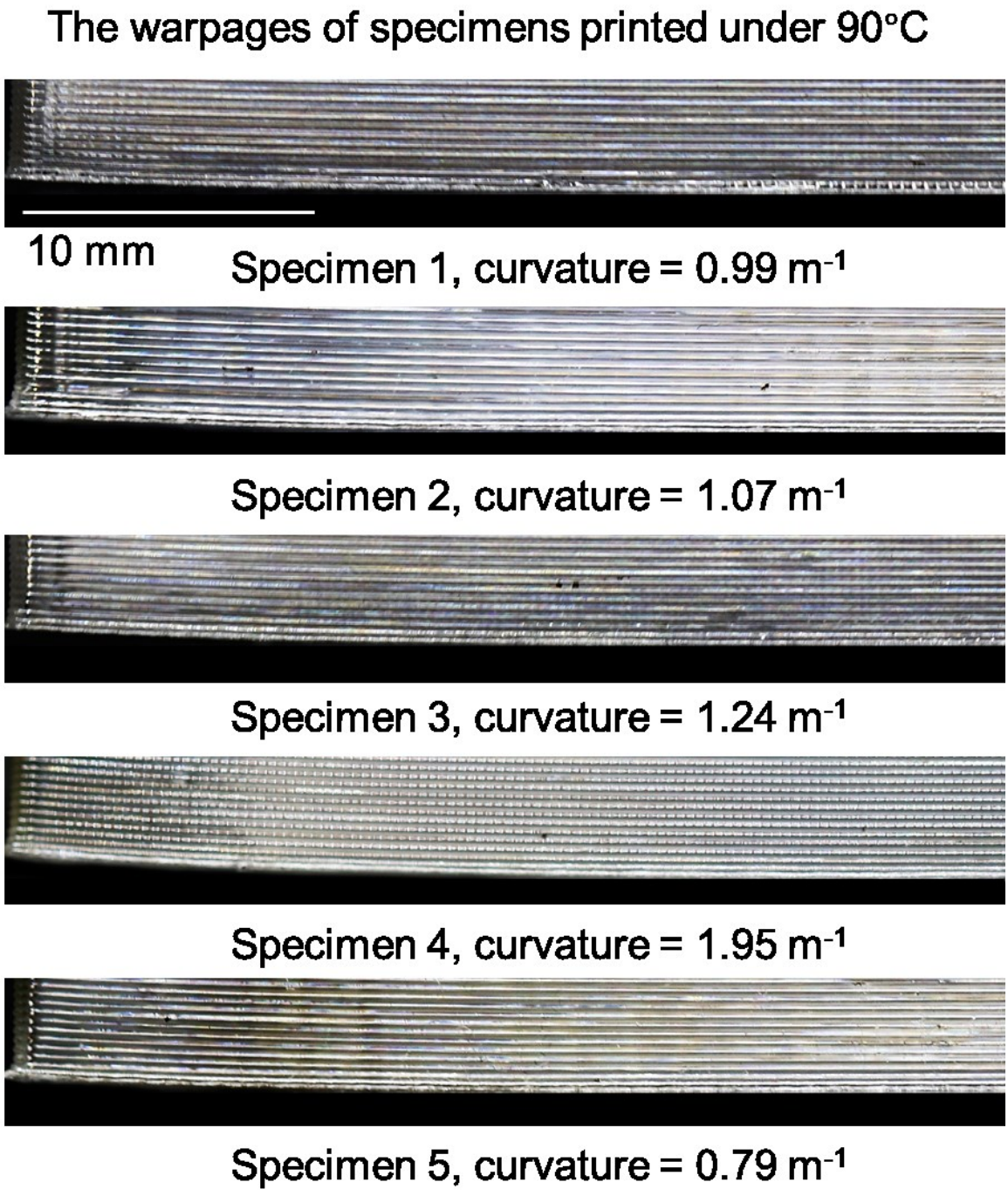

Figure 4.12: Warpages of specimens printed under 90 °C environmental temperature.

From Figure 4.13, we could see the model can capture the warping curvature change upon a different environmental temperature. The discrepancy, especially for the

overestimation at 90 °C, could be attributed to the adhesion effects. The adhesion force between the build plate and the specimen could compensate for the bending moment induced by thermal stress, especially at higher temperatures when the thermal stress is smaller. Here in experiments, we tried to minimize the adhesion effects to fulfill the 'no external constraint' condition in our model. While in practice, the adhesion force could depend on multiple factors including material pair, build plate temperature, glues, first layer geometry, etc.

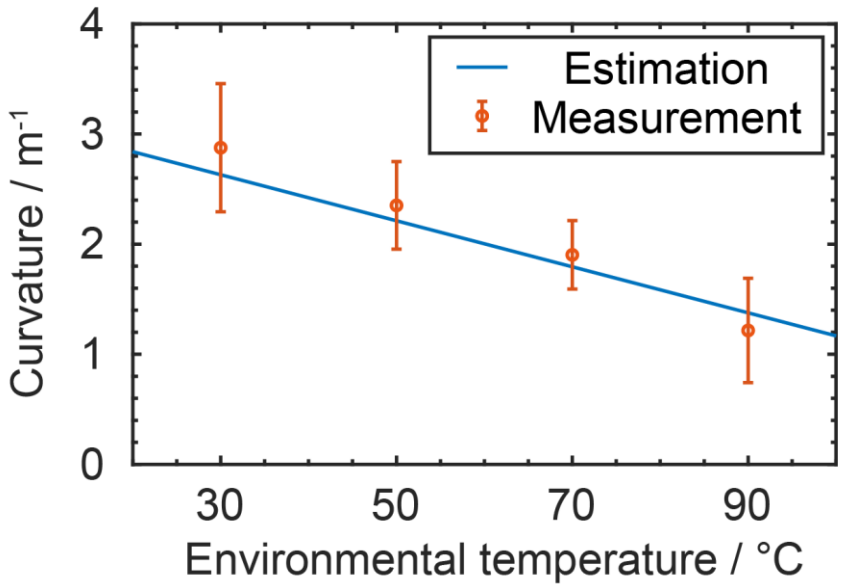

Figure 4.13: The plot of prediction and measurements of bending curvatures changing with environmental temperatures, the error bars are from standard deviations of data obtained from five measurements.

From this mechanism, there could be two ways to reduce thermal deflection. The first one is increasing the adhesion between the build plate and printed specimen. However, a concern here is the thermal stress still exists during printing. And if it is large enough, it

may overcome the bonding force between layers and cause delamination. The second option is increasing the environmental temperature, and from our observation, it could continuously mitigate the warping defects.

4.3.1.3 Impacts on mechanical properties

Finally, the mechanical strengths of printed specimens were measured in Table 4.1. For longitudinal direction (stretch along printing direction), the ductile mechanical responses are similar to those of bulk PC, as Figure 4.14(a) shows. In Figure 4.14(b), the ultimate tensile strength also shows a slightly increasing trend with increasing environmental temperature, which could be due to the mitigation of geometrical defects, including warping and delamination. With fewer warpages, the extrudates are more aligned to the testing direction, which provides higher strength. However, the strength is always smaller than that of bulk PC, indicating the mechanical performance loss brought by FFF processing.

Table 4.1: Tabulated results of tensile tests on specimens printed under different environmental temperatures.

Environmental temperature	**Longitudinal strength (MPa)**	**Transverse strength (MPa)**
30 °C	57.24 ± 2.75	19.52 ± 3.25
50 °C	59.72 ± 3.31	21.98 ± 6.38
70 °C	57.54 ± 10.54	25.95 ± 3.18
90 °C	66.53 ± 1.41	24.18 ± 3.60

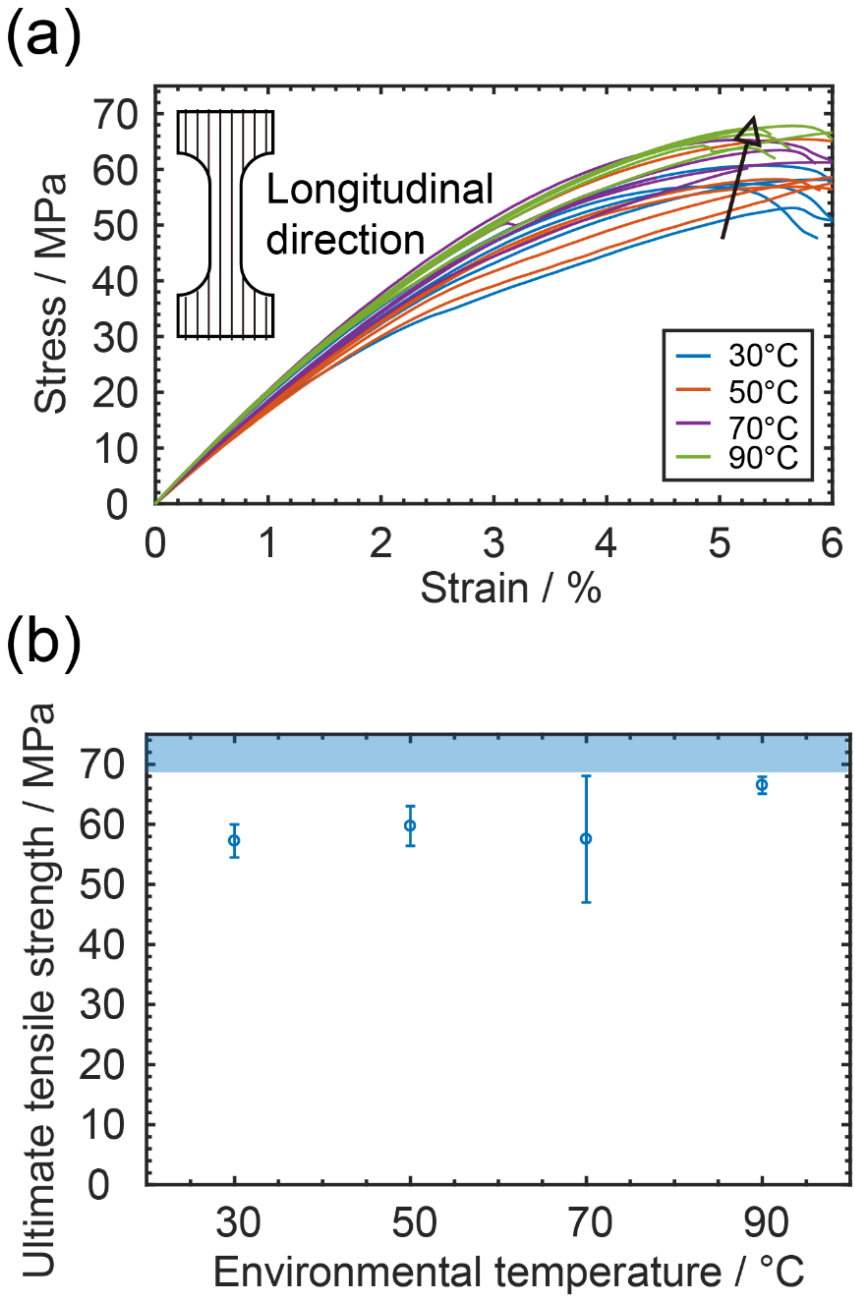

Figure 4.14: Mechanical effects of varying environmental temperatures. (a) Stress-strain curves of tensile specimens tested longitudinally, the arrow denotes the increasing strength with environmental temperature; (b) Ultimate tensile strengths of longitudinal specimens printed with different environmental temperatures, the reference value of unprinted bulk

PC is denoted as a pale blue shaded region. The error bars are from standard deviations of data obtained from five measurements.

For transverse direction (stretch perpendicular to the printing direction), the mechanical performances reduce significantly, and it showed a brittle behavior, suggesting a strong anisotropy, as Figure 4.15(a). The earlier fracture of specimens is majorly due to the non-uniform cross-section geometry in the transverse direction (illustrated in Figure 2.5); the bond between two layers is always narrower, and hence easier to break. Nevertheless, comparing different environmental temperatures, a slightly increasing trend of strength is still observed, proving the benefits of reducing thermal gradient, as Figure 4.15(b) plots.

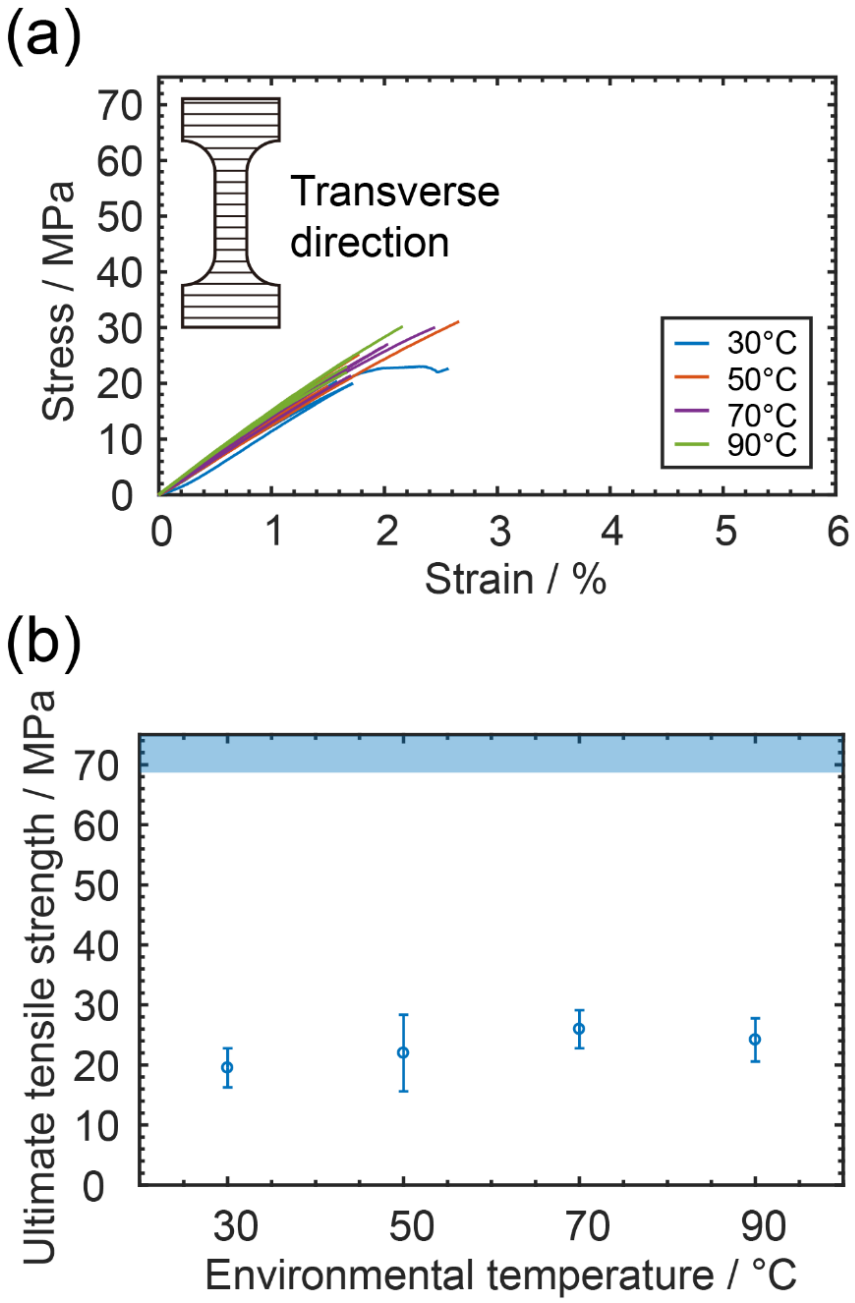

Figure 4.15: Mechanical effects of varying environmental temperatures. (a) Stress-strain curves of tensile specimens tested transversely; (b) Ultimate tensile strengths of transverse specimens printed with different environmental temperatures. The error bars are from standard deviations of data obtained from five measurements.

4.3.2 Effects of varying environmental humidity

In this subsection, the relationship among environmental humidity, specimen porosity, and mechanical properties was investigated and discussed. An analytical estimation of the porosity was also proposed and examined.

4.3.2.1 Water absorption of PC

To investigate the effects of environmental humidity, the very first task is to understand how much water the PC could absorb. As described in Chapter 4.2.1, the weight change of 20 g of dried PC filaments had been monitored for 24 h with exposure to five different humidity levels, ranging from 10 % RH to 90 % RH. After experiments, the filaments were re-dried and weighted to make sure they return to the original weight, hence the weight change is purely due to moisture absorption. The results were plotted in Figure 4.17, except for the results under 90 % RH, in which we observed significant droplet condensation and mist inside the lab balance chamber, as shown in Figure 4.16. Theoretically, condensation shall only happen after the humidity reaches 100 % RH. However, due to potential condensation nucleus (dust / sharp edges), the droplets may form earlier. As a result, those droplets could add extra weight to our specimens so that the measurement is no longer trustworthy.

Figure 4.16: Evidence of unreliable weight reading under 90 %RH due to condensation.

All four curves showed very high water absorption rate at the beginning, and the rate gradually dropped with time, until it reached equilibrium. The measured saturation points were around 0.01 wt%, 0.05 wt%, 0.10 wt%, and 0.15 wt%, respectively. The results are comparable with previously reported data [48]. When those filaments are printed, the water stored inside evaporates by the heat and creates undesired pores within specimens. To be noted here, understanding the process of printing non-saturated filaments could be very complicated. According to previous literature, the water diffusion depth in cylindrical filaments is proportional to the square root of time multiplied by diffusivity [94]. Thus, the interior core and exterior surface of the filaments may have different water contents and result in different porosities and mechanical properties.

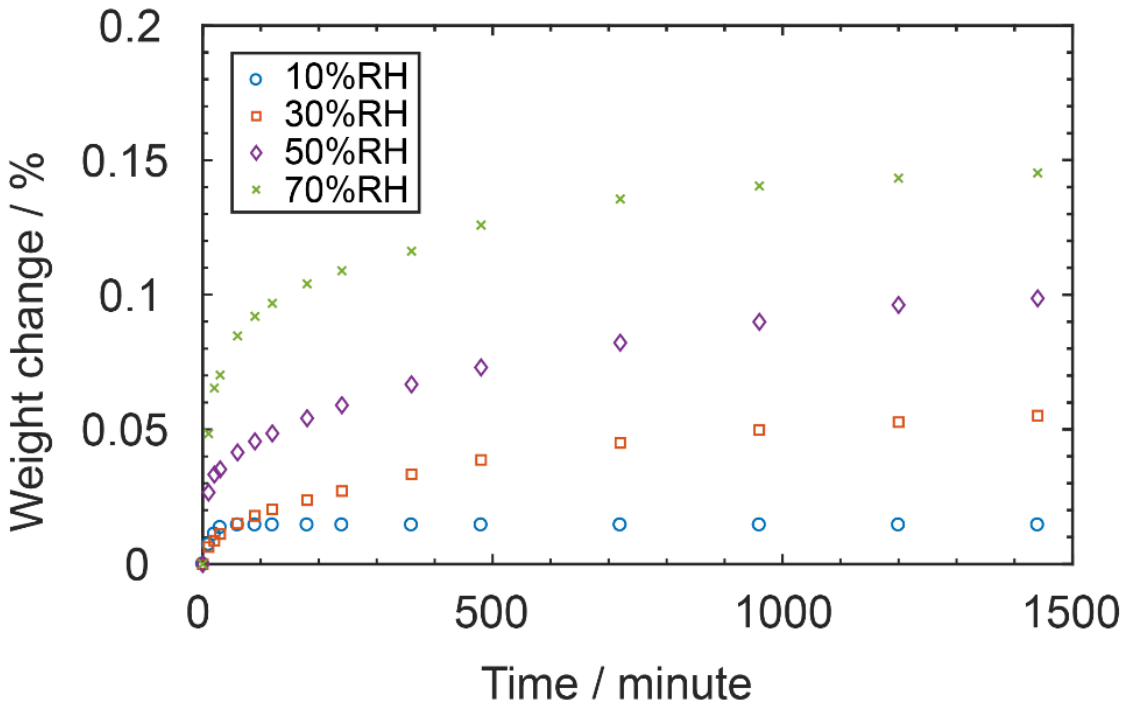

Figure 4.17: The weight change over time of PC filaments exposed to different humidity levels, specimens saturated after 24 h.

4.3.2.2 Characterization of pore defects

Printing with the filaments that have different water contents, we obtained several specimens. To characterize their porosity defects, micro-CT scans were conducted. Four representative scanned cross-sections of the specimens are plotted in Figure 4.18. For printing with dried filament, the porosity is as low as 0.16 vol%, while for high water content filament (0.15 wt%), the printed specimen has porosity up to 11.7 vol%, and the overall geometry is highly non-uniform.

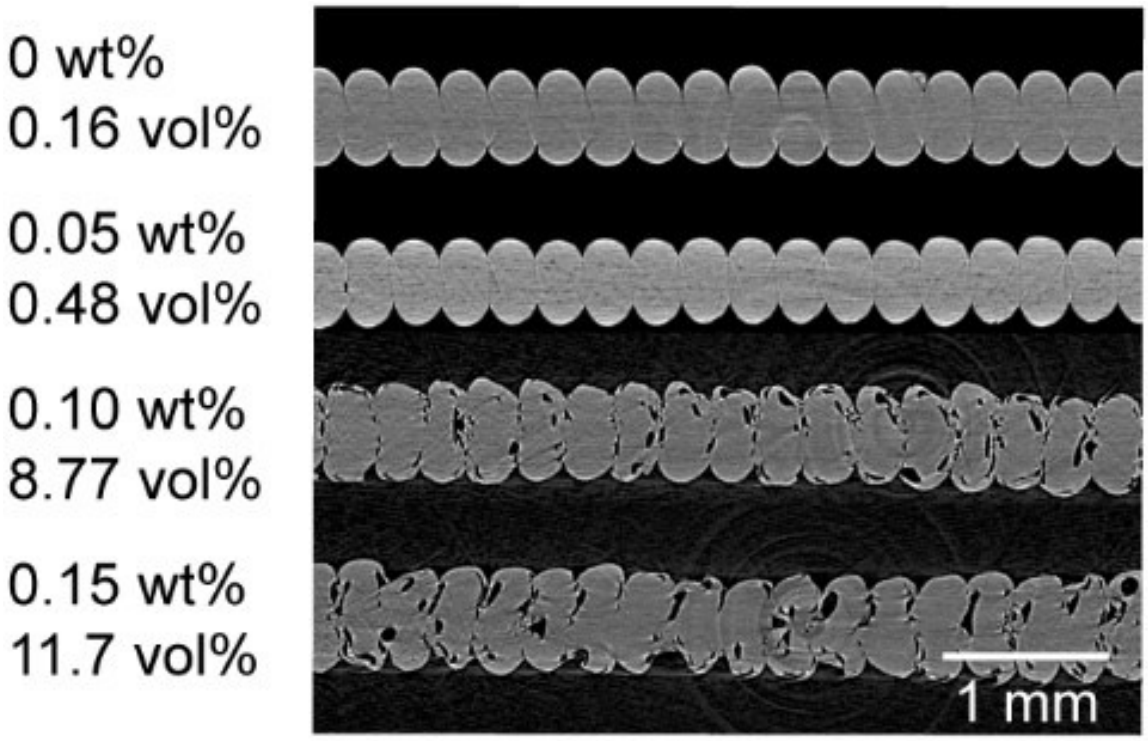

Figure 4.18: The CT-scanned cross-sections of printed specimens using filaments with different water contents.

If assuming all the water is vaporized and hence creating pores inside the specimen, we could calculate the corresponding vapor volume from mass conservation. Similar to other gases, water vapor is not an ideal gas, and corrections need to be applied to the ideal gas law [95]:

$$\frac{P}{\rho RT} = 1 + B\rho + C\rho^2 + \cdots \tag{4.4}$$

where P is the pressure inside the nozzle; ρ is the molar density, which is correlated with both vapor mass and volume; R is the gas constant of 8.314 J/(K·mol); T is the material

temperature, which in principle shall be equal to the nozzle temperature of 280 °C (553 K), but in practices it could be lower than that considering thermal conduction takes time [96]. From our IR observation, the material temperature could be 15 °C lower than nozzle temperature after coming out of the nozzle. This shall serve as the lower bound of the material temperature since IR thermography could not measure the temperature inside the nozzle, and the material cools down fast in ambient. Thus, here we made another calculation based on the temperature of 265 °C (538 K). Finally, B and C in Equation 4.4 are the virial coefficients that are characterizing the interaction potential between particles (B for two particles, C for three, etc.), which provide systematic corrections to the ideal gas law. In practice, the higher-order virial coefficients (C and beyond) are often ignored since interactions between three and more molecules are less likely to happen in the gas phase [97]. While the water vapor's second virial coefficient B has been extensively studied and could be estimated by a fitted equation [98]:

$$\frac{B(T)}{B^0} = \sum_{i=1}^{4} a_i * (T^*)^{b_i} \tag{4.5}$$

where B_0 is 1000 cm^3/mol, T^* is T/100K, a_1 is 0.34404, b_1 is -0.5, a_2 is -0.75826, b_2 is -0.8, a_3 is -24.219, b_3 is -3.35, a_4 is -3978.2, b_4 is -8.3 [98]. And the resulting B at 553K is -128.1678 cm^3/mol, while at 538K is -138.7297 cm^3/mol.

The final unknown parameter is the internal pressure, which is relatively hard to measure. A previous literature has reported an estimation approach derived from the Navier-Stokes equation [88]:

$$P_{nozzle\_approx} = \frac{12\mu qD}{h_l^3} - \frac{6\mu v_p D}{h_l^2} \tag{4.6}$$

here the Newtonian viscosity μ is 249.88 Pa·s for our PC under 280 °C and 354.83 Pa·s under 265 °C; q is the volumetric flow rate normalized by a unit length in the Y direction, which is 36.67 mm^2/s for our printing parameters; D is the nozzle diameter of 0.5 mm, v_p is the print speed of 10 mm/s, h_l is the layer height of 0.3 mm. Finally, the pressure is estimated to be 1.95 MPa at 280 °C and 2.77 MPa at 265 °C.

From Equations 4.4 - 4.6, we could calculate the water vapor's molar density (ρ) to be 450.10 mol/m^3 at 280 °C and 684.23 mol/m^3 at 265 °C. Then, the porosity could be estimated as:

$$\text{Porosity} = \text{water content} * \rho_{PC}/\rho M_{water} \tag{4.7}$$

where the density of PC is 1.22 g/cm^3, M_{water} is the molar mass of water as 18 g/mol. Substituting different water contents into Equation 4.7, we could get the estimation of the porosity. The comparison between this mass-conservation model and measured values is plotted in Figure 4.19, from which we could find the model's values are significantly higher than measured values. This could be due to two primary reasons; the first one is the water vapor may escape from the specimens, especially for water distributed near the exterior surfaces of the filaments; the second reason is the limitation of our measurement capability: our micro-CT scans ran at 4.87 μm/pixel, meaning all the pores smaller than that were not detected, while they could contribute to the overall porosity.

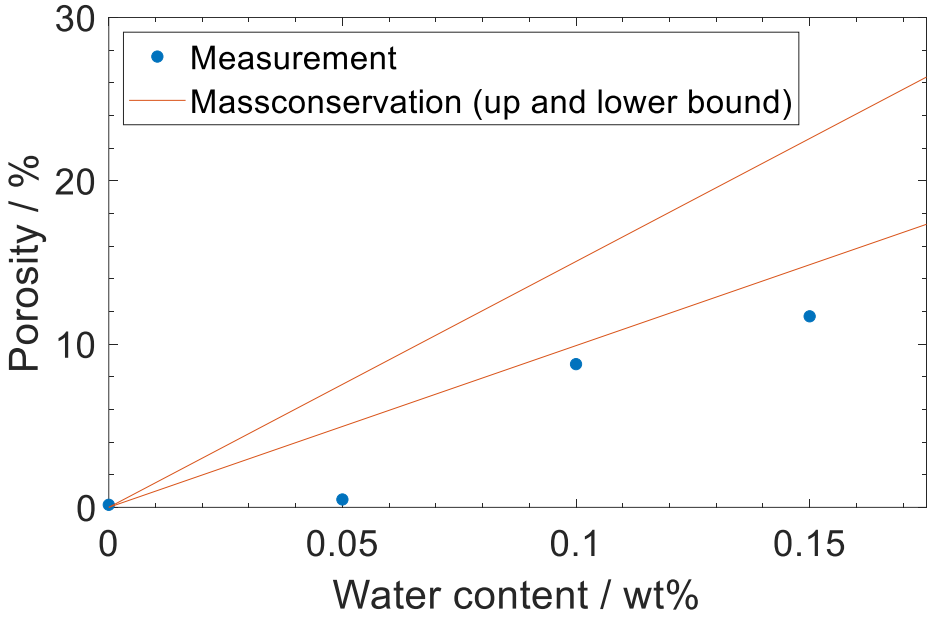

Figure 4.19: The comparison between measured porosity and predicted porosity using mass conservation.

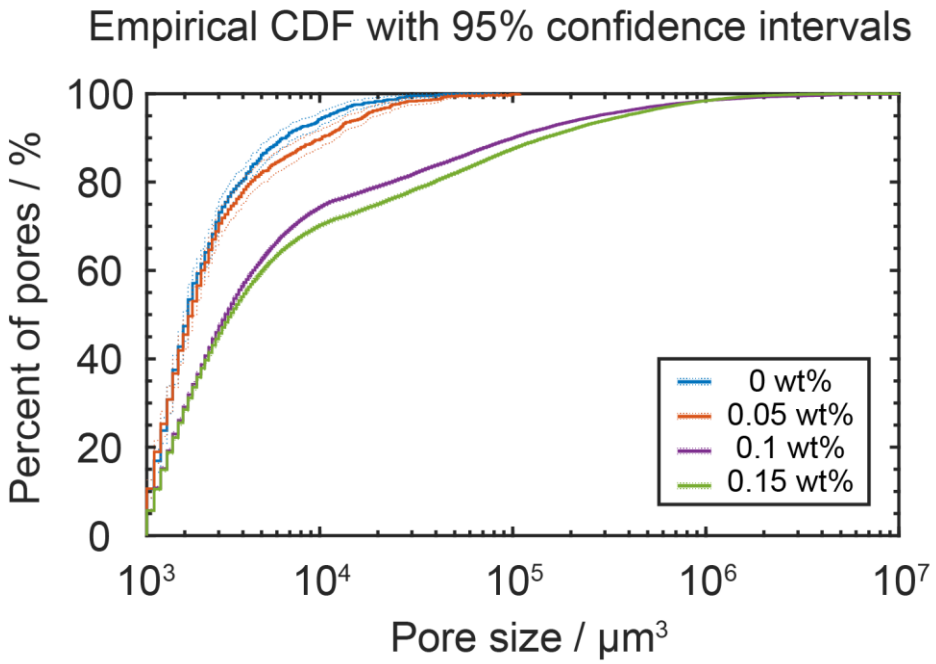

Figure 4.20: Empirical Cumulative Distribution Functions (CDF) for the pore sizes of printed specimens using filaments with different water contents, dotted lines indicate the upper and lower bounds of 95% confidence intervals.

To further quantify the size of those pores, the Dragonfly software package was used to segregate each pore and statistically analyze the pore size distribution. The results are shown in Figure 4.20, which illustrates the empirical Cumulative Distribution Function (CDF) [99] for the pore sizes. We could find that higher water contents lead to higher percentages of large pores. And, the absolute volume of the largest pores also increases with water contents. As a result, according to fracture mechanics, samples with the larger pores shall have lower mechanical strengths as the pores could easily initiate and help propagating the cracks.

4.3.2.3 Impacts on mechanical properties

Finally, we can consider the mechanical performance changes with pore defects. Previous literature has shown that the PC's mechanical properties will drop upon water absorption, which mainly due to two reasons: one is the absorbed water clusters can lead to the formation of microcracks [47], [49], [50]; the other is the molecular weight reduction upon hydrolysis [100]. For our case, the printed materials have been extruded from the hot nozzle and then kept on the 115 °C build plate for hours, so that the specimen is expected to have minimal water content after printing. This was further confirmed by additional drying experiments with the oven: the weights of the printed specimens do not change before and after drying. Though without any water content, the pore defects left inside the

specimen can still impact the mechanical properties, this shall be accounted as a geometrical factor and will be discussed below. For the hydrolysis reaction, it's a much slower process that takes months to show significant difference [100], which doesn't need to be accounted in our case.

The results are tabulated in Table 4.2. For longitudinal direction (stretch along printing direction), the mechanical behavior is still ductile, as Figure 4.21(a) shows. However, there is a significant loss in ultimate tensile strength when printing with higher water content. As Figure 4.21(b) shows, the strength decreases around 30 % compared to printing with dry filament, for which the strength is close to that of a bulk PC. Such a loss could be attributed to the porosity. The randomly distributed pores reduce the effective cross-section areas as well as create stress concentrations, which greatly weaken the specimens.

Table 4.2: Tabulated results of tensile tests on specimens printed with filaments of different water contents.

Filament water content	**Longitudinal strength (MPa)**	**Transverse strength (MPa)**	**Transverse fracture strain (%)**
0 wt%	64.95 ± 3.61	30.23 ± 4.35	2.03 ± 0.23
0.05 wt%	65.86 ± 3.14	9.34 ± 2.20	0.70 ± 0.26
0.10 wt%	47.78± 4.15	4.94 ± 0.81	0.81 ± 0.10
0.15 wt%	46.93 ± 1.83	8.75 ± 2.38	1.24 ± 0.28

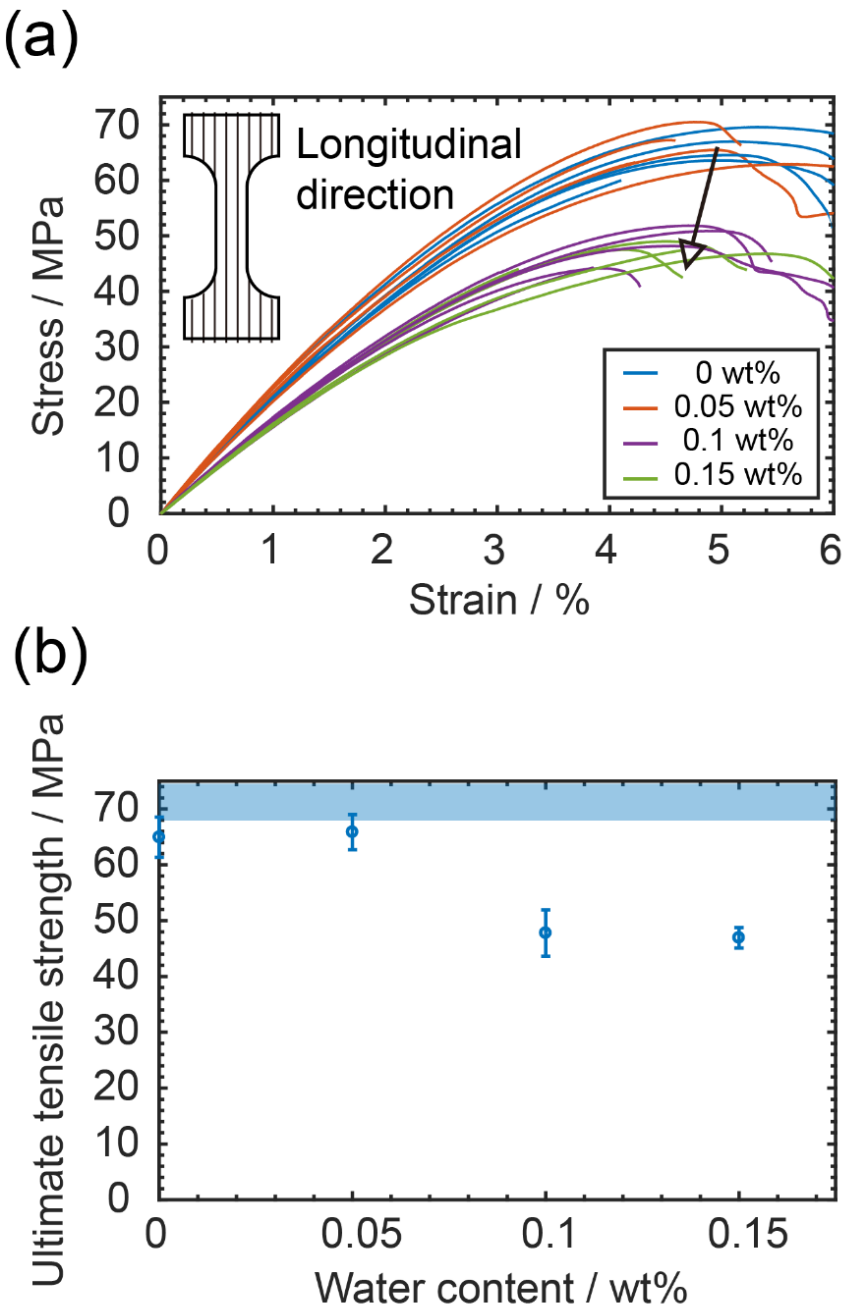

Figure 4.21: Mechanical effects of varying water content. (a) Stress-strain curves of tensile specimens tested longitudinally, the arrow denotes the decreasing strength with higher water contents; (b) Ultimate tensile strengths of longitudinal specimens printed with different water content, the reference value of unprinted bulk PC is denoted as a pale blue shaded region. The error bars are from standard deviations of data obtained from five

measurements. The reference value of unprinted bulk PC is denoted as a pale blue shaded region.

For transverse direction (elongated perpendicular to the printing direction), again the mechanical performances drop, and now the behavior becomes brittle, meaning the ultimate tensile strength is also the fracture strength, as Figure 4.22(a) shows. Here we observed a very interesting trend of mechanical property change: both fracture strength and strain firstly decrease but later increase with the increase in water content, as denoted in Figure 4.22(b). This phenomenon only happens in the transverse direction, suggesting it could be a combined effect of printed geometry and pore defects. As the illustrations in Figure 4.23 show, when there is no porosity, the weld point between two layers could initiate the crack, and the crack would propagate along the relatively narrow bond; when some porosity is introduced, the extra pores could help the crack initiation and propagation, causing lower fracture strength; however, when the porosity is high, the randomly distributed pores may deviate the crack and let it propagate along a longer path, which might introduce some extra ductility to the specimens. Evidence for this hypothesis is the pictures shown in Figure 4.23, from which we could see for no water content, the crack is exactly along the bond between two layers; while for higher water content, the crack deviates from the bond and propagates across multiple layers.

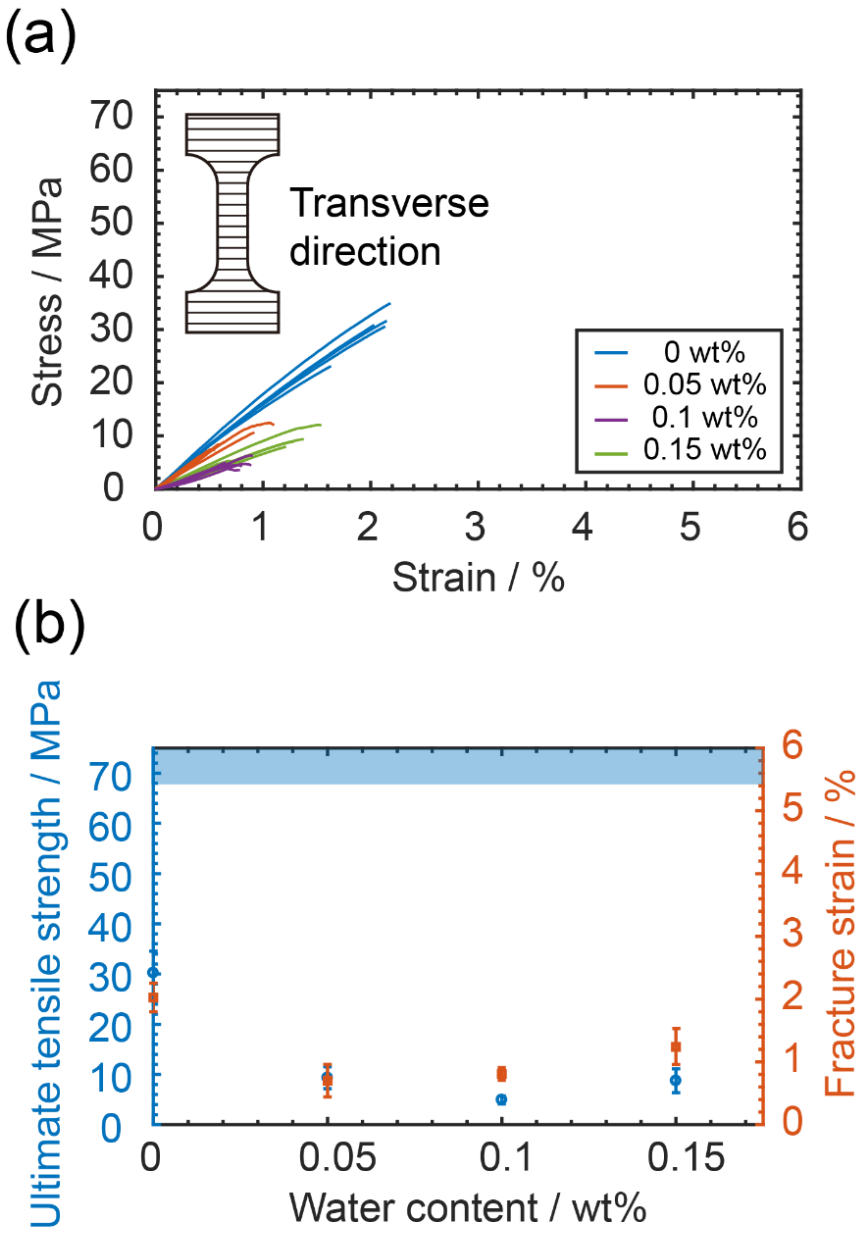

Figure 4.22: Mechanical effects of varying water content. (a) Stress-strain curves of tensile specimens tested transversely; (b) Ultimate tensile strengths and fracture strains of transverse specimens printed with different water content. The error bars are from standard deviations of data obtained from five measurements. The reference value of unprinted bulk PC is denoted as a pale blue shaded region.

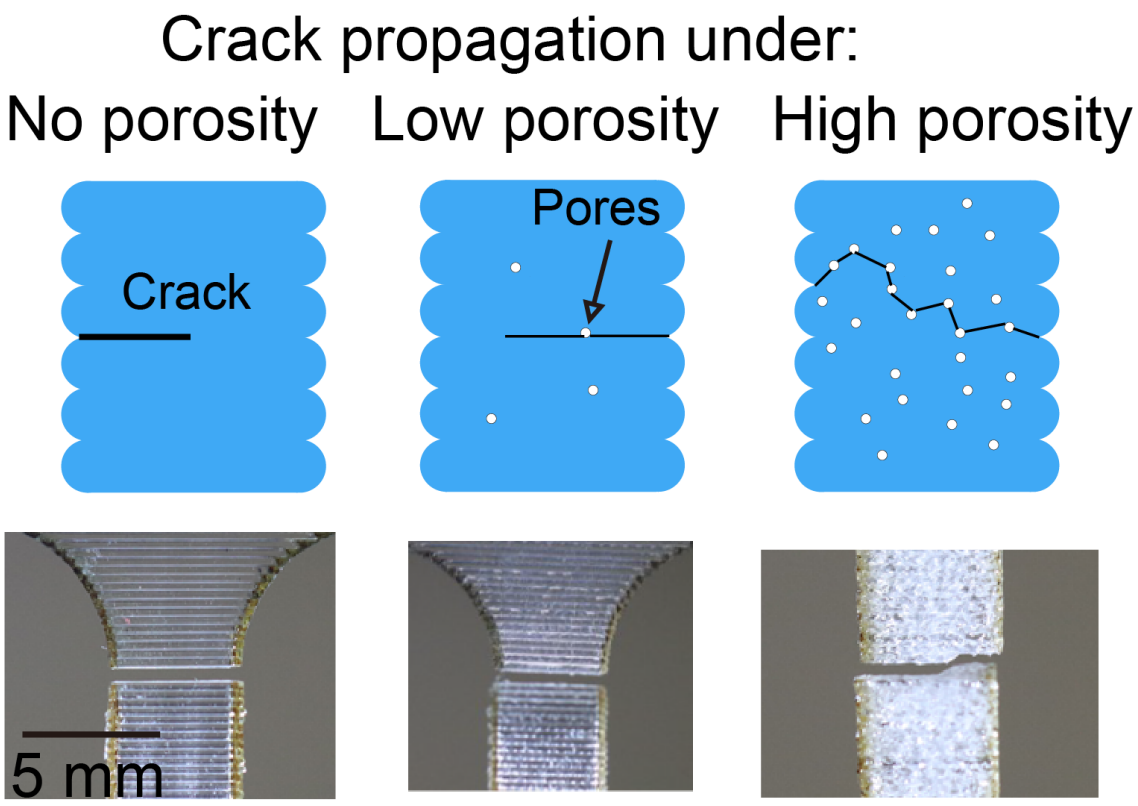

Figure 4.23: Illustrations and images of crack formations.

To further investigate the mechanism behind the extra ductility, we performed SEM scans on the fracture surfaces of porous specimens. As mentioned in Chapter 2.2.2, for non-porous transverse specimens, the crack propagates along the bonds between two adjacent layers. Similarly, for specimens printed with wet filaments, the fracture also initiates along the bonds. However, under SEM we could observe multiple pores across the surfaces, which reduce the effective cross-section areas as well as help propagating the cracks (Figures 4.24 - 4.27).

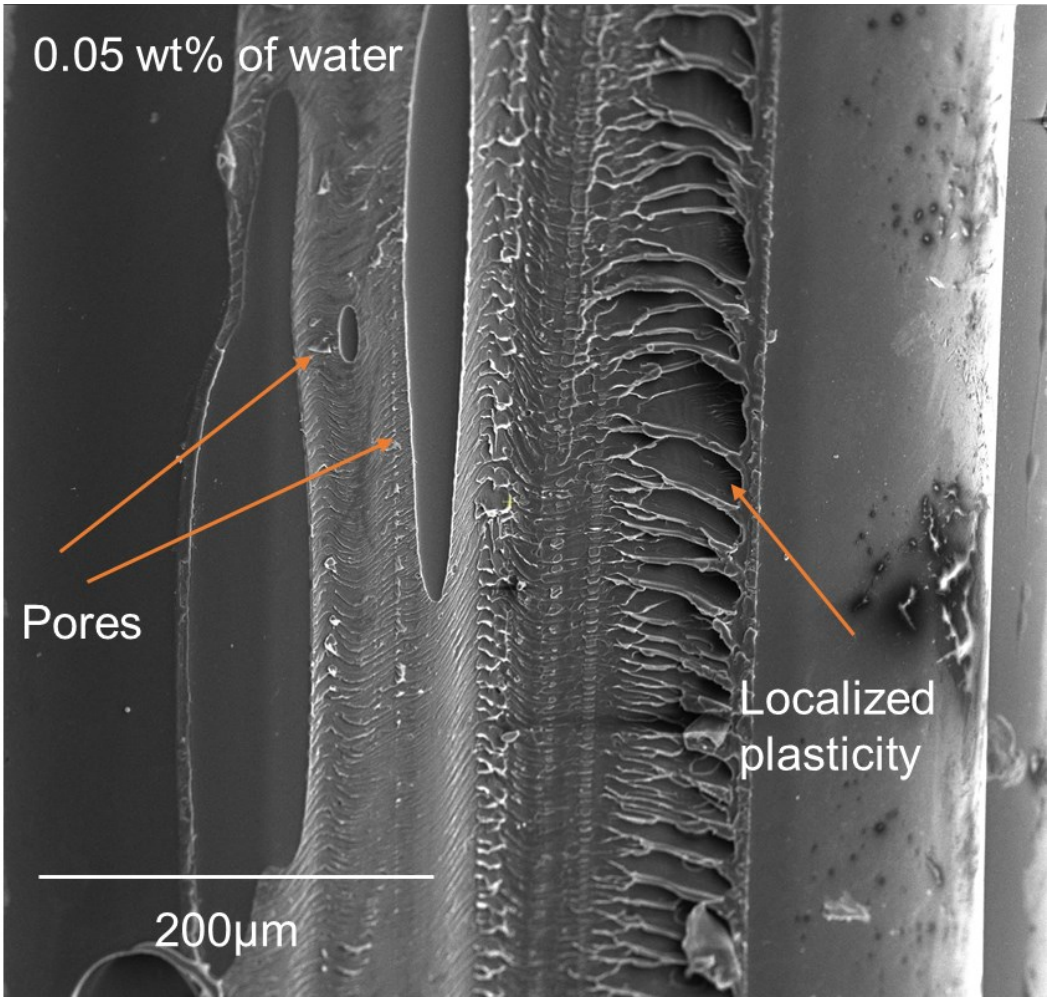

Figure 4.24: SEM image of the fracture surface of a transverse specimen printed with filaments of 0.05 wt% water content.

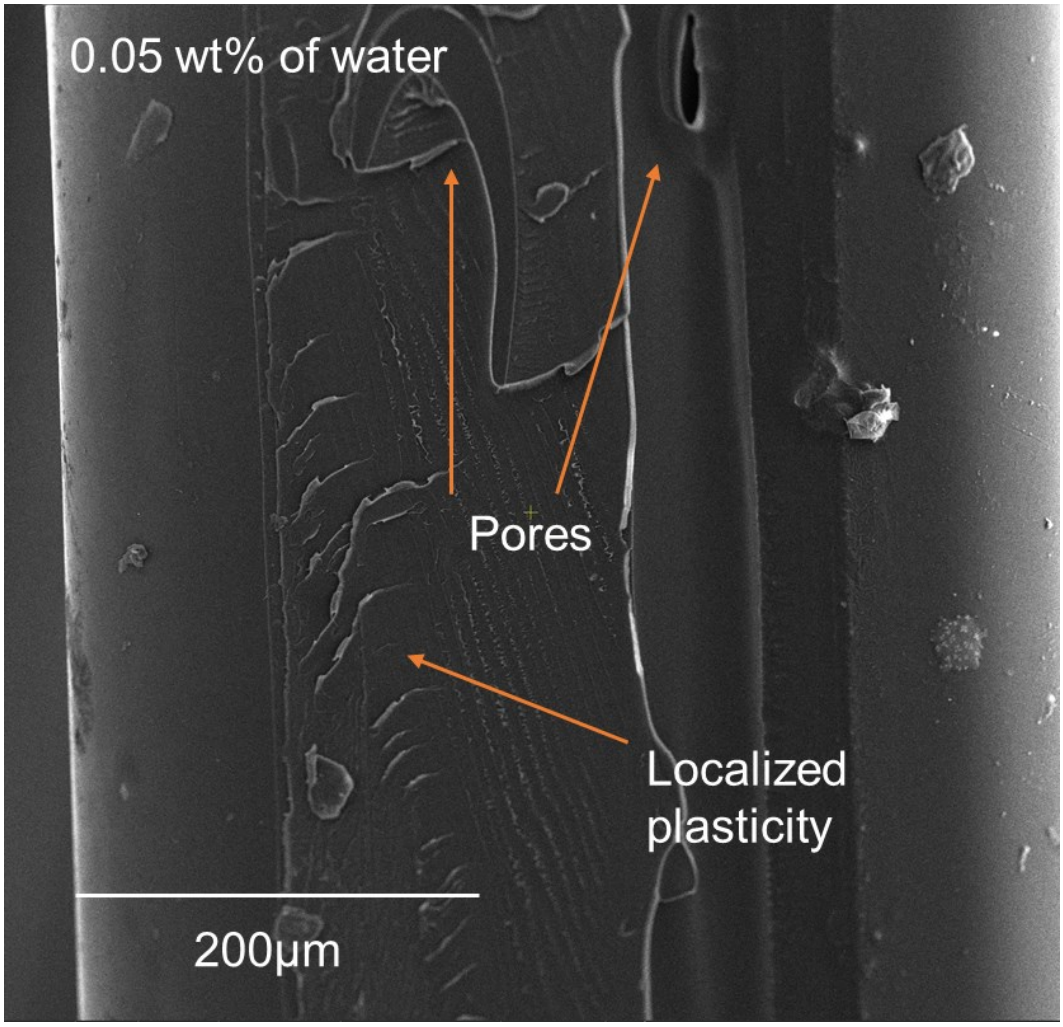

Figure 4.25: SEM image of the fracture surface of another transverse specimen printed with filaments of 0.05 wt% water content.

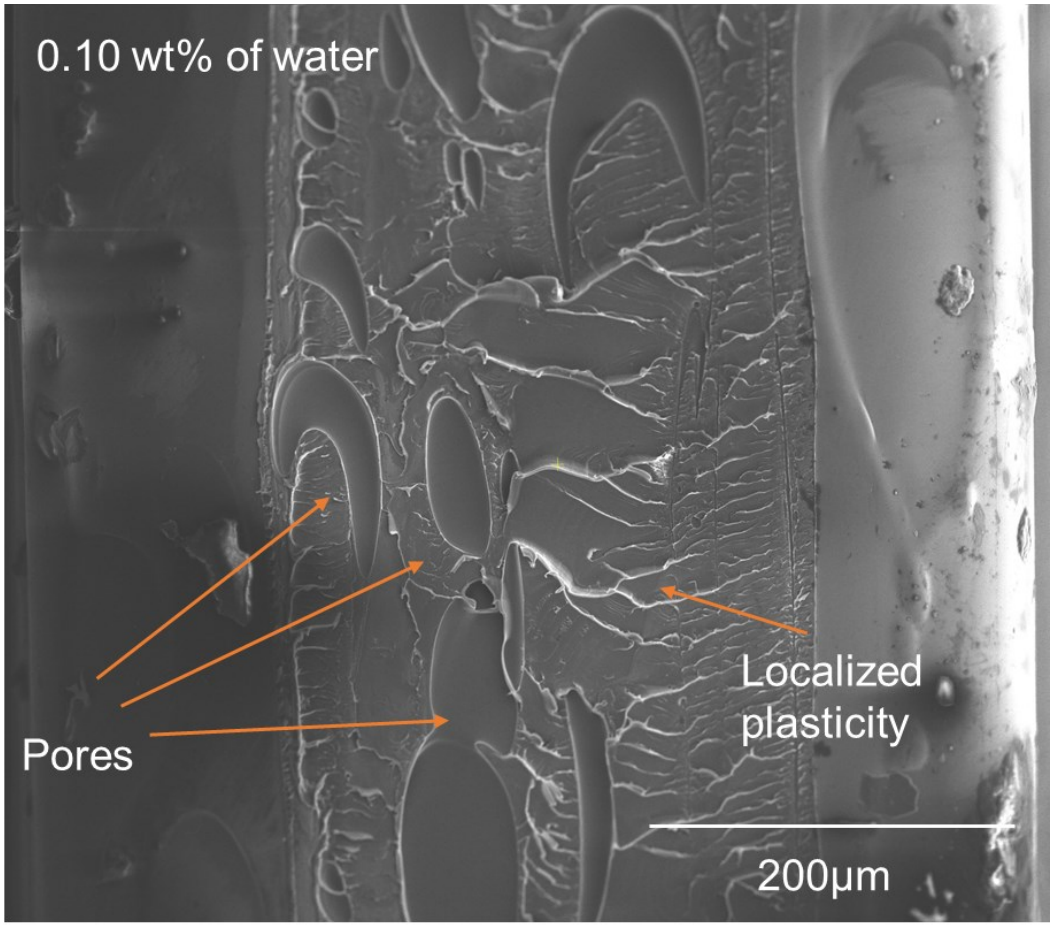

Figure 4.26: SEM image of the fracture surface of a transverse specimen printed with filaments of 0.10 wt% water content.

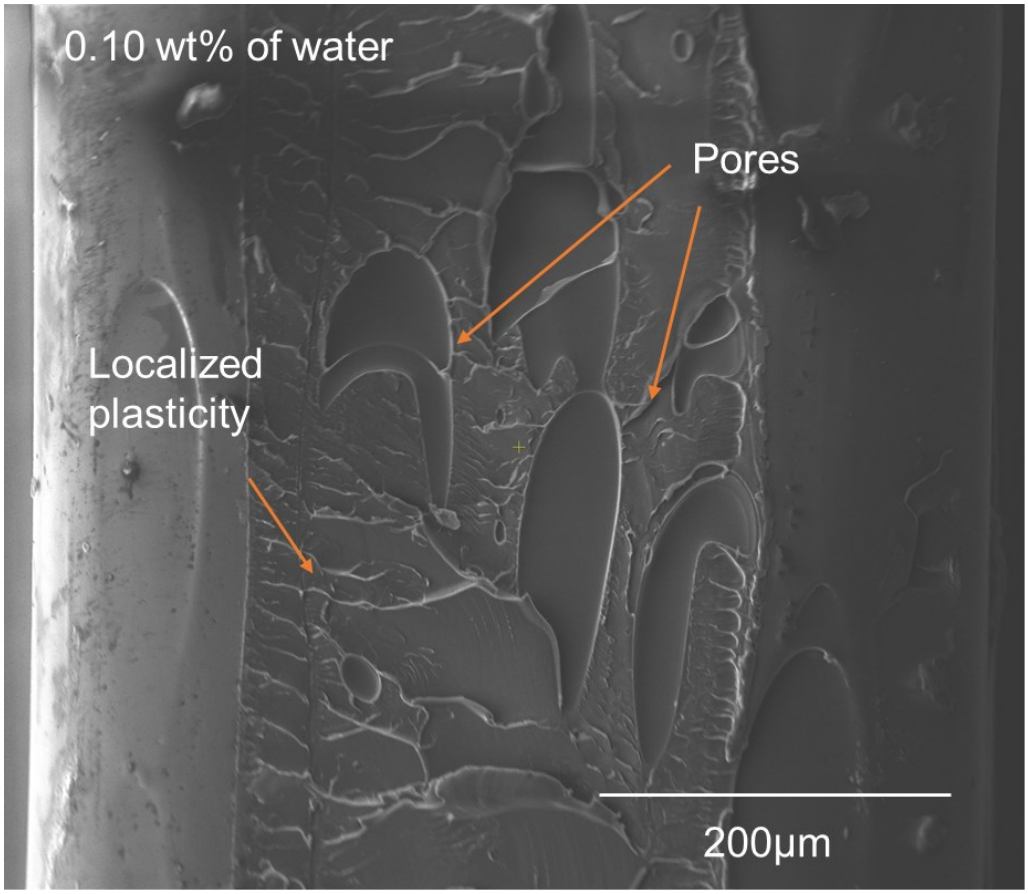

Figure 4.27: SEM image of the fracture surface of another transverse specimen printed with filaments of 0.10 wt% water content.

The specimens in Figures 4.22 and 4.23 were printed with filaments that have 0.05 wt% of water content, while the value in Figures 4.24 and 4.25 is with 0.10 wt% of water. Compared to the specimens printed with dry filaments (Figures 3.5 and 3.6), those 'wet' specimens have more pores across the surface, and in return, there are more smooth zones and fewer localized plasticity, which cause the specimen to fracture earlier and has much lower mechanical strength in the transverse direction (Table 4.2).

When the water content increases to 0.15 wt%, there are even more pores, as shown in Figures 4.28 and 4.29. However, the extra porosity deviates the crack and let it propagate

across different layers, which can elongate the crack path and increase the ductility. This could explain the extra strength and ductility observed in tensile tests.

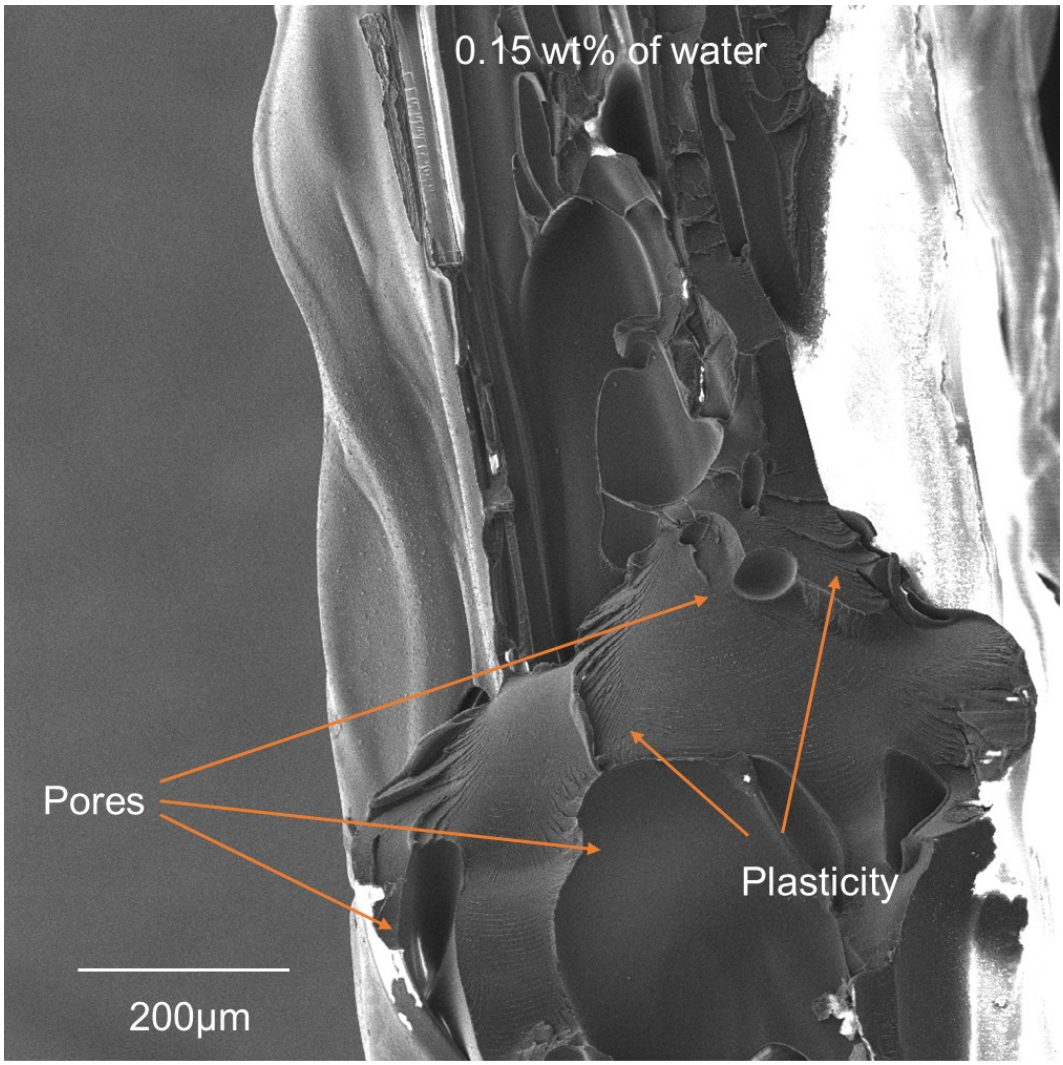

Figure 4.28: SEM image of the fracture surface of a transverse specimen printed with filaments of 0.15 wt% water content.

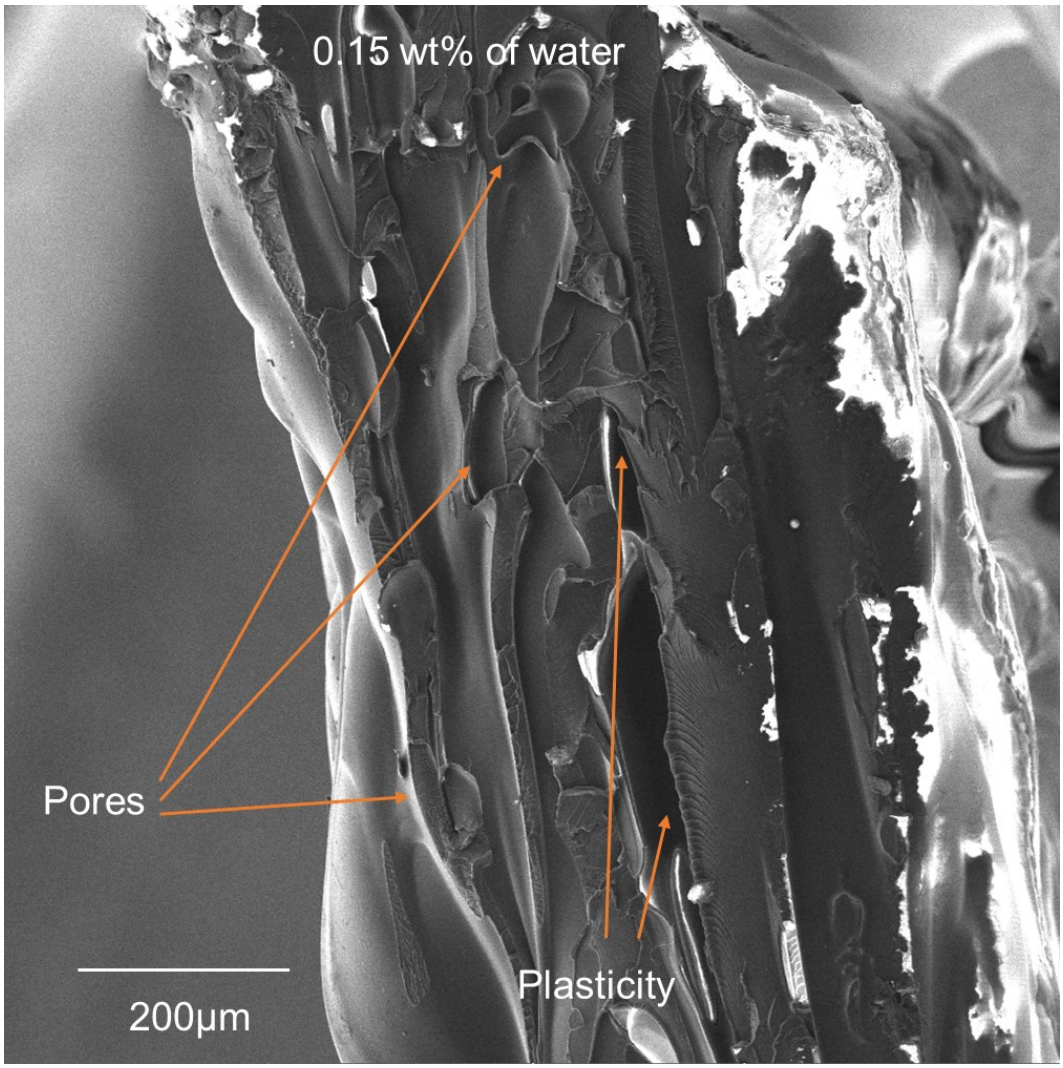

Figure 4.29: SEM image of the fracture surface of another transverse specimen printed with filaments of 0.15 wt% water content.

As a summary, the porosity brought by moisture absorption could significantly impact both the geometry and mechanical performances of printed specimens. The pores not only make the product rougher, but also decrease the uniformity of the printing pattern. For the mechanical side, the strengths will decrease in both longitudinal and transverse directions with water content. Though some extra ductility could be introduced at very high water content, the mechanical performance is still worse than that of printing with dried filaments.

Combining with the water absorption test results shown in Chapter 4.3.2.1, avoiding water content is not only about drying filaments beforehand, but also minimizing moisture absorption during printing, as the absorption rate is very fast at the beginning. For example, if less than 0.05 wt% water content is desired, printing could either be performed under 30 % RH -- as long as the printing does not take a full day. Otherwise, a dry environment is required since PC can absorb 0.05 wt% of water in less than two hours when under > 50% RH humidity.

4.4 Chapter Summary

In this chapter, we systematically investigated the geometrical and mechanical effects of varying environmental temperature and humidity during the FFF process, using a combination of analytical and experimental approaches. Regarding temperature, the temperature gradient within specimens was quantified, and the resulting warping defects were estimated and measured. The model and experiments show that increasing environmental temperature (30 °C to 90 °C) could mitigate the warping defects by a 50% reduction in curvature, as well as improve mechanical performance. Meanwhile, binding the specimen to the build plate is a worse choice (compared to increasing environmental temperature) since delamination may still happen.

Regarding humidity, the water absorption rate and saturation points of PC filaments were measured under different environmental humidity. The saturated filaments were then printed and characterized. While the water-generated porosity is less than estimated, it still showed a significant impact on the specimen's mechanical performance. Compared to printing with dried filaments, the specimens made of filaments with water content have

inferior strength in both longitudinal (up to 30 % reduction) and transverse directions (up to 70 % reduction). However, compared to specimens with low water content (> 0 wt% and < 0.10 wt%), increased ductility (up to 50 %) was observed in the transverse direction than high water content (> 0.10 wt%) specimens. This increase in ductility is due to the combined effect of high porosity and non-uniform cross-section geometry: the crack propagates beyond the bond plane, and the long path in return gives more plastic dissipation, as confirmed by SEM scans. Overall, we recommend drying filaments before printing and keep the printing environment dry, especially for long jobs, for minimal geometric warping and good mechanical performance.

Chapter 5 : Determination of the Effective Young's Modulus

In this chapter, we discussed the method to determine the effective Young's modulus for printed specimens. It is well-known that the elastic responses of homogeneous isotropic materials are commonly represented by their Young's modulus (E), but voids and geometric variability associated with additive manufacturing result in materials that are neither homogeneous nor isotropic. Here we applied finite element analysis (FEA) to determine the effective elastic modulus (E_{eff}) of polycarbonate samples printed via fused filament fabrication. The simulation could predict E_{eff} based on material intrinsic modulus and printed geometry. From further stress analysis, an analytical estimation is proposed to capture the modulus change upon varied printing conditions and hence different geometries. We envision this FEA-based approach could provide a precise modulus estimation for as-printed specimens, with the potential of applying to other extrusion-based additive manufacturing technologies.

5.1 Introduction

As stated in Chapter 1.2, though there are extensive studies working on mechanical strength, few studies have addressed the Young's modulus, an important material property used for material design and selection, of 3D-printed parts. To address this issue, the additive manufacturing community has been calling for test standards of Young's modulus that could account for the modulus change brought by the printing process [18]. If we

consider a typical tensile test procedure, the force is normalized by the cross-section area (of the standard dogbone tensile specimen) to get the stress, from which we could obtain the elastic modulus dividing by strain. Here we call this 'effective Young's modulus (E_{eff})' since it reflects the combined effects of material's intrinsic modulus (E) and printed geometry. As intrinsic modulus could change after processing, and the printed geometry has a non-uniform cross-section, the estimation of effective Young's modulus is very challenging, especially when a full cross-section geometry is not available.

Here we have investigated rational ways to predict the effective Young's modulus from measured intrinsic modulus and geometries. From micro-CT scanned digital model and measured intrinsic modulus, Finite Element Analysis was performed and shown to be able to precisely predict the effective modulus. Inspired by further studies on stress distribution, multiple analytical methods were proposed and compared with experimental results. Finally, we identified that there is one method that can provide effective Young's modulus values with less than 10 % deviations for our case. The FEA-inspired approach could be extended to other printing practices.

5.2 Methods

Figure 5.1 shows a typical geometry of extrusion-based AM specimens, where the cross-section is non-uniform and the width varies at different locations. To give an insight of the elastic response of specimens prepared by FFF, we fabricated multiple specimens, then performed mechanical tensile tests following the Chapter 2.2 procedure, and finite element method simulation based on scanned full cross-section geometry.

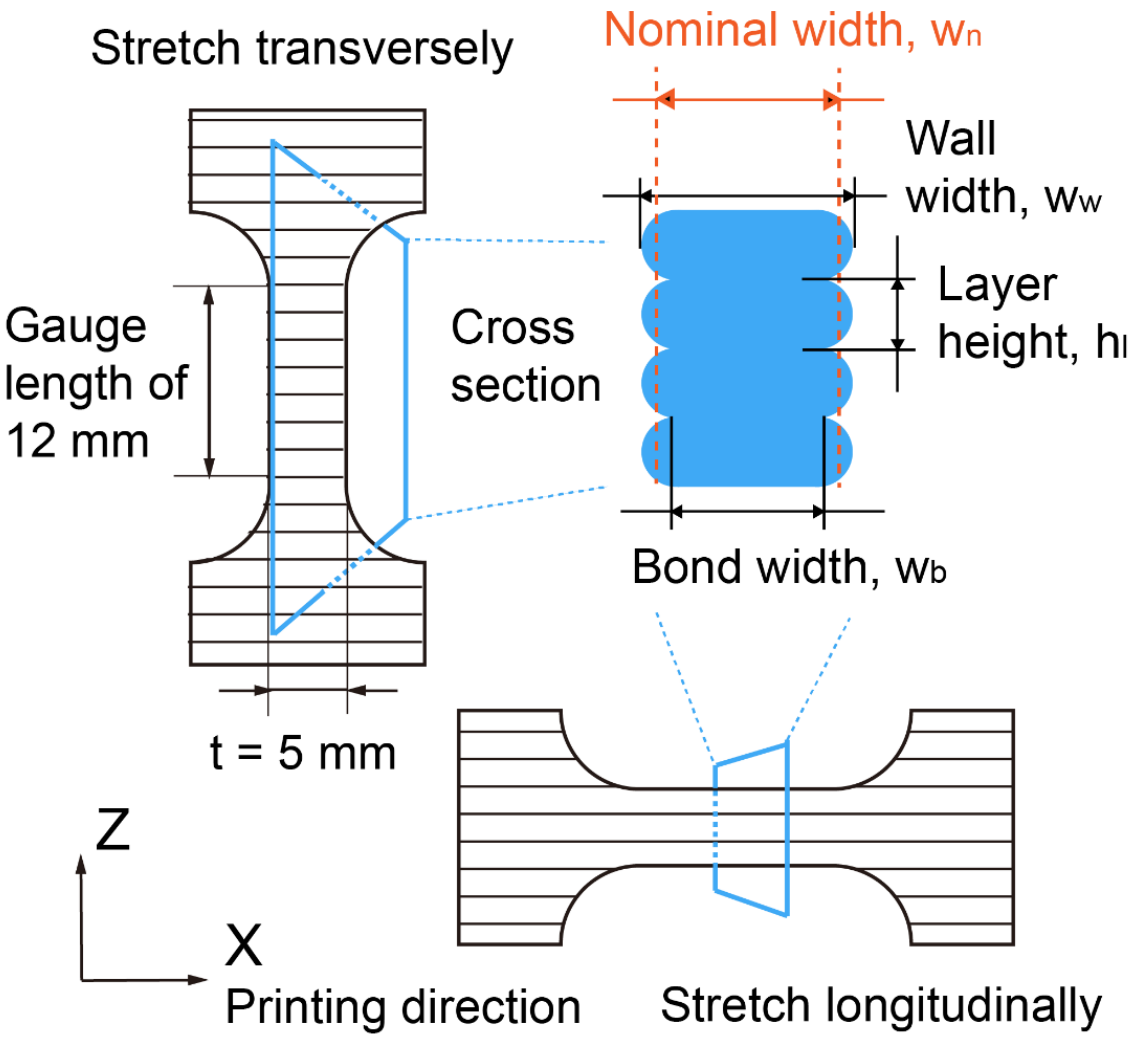

Figure 5.1: Schematics of the tensile specimens in both testing directions, one stretching along printing direction X (longitudinal), the other stretching along layer stacking direction Z (transverse).

Multiple thin-wall geometries were printed using three different layer heights: 0.15 mm, 0.30 mm, and 0.45 mm, while other parameters were kept constant (nozzle temperature: 280 °C, print speed: 10 mm/s, build plate temperature: 115 °C, humidity < 10 % RH). Each thin wall represents a stack of single extrudates: within each layer, there is only one continuous extrudate deposited. After printing, the specimens were scanned by

Bruker Skyscan 1172 Micro-CT scanner with a resolution of 4.87 μm/pixel. The scanned results were imported into MATLAB for further image analysis, which facilitated precise measurements of the width of each layer, including the narrowest part (bond width) and the widest part (wall width). As expected, the width of the original digital design (nominal width) is between bond width and wall width. To be noted here, our printing was done with 100 % flow index, i.e., the product of nozzle area and extrusion speed is equal to the product of deposited cross-section area and nozzle moving speed. This represents the most common printing setup, while intentionally increase or decrease flow index will cause over- or under-extrusion of materials and result in less dimensional accuracy.

5.3 Finite Element Analysis

To better illustrate the stress distributions within specimens and to use as references for Young's modulus measurements, simulations of the tensile tests were conducted with commercial finite element package Abaqus/Standard. As shown in Figure 5.2, a cross-section image was extracted from reconstructed 3D geometry and converted into a binary image. The outline of the specimen was further fitted and converted into vector form. The Drawing Exchange Format file was then imported to Solidworks and transformed into Abaqus-readable IGES format, before finally modeled and applied boundary conditions in the FEA using Abaqus.

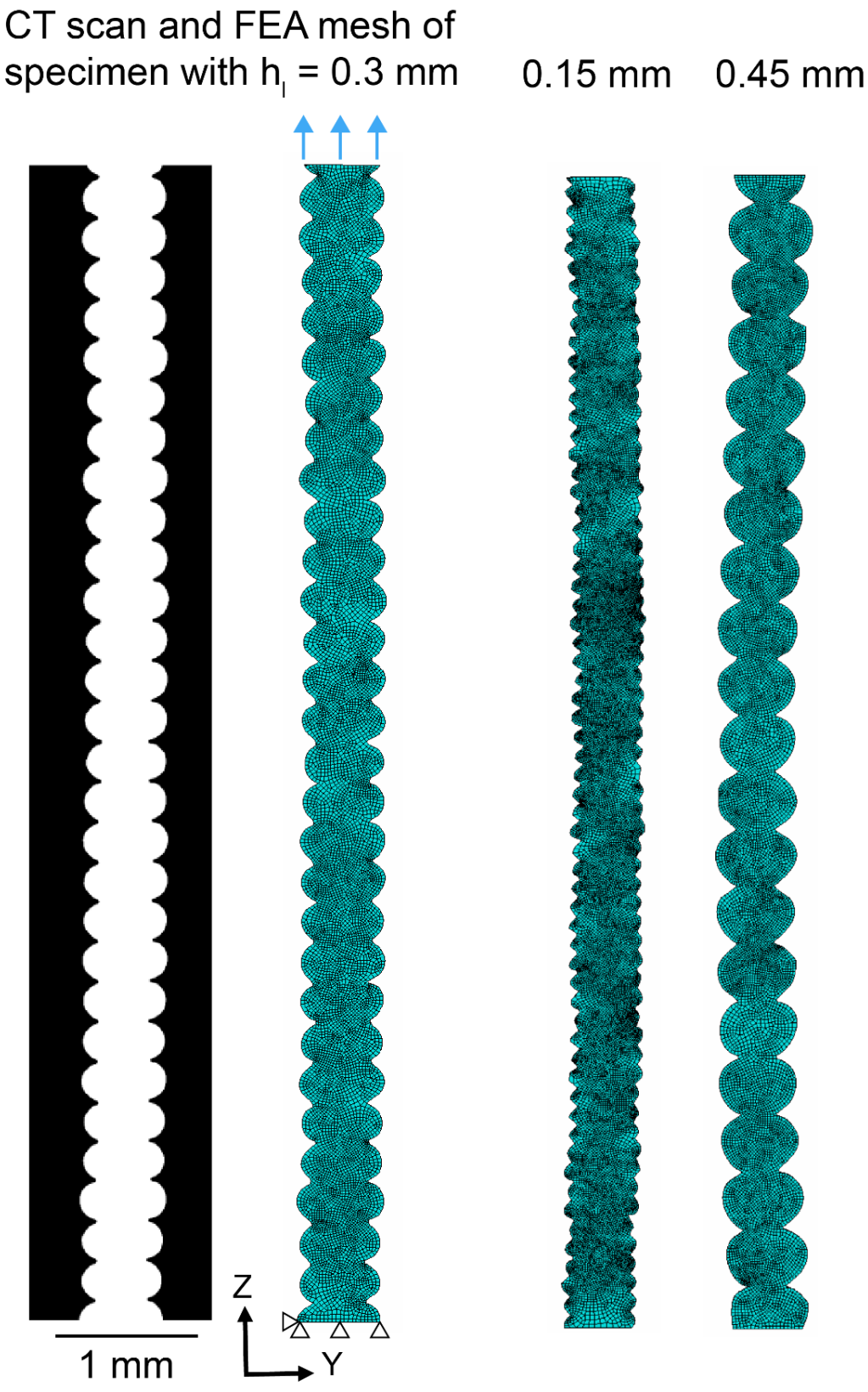

Figure 5.2: Scanned cross-section profile and converted finite element analysis setup.

The bottom surface was constrained in the stretching direction, and the bottom-left node was fixed in all directions. A small displacement loading was applied on a reference point coupled with the top surface, and all other boundaries were set as free to simulate the uniaxial tensile condition. The 8-node linear brick with hourglass control and reduced integration element (C3D8R) was used in simulations. Since we are investigating the elastic properties of tensile specimens, linear elastic material properties were applied in simulations. Considering the material intrinsic modulus may change after printing, additional measurements were performed on 0.5 mm diameter free-hang filament extruded from the printer nozzle, using the same processing parameters. The after-printing Young's modulus was measured to be 1.82 GPa ± 0.05 GPa, which was applied in simulation together with the Poisson's ratio of 0.35. After the simulations, the reaction force on the reference point was extracted, which equals to the reaction force on the right loading surface.

To validate the simulation results, a mesh convergence study was conducted. Different mesh sizes with the number of meshes ranging from 300 to 24,000 were used to estimate the error as Figure 5.3. From the figure, the results converged to less than 0.2 % error starting from 2,700 meshes, and the corresponding meshes were used in simulations (Figure 5.2). This setup could be applied to all simulations as they share very similar overall dimensions.

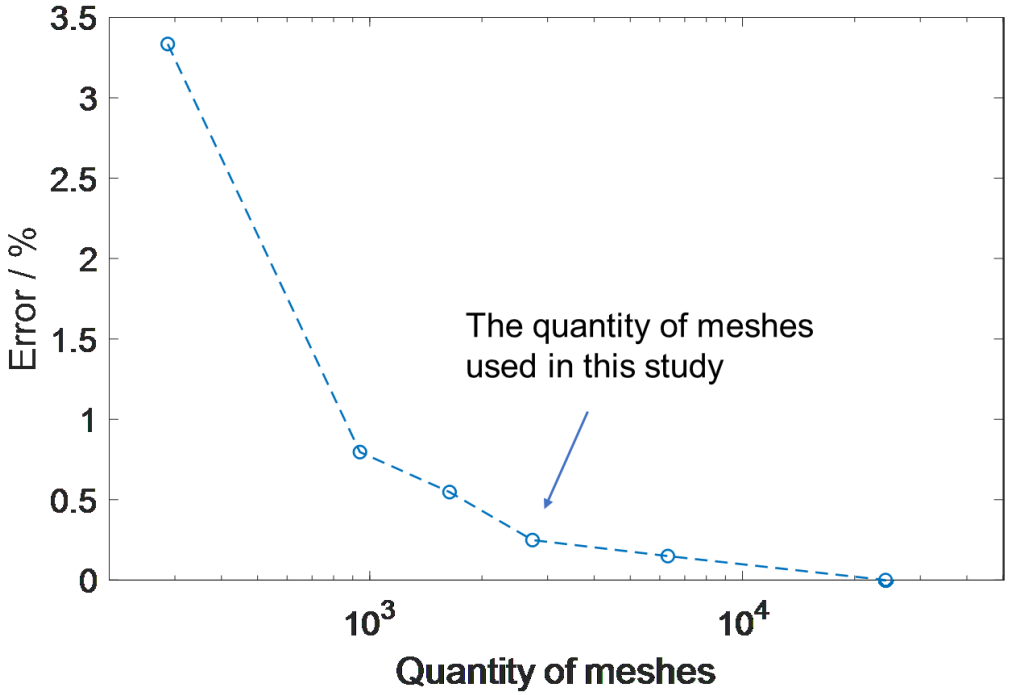

Figure 5.3: The mesh convergence study, the results converge with the increased number of meshes.

We also performed mechanical tests on printed samples following the procedure described in Chapter 2.2.2. By comparing the effective Young's modulus obtained by simulation and experiment, we do find this elastic simulation could successfully capture the specimens' moduli, as Table 5.1 and Figure 5.4 shows. This further confirms that geometry and intrinsic modulus change contribute together to the effective Young's modulus change, which could be accurately simulated by considering both factors. However, as the intrinsic modulus change is only 3 % according to our measurements (Table 2.1), geometry shall be regarded as the major cause.

Table 5.1: Comparison between measured Young's modulus in transverse tests and the corresponding predictions from the Finite Element Analysis.

Layer height	**Measured effective modulus (GPa)**	**Predicted effective modulus (GPa)**
0.15 mm	1.79 ± 0.03	1.77
0.3 mm	1.52 ± 0.06	1.59
0.45 mm	1.22 ± 0.08	1.26

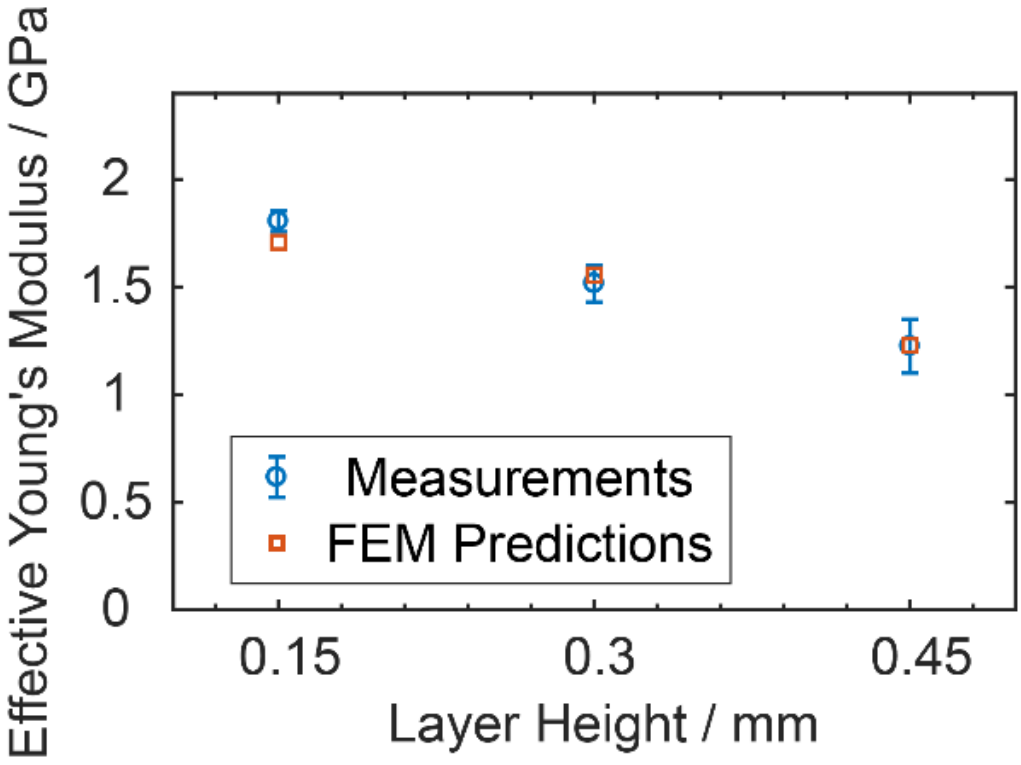

Figure 5.4: Comparison between measured Young's modulus in transverse tests and the corresponding predictions from the Finite Element Analysis. The error bars are from standard deviations of data obtained from 5 measurements.

Looking back to the simulation results, from the stress distribution within the tensile specimens (Figures 5.5 - 5.7), the stress in YY and YZ directions is more than 80 % smaller compared to that of the ZZ direction. For the normal stress along the stretching direction (ZZ), the stress within bond width is almost uniform, except few stress concentrations at linking points between two layers. Meanwhile, the stress in the ZZ direction drops significantly out of the bond width region. At the very far points in the caps, compressive stress is observed, which means the cap regions only contribute to a small portion of the overall mechanical performance.

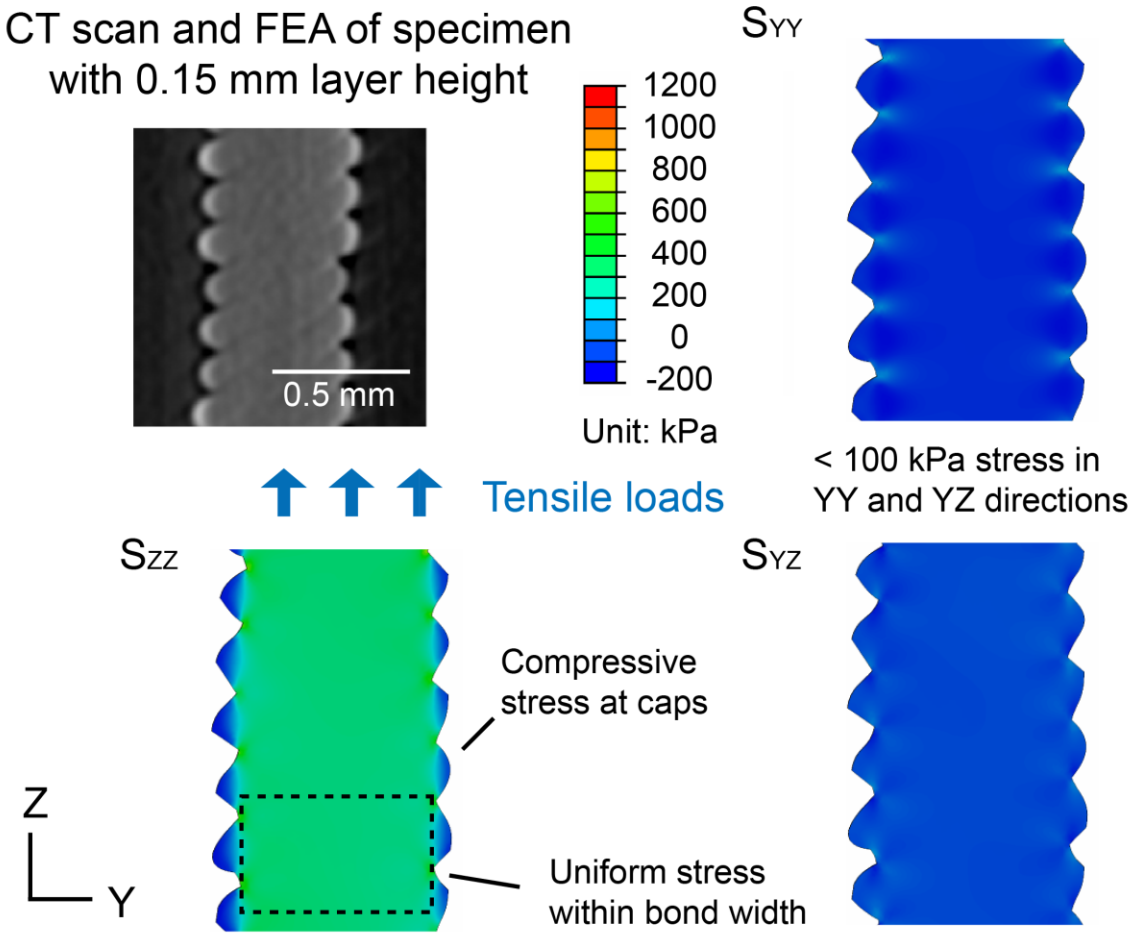

Figure 5.5: Finite element simulation of tensile tests along the transverse direction of specimen with 0.15 mm layer height. The stress distribution within a piece of specimen is illustrated.

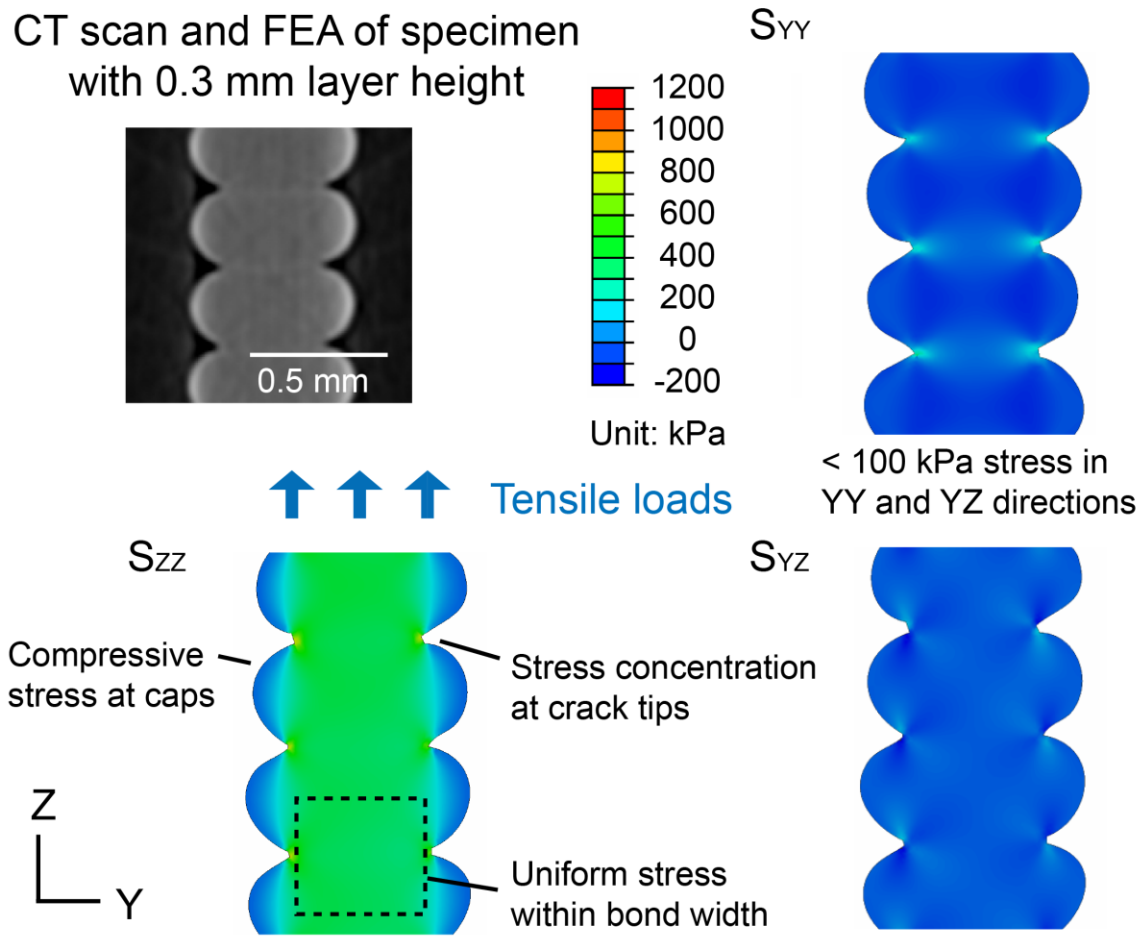

Figure 5.6: Finite element simulation of tensile tests along the transverse direction of specimen with 0.3 mm layer height. The stress distribution within a piece of specimen is illustrated.

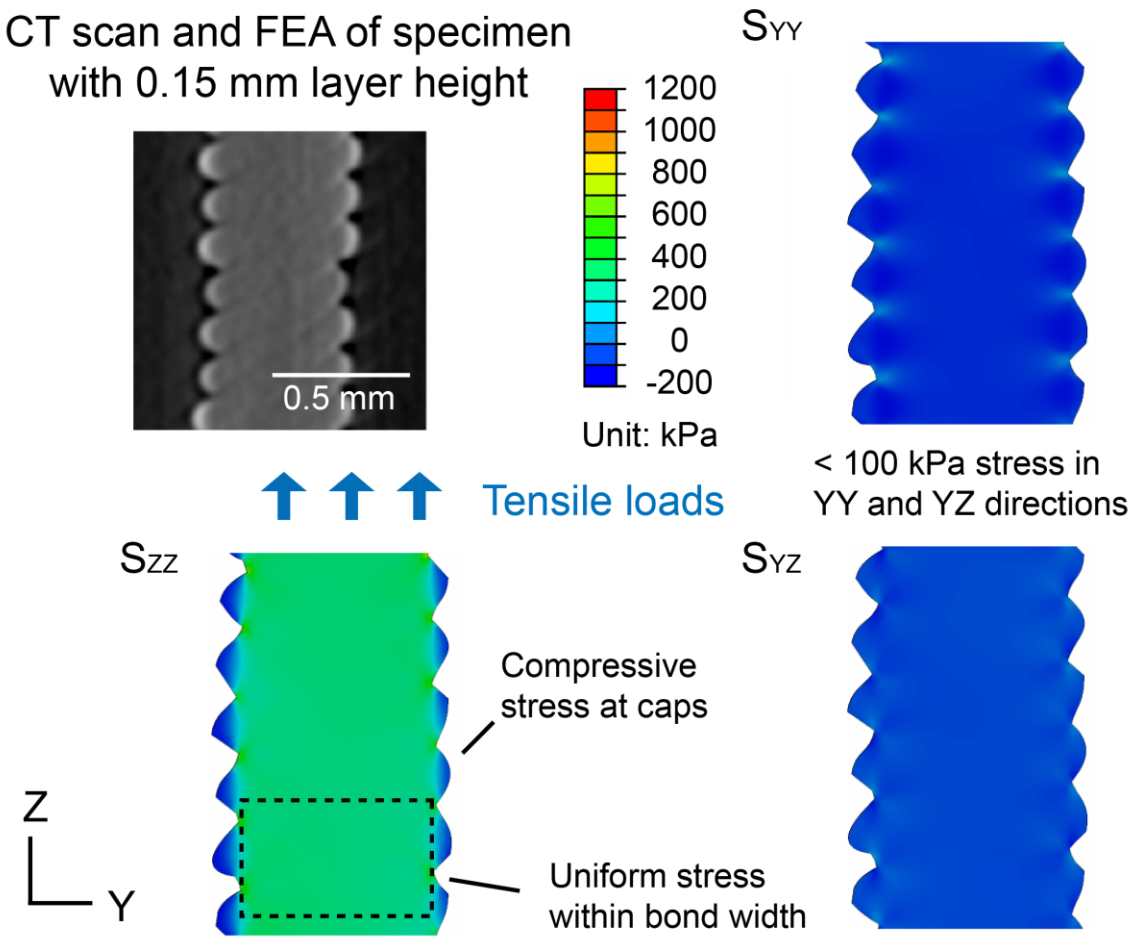

Figure 5.7: Finite element simulation of tensile tests along the transverse direction of specimen with 0.45 mm layer height. The stress distribution within a piece of specimen is illustrated.

For more quantitative analysis of the finite element results, we extracted the stress distribution across the cross-section of the models, as Figure 5.8 shows. The number at left indicates the nodal number; the number at right is the normal stress S_{ZZ} (in kPa) at the corresponding location.

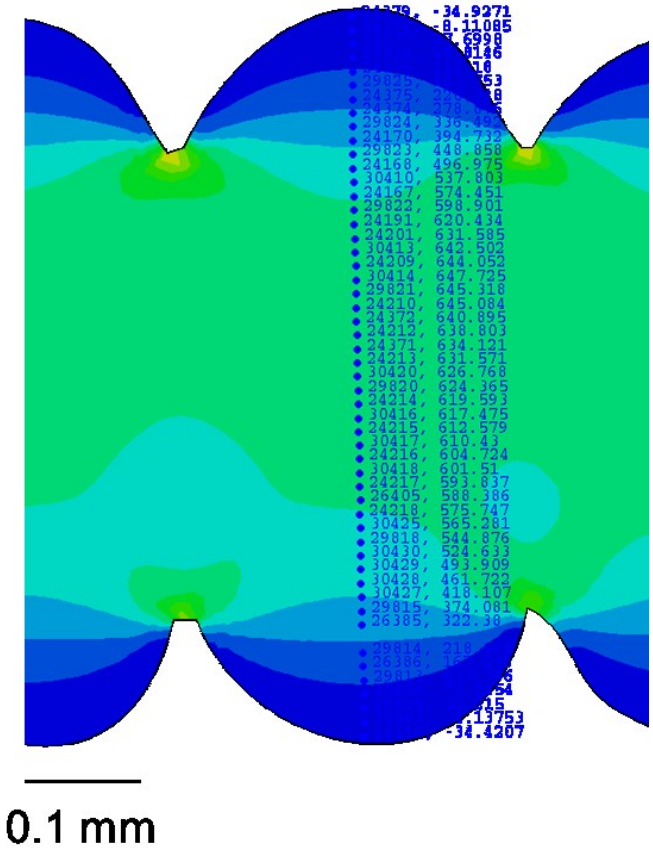

Figure 5.8: Extracted normal stress along a section.

For all three layer heights that have been simulated, the cross-sectional stress distributions were plotted in Figure 5.9. We could see that the cap region has much lower, sometimes even negative normal stress, while the central area has higher and more uniform normal stress. If integrating across the cap regions, we found that the cap region can provide an average of 30 % of loading-bearing capability (29.1 % for 0.15 mm, 30.7 % for 0.3 mm, 30.6 % for 0.45 mm). From this finding, we proposed the method of 'bond + 30 % cap width' for estimation of the effective Young's modulus in the following section.

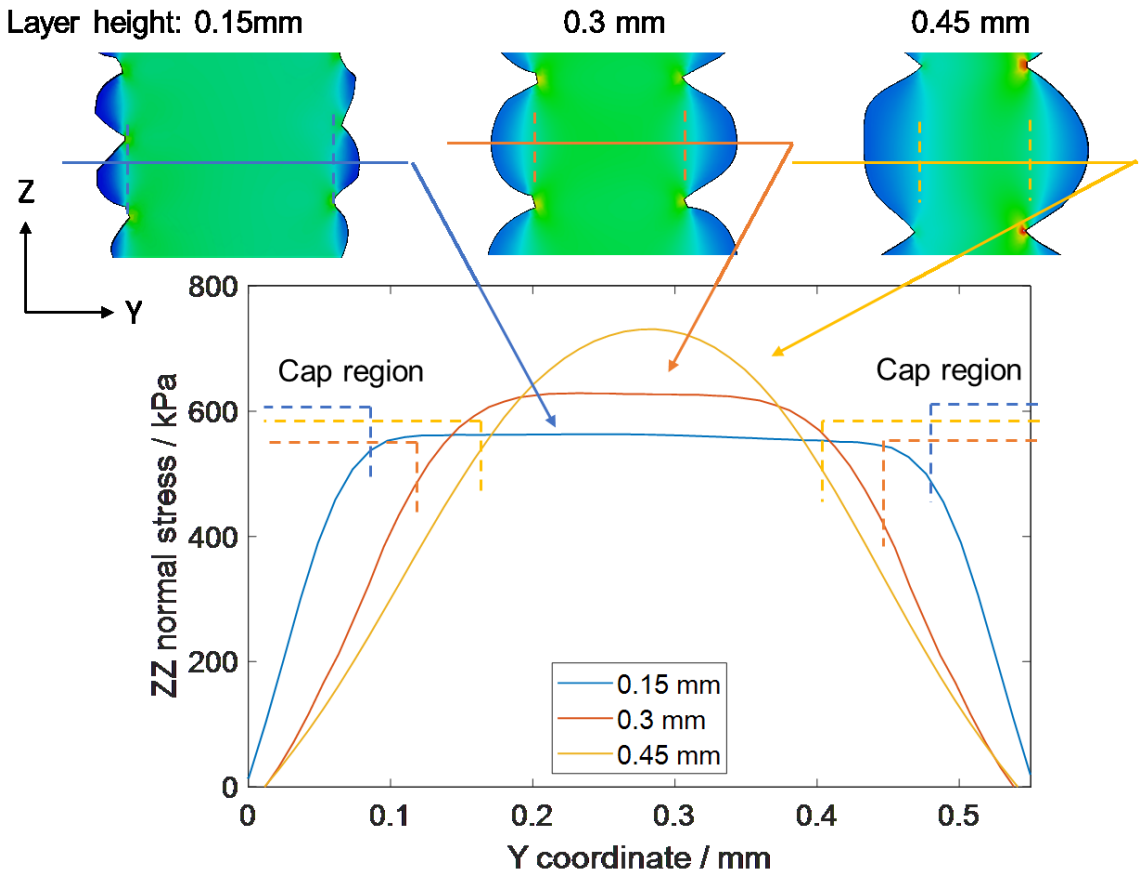

Figure 5.9: Extracted normal stress along sections of different specimens.

5.4 Estimation Approaches

Based on the analysis of stress distribution, multiple methods could be proposed to estimate the effective Young's modulus of the 3D-printed specimens by linking the overall mechanical performance with dimensions of specimens and material intrinsic modulus, as shown in Table 5.2.

Table 5.2: Description of proposed estimation methods.

Method	Nominal width	Wall width	Bond width	Analytical averaging	Bond width + 30 % cap width
Equation of Effective Young's modulus	$E_{effective} = E$	$E_{effective} = w_w E/w_n$	$E_{effective} = w_b E/w_n$	$E_{effective} = \int w(z)E/w_n \, dz$	$E_{effective} = (w_b + 0.3*(w_w - w_b))E/w_n$

(E is the material intrinsic modulus of 1.82 GPa, w_n is the nominal width of 0.5 mm, w_b is the bond width, w_w is the wall width, cap width is w_w - w_b, while for the analytical averaging method, w(z) stands for the real width at each z location.)

Among these widths, the nominal width and the wall width are the easiest to obtain: the nominal width is simply the dimension in digital design while the wall width could be measured by a caliper. As the majority of the positive tensile normal stress S_{zz} would be distributed within the narrowest neck - bond width (Figures 5.5 - 5.7), it is natural to assume these regions make major contributions to the overall tensile properties. However, measuring the bond width is challenging in general settings, as it requires either sectioning or X-ray scanning. Another method would be discretizing the specimen into thin slices, then integrating slices. The key assumption here is each slice remains planar after deformation, and there is no shear or bending stress.

Finally, an alternative method is proposed with a factor based on the stress distribution results from numerical simulation: using bond width plus 0.3 times cap width, which is the difference between wall width and bond width. The additional 30 % of cap width accounts for the contribution of cap regions and gives a better estimation than simply using the bond width.

On the other hand, for longitudinal direction specimens, there is no significant change in their cross-section areas along the stretching direction, despite the less than 2 % variation brought by printer inaccuracy. As a result, their effective modulus could be simply calculated using the constant cross-section area. To be noted here, this creates anisotropic stiffness behavior in general FFF specimens. For larger-scale parts that have different raster angles, they should be considered and calculated as composites to get precise estimations.

5.5 Comparison between different methods

The comparison between different estimation methods are shown in Table 5.3 and Figure 5.10, where the effective modulus is estimated based on each method, and the measured value is denoted as solid blue dots. Generally, all methods work better at a thinner layer height (less geometry deviation), while at a thicker layer height, the errors are higher.

Table 5.3: Comparison of the estimated moduli for 0.45 mm layer height and the measured value (1.23 GPa ± 0.08 GPa). Deviation is calculated by (Estimation - Measurement) / Measurement * 100%.

Method	Nominal width	Wall width	Bond width	Analytical averaging	Bond width + 30 % cap width
Estimated modulus at l_h = 0.45 mm (GPa)	1.82 ± 0.05	2.27 ± 0.06	0.90 ± 0.02	1.76 ± 0.05	1.31 ± 0.04
Deviation (%)	+48.0	+84.6	-26.8	+43.1	+6.5

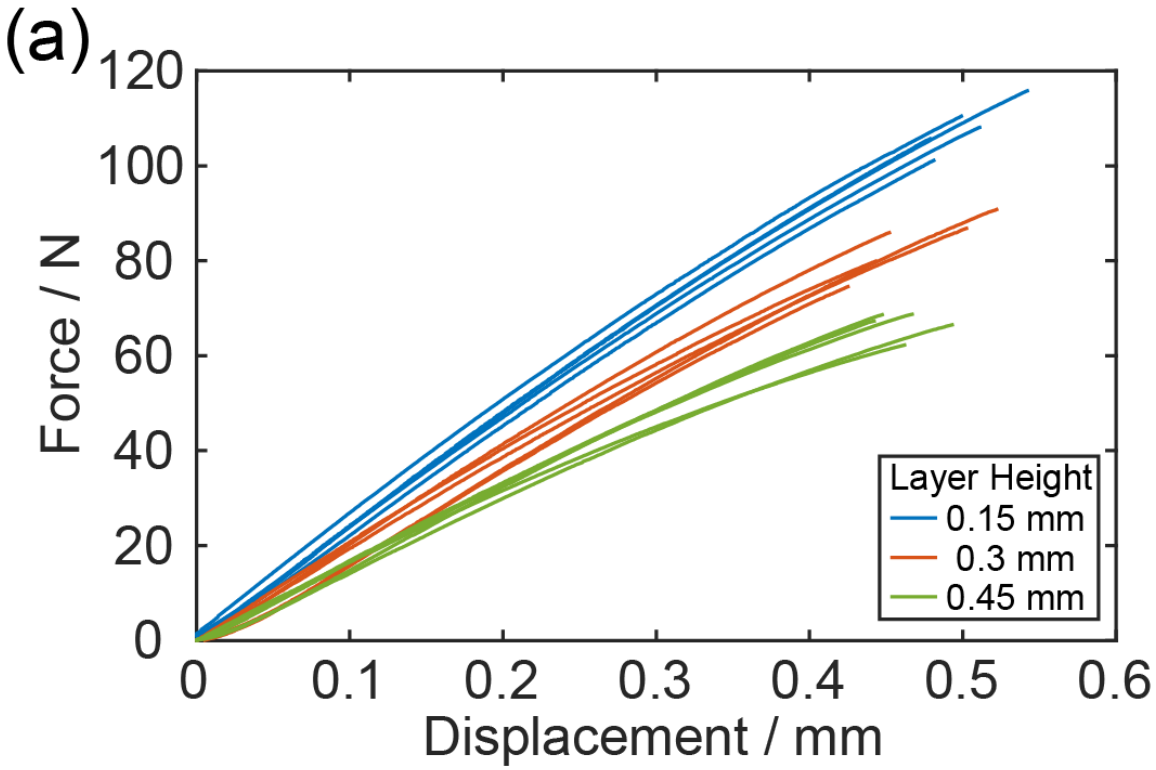
(a)
120
100
80
60
40
20
0
Force / N
0
0.1
0.2
0.3
0.4
0.5
0.6
Displacement / mm
Layer Height
0.15 mm
0.3 mm
0.45 mm

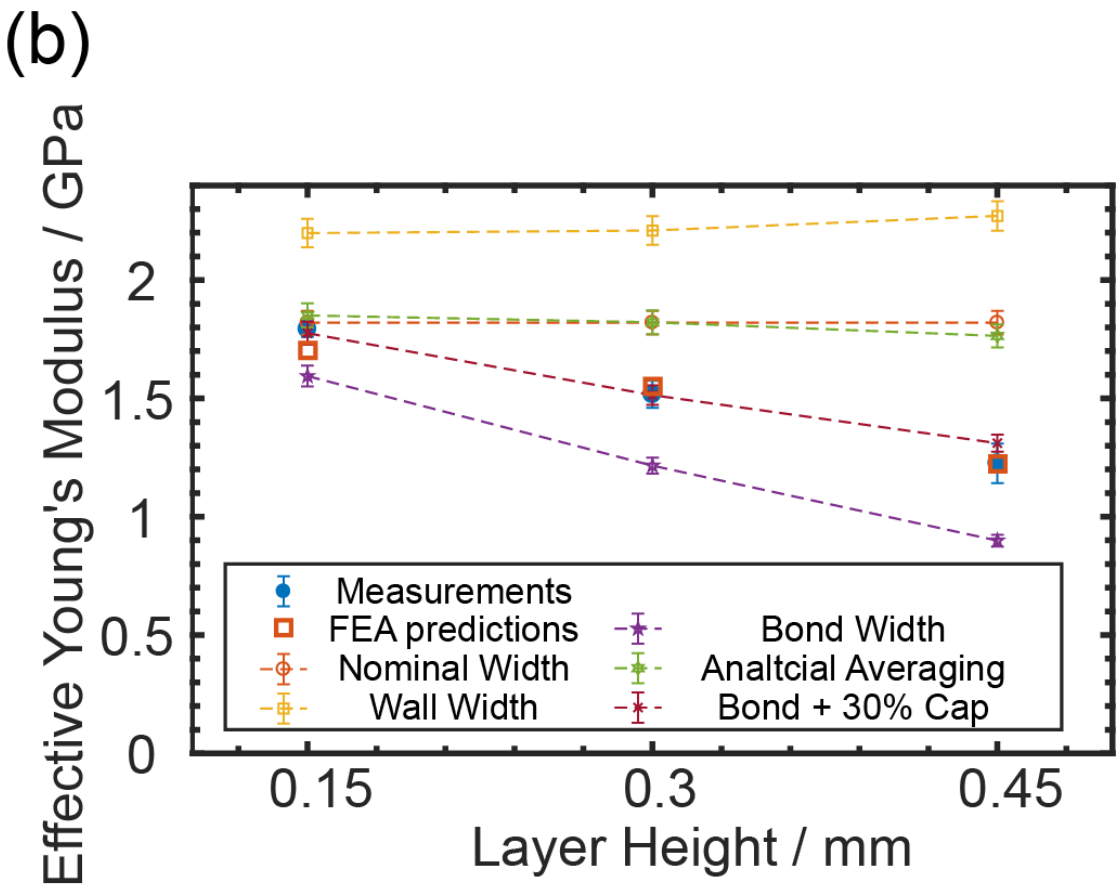
(b)
Effective Young's Modulus / GPa
2
1.5
1
0.5
0
0.15
0.3
0.45
Layer Height / mm
Measurements
FEA predictions
Nominal Width
Wall Width
Bond Width
Analtcial Averaging
Bond + 30% Cap

Figure 5.10: (a) The force-displacement relationships of transverse direction specimens with different layer heights. (b) The estimation of effective modulus using different methods, the experimentally measures values are denoted as solid blue dots.

Both nominal width and wall width overestimated the effective Young's modulus, as both options do not account for the narrower necks, which significantly reduces the load-bearing capability. For the bond width, though the simulation supports our hypothesis that the positive normal stress mainly distributes within the neck region, using bond width still underestimates the effective modulus. This means that the cap region has contributed to the effective modulus. Similarly, though simulation shows the stress in YY and YZ directions are small, there are still significant deviations between the analytical averaging method and experimental results. This suggests that the assumption of plane sections remain plane is not true: those small YY and YZ stresses still affect the overall load-bearing capability.

Finally, the proposed method based on the bond width and wall width could give a good and consistent estimation throughout all tested layer heights, and it is the only method that has less than 10 % deviation. From this result, we learned that while the bond width contributes most to the load-bearing capability, the cap region can still hold around 30 % modulus compared to a solid cubic part with the same dimensions. To get an accurate estimation, both regions need to be counted. What is more, since the relationship between intrinsic modulus, geometry, and effective modulus is found, we can also estimate the intrinsic modulus from the exterior dimension and effective modulus of printed specimens,

which will be helpful when there is a big change in intrinsic modulus before and after printing.

5.6 Chapter Summary

In summary, we performed finite element analysis to find the relationship between material intrinsic modulus, printed geometry, and the overall effective modulus. From the inspiration given by the simulated stress distribution, we also proposed an empirical method to estimate the effective Young's modulus of the specimens prepared by fused filament fabrication. The effective Young's modulus is calculated from the material intrinsic modulus value and the exterior dimensions of printed specimens. The empirical method shows good estimation accuracy with less than 10 % error for three different tested layer heights. Though the empirical factor could vary from case to case, since the layer-by-layer structure is widely found in extrusion-based additive manufacturing (EAM) parts, the approach of using FEA to analyze the stress distribution could be applied to other EAM methods to estimate the effective Young's modulus of specimens with non-uniform cross-section areas.

Chapter 6 : Summary and Outlook

6.1 Summary of this Work

In this work, we have used a combination of analytical, numerical, and experimental approaches to investigate the key factors that determine the FFF printing quality. Through the study, we have found:

- In different testing directions, the failure mode changed from slow fracture (longitudinal) to fast fracture (transverse). SEM images revealed the different levels of plasticity formed across the fracture surfaces, which resulted in the fracture mode change.
- When layer height increased, the bonding area was reduced, which in return caused reductions in transverse tensile strength and Young's modulus. The strength and modulus change were correlated with geometry changes quantified with micro-CT scan results: the strength showed a simple linear relationship with the bonding area within the measured conditions, while the modulus change is more complex but still could be explained by finite element simulations. To be noted, decreasing layer height will also increase printing time. So, there is a tradeoff between quality and speed.
- When changing the nozzle temperature, no significant geometrical difference was found. However, for transverse tensile strength, a minimum threshold of 250 °C was observed to reach maximum strength. This is attributed to the difference in

welding time, which leads to the different welding quality. If the welding is fully developed, further increasing the temperature is not expected to change the strength.

- When increasing print speed, there could be periodical geometry variations in printed width, while it did not influence mechanical performance within the range that we tested, since the cross-section area did not change.
- Using the micro-CT data, we could intentionally tune the flow index to compensate for machine-related errors and get better dimensional accuracy.
- When increasing environmental temperature, a smaller thermal gradient was detected within the specimen right after printing. Hence, there was less warping and deflection of the specimen off of the build plate. An analytical model based on the Timoshenko beam theory was proposed to estimate the deflection, while the adhesion between specimen and build plate still makes some discrepancies. Overall, to reduce warping, we recommend increasing environmental temperature rather than adding glues, since the remaining thermal stress may cause delamination defects.
- When increasing environmental humidity, PC absorbed more water and generated more porosity during printing, which in return reduced the as-printed specimen's mechanical performance. Meanwhile, an increase in ductility was observed in the transverse direction as the water content further increased and reached 0.15 wt%. Overall, drying filaments before printing is always recommended, reducing environmental humidity to less than 30 % RH is also recommended for long printing jobs (> 1 h).

Besides the direct influences of printing conditions, we also performed FEA to study the relationship between material intrinsic modulus, printed geometry, and the specimen's overall effective Young's modulus. From the FEA results, we proposed a simple and reliable approach to determine the effective Young's modulus. Based on scanned geometry from micro-CT, this simulation-inspired approach could compensate for the non-uniform cross-section geometry and give an accurate estimation of the effective Young's modulus with a < 10 % error. The same CT scan - FEA - stress analysis approach could possibly be extended to other printers and printing technologies as well.

Overall, we envision that our findings can contribute to providing guidelines for the selection of printing parameters to improve or customize printing quality, as well as expand the understanding of the FFF process. Our experimental data may also serve as benchmark data for future thermo-mechanical simulation models.

6.2 Future Directions

Our work may open new directions for studying the FFF process. Firstly, more fundamental investigations of the underlying mechanism could be very helpful. For example:

- Understanding the interactions between the extruded filament and previously deposited material: modeling the chain entanglement and weld development so that people could predict the minimal time and temperature needed to get a fully bonded interface.

- Developing numerical models that either consider or can predict the imperfection during the printing process, like the ‘waviness’ defects observed when varying print speed.
- Characterizing the fracture behaviors with more experimental tools, for example, using a high-speed camera to capture the crack propagation during transverse direction tests.
- Modeling the printing process with considerations of the surrounding air, accounting for the thermal conduction and convection during printing, which can give a more accurate estimation of the thermal history.
- Modeling the process of water diffusing into the polymer and generating pores during printing, especially for the nano-pores that were not discussed in this study. This also requires the involvement of more advanced experimental techniques, like in-situ nano-CT.

Next, our current study focused on the geometry of a single extrudate wide wall. Future studies could include larger-scale samples, where raster angle, infill density, and tool path will play more important roles. The raster angle can bring in more anisotropy, while a proper tool path may reduce the anisotropy. Infill density will introduce structural porosity, which can impact the as-printed mechanical properties. Besides the mechanical side, the geometry change will influence thermal stress and water absorption rate, which makes the environmental factors having more complex effects on printing quality.

Furthermore, FFF supports more materials other than the PC. While for other materials, people may need to consider more physical and chemical properties like crystallinity,

which highly depends on thermal history. Also, some polymers are more sensitive to humidity, while others are not. For advanced applications of printing composite filaments, studying the interactions between different materials is also required: How will they weld together? What could be the effects of strain mismatch as they have different coefficients of thermal expansion?

Finally, the overall objective of the NSF DMREF project, is the creation of a multi-physics multi-scale numerical model to fully account for the printed polymer's behavior from multiple aspects, including solid mechanics, polymer dynamics, and molecular and chain dynamics. We hope our study could provide solid experimental foundations for such numerical studies.

Bibliography

[1] "Editor's pick: 3D printing: you read it here first | New Scientist." https://www.newscientist.com/letter/mg23230991-100-1-editors-pick-3d-printing-you-read-it-here-first/ (accessed Feb. 26, 2020).

[2] H. Kodama, "Automatic method for fabricating a three-dimensional plastic model with photo-hardening polymer," *Review of Scientific Instruments*, vol. 52, no. 11, pp. 1770–1773, Nov. 1981, doi: 10.1063/1.1136492.

[3] W. E. Masters, "United States Patent: 4665492 - Computer automated manufacturing process and system," 4665492, May 12, 1987.

[4] C. W. Hull, "Apparatus for production of three-dimensional objects by stereolithography," US4575330A, Mar. 11, 1986.

[5] H. Bikas, P. Stavropoulos, and G. Chryssolouris, "Additive manufacturing methods and modelling approaches: a critical review," *Int J Adv Manuf Technol*, vol. 83, no. 1, pp. 389–405, Mar. 2016, doi: 10.1007/s00170-015-7576-2.

[6] 14:00-17:00, "ISO/ASTM 52900:2015," *ISO*. https://www.iso.org/cms/render/live/en/sites/isoorg/contents/data/standard/06/96/69669.html (accessed Feb. 26, 2020).

[7] B. Brenken, E. Barocio, A. Favaloro, V. Kunc, and R. B. Pipes, "Fused filament fabrication of fiber-reinforced polymers: A review," *Additive Manufacturing*, vol. 21, pp. 1–16, May 2018, doi: 10.1016/j.addma.2018.01.002.

[8] Hod Lipson and M. Kurman, “Fabricated: The New World of 3D Printing | Wiley,” *Wiley.com*. https://www.wiley.com/en-us/Fabricated%3A+The+New+World+of+3D+Printing-p-9781118350638 (accessed Feb. 26, 2020).

[9] S. Ahn, M. Montero, D. Odell, S. Roundy, and P. K. Wright, “Anisotropic material properties of fused deposition modeling ABS,” *Rapid Prototyping Journal*, vol. 8, no. 4, pp. 248–257, Jan. 2002, doi: 10.1108/13552540210441166.

[10] R. Anitha, S. Arunachalam, and P. Radhakrishnan, “Critical parameters influencing the quality of prototypes in fused deposition modelling,” *Journal of Materials Processing Technology*, vol. 118, no. 1, pp. 385–388, Dec. 2001, doi: 10.1016/S0924-0136(01)00980-3.

[11] K. Chin Ang, K. Fai Leong, C. Kai Chua, and M. Chandrasekaran, “Investigation of the mechanical properties and porosity relationships in fused deposition modelling-fabricated porous structures,” *Rapid Prototyping Journal*, vol. 12, no. 2, pp. 100–105, Jan. 2006, doi: 10.1108/13552540610652447.

[12] Q. Sun, G. M. Rizvi, C. T. Bellehumeur, and P. Gu, “Effect of processing conditions on the bonding quality of FDM polymer filaments,” *Rapid Prototyping Journal*, vol. 14, no. 2, pp. 72–80, Jan. 2008, doi: 10.1108/13552540810862028.

[13] M. Spoerk *et al.*, “Polypropylene Filled With Glass Spheres in Extrusion-Based Additive Manufacturing: Effect of Filler Size and Printing Chamber Temperature,” *Macromol. Mater. Eng.*, vol. 303, no. 7, p. 1800179, Jul. 2018, doi: 10.1002/mame.201800179.

[14] J. E. Seppala, S. H. Han, K. E. Hillgartner, C. S. Davis, and K. B. Migler, "Weld formation during material extrusion additive manufacturing," *Soft Matter*, vol. 13, no. 38, pp. 6761–6769, Oct. 2017, doi: 10.1039/C7SM00950J.

[15] T. J. Coogan and D. O. Kazmer, "Bond and part strength in fused deposition modeling," *Rapid Prototyping Journal*, vol. 23, no. 2, pp. 414–422, Jan. 2017, doi: 10.1108/RPJ-03-2016-0050.

[16] A. K. Sood, R. K. Ohdar, and S. S. Mahapatra, "Parametric appraisal of mechanical property of fused deposition modelling processed parts," *Materials & Design*, vol. 31, no. 1, pp. 287–295, Jan. 2010, doi: 10.1016/j.matdes.2009.06.016.

[17] F. Rayegani and G. C. Onwubolu, "Fused deposition modelling (FDM) process parameter prediction and optimization using group method for data handling (GMDH) and differential evolution (DE)," *Int J Adv Manuf Technol*, vol. 73, no. 1, pp. 509–519, Jul. 2014, doi: 10.1007/s00170-014-5835-2.

[18] D. Popescu, A. Zapciu, C. Amza, F. Baciu, and R. Marinescu, "FDM process parameters influence over the mechanical properties of polymer specimens: A review," *Polymer Testing*, vol. 69, pp. 157–166, Aug. 2018, doi: 10.1016/j.polymertesting.2018.05.020.

[19] G. C. Onwubolu and F. Rayegani, "Characterization and Optimization of Mechanical Properties of ABS Parts Manufactured by the Fused Deposition Modelling Process," *International Journal of Manufacturing Engineering*, 2014. https://www.hindawi.com/journals/ijme/2014/598531/ (accessed Feb. 27, 2020).

[20] I. Durgun and R. Ertan, “Experimental investigation of FDM process for improvement of mechanical properties and production cost,” *Rapid Prototyping Journal*, vol. 20, no. 3, pp. 228–235, 2014, doi: 10.1108/RPJ-10-2012-0091.

[21] S. Ziemian, M. Okwara, and C. W. Ziemian, “Tensile and fatigue behavior of layered acrylonitrile butadiene styrene,” *Rapid Prototyping Journal*, vol. 21, no. 3, pp. 270–278, Jan. 2015, doi: 10.1108/RPJ-09-2013-0086.

[22] A. W. Fatimatuzahraa, B. Farahaina, and W. A. Y. Yusoff, “The effect of employing different raster orientations on the mechanical properties and microstructure of Fused Deposition Modeling parts,” in *2011 IEEE Symposium on Business, Engineering and Industrial Applications (ISBEIA)*, Sep. 2011, pp. 22–27, doi: 10.1109/ISBEIA.2011.6088811.

[23] S. Mahmood, A. J. Qureshi, K. L. Goh, and D. Talamona, “Tensile strength of partially filled FFF printed parts: experimental results,” *Rapid Prototyping Journal*, vol. 23, no. 1, pp. 122–128, Jan. 2017, doi: 10.1108/RPJ-08-2015-0115.

[24] Agnes Bagsik and Volker Schöppner, “MECHANICAL PROPERTIES OF FUSED DEPOSITION MODELING PARTS MANUFACTURED WITH ULTEM*9085,” in *ANTEC 2011, Boston*, 2011, p. 5.

[25] J. Zhang, X. Z. Wang, W. W. Yu, and Y. H. Deng, “Numerical investigation of the influence of process conditions on the temperature variation in fused deposition modeling,” *Materials & Design*, vol. 130, pp. 59–68, Sep. 2017, doi: 10.1016/j.matdes.2017.05.040.

[26] K. Jud, H. H. Kausch, and J. G. Williams, “Fracture mechanics studies of crack healing and welding of polymers,” *J Mater Sci*, vol. 16, no. 1, pp. 204–210, Jan. 1981, doi: 10.1007/BF00552073.

[27] D. B. Kline and R. P. Wool, “Polymer welding relations investigated by a lap shear joint method,” *Polymer Engineering & Science*, vol. 28, no. 1, pp. 52–57, 1988, doi: 10.1002/pen.760280109.

[28] K. W. Allen, “Polymer interfaces: structure and strength, Richard P. Wool. Carl Hanser Verlag, Munich, Vienna, New York, 1995. pp. xvii + 494, price DM 178.00, £72.00. ISBN 3-446-16140-6,” *Polymer International*, vol. 38, no. 3, pp. 305–306, 1995, doi: 10.1002/pi.1995.210380314.

[29] K. R. Hart, R. M. Dunn, J. M. Sietins, C. M. Hofmeister Mock, M. E. Mackay, and E. D. Wetzel, “Increased fracture toughness of additively manufactured amorphous thermoplastics via thermal annealing,” *Polymer*, vol. 144, pp. 192–204, May 2018, doi: 10.1016/j.polymer.2018.04.024.

[30] A. R. Zekavat, A. Jansson, J. Larsson, and L. Pejryd, “Investigating the effect of fabrication temperature on mechanical properties of fused deposition modeling parts using X-ray computed tomography,” *Int J Adv Manuf Technol*, vol. 100, no. 1, pp. 287–296, Jan. 2019, doi: 10.1007/s00170-018-2664-8.

[31] C. McIlroy and P. D. Olmsted, “Disentanglement effects on welding behaviour of polymer melts during the fused-filament-fabrication method for additive manufacturing,” *Polymer*, vol. 123, pp. 376–391, Aug. 2017, doi: 10.1016/j.polymer.2017.06.051.

[32] Marco Galvani and Mark Robbins, “ffect of Chain Alignment and Entanglements on Thermal Welding in Fused Filament Fabrication,” in *Bulletin of the American Physical Society*, vol. Volume 65, Number 1, Accessed: Mar. 27, 2020. [Online]. Available: http://meetings.aps.org/Meeting/MAR20/Session/F34.7.

[33] Vijay. B. Nidagundi, R. Keshavamurthy, and C. P. S. Prakash, “Studies on Parametric Optimization for Fused Deposition Modelling Process,” *Materials Today: Proceedings*, vol. 2, no. 4, pp. 1691–1699, Jan. 2015, doi: 10.1016/j.matpr.2015.07.097.

[34] M. Montero, S. Roundy, D. Odell, S.-H. Ahn, and P. K. Wright, “Material Characterization of Fused Deposition Modeling (FDM) ABS by Designed Experiments,” p. 21, 2001.

[35] X. Wang, L. Zhao, J. Y. H. Fuh, and H. P. Lee, “Effect of Porosity on Mechanical Properties of 3D Printed Polymers: Experiments and Micromechanical Modeling Based on X-ray Computed Tomography Analysis,” *Polymers*, vol. 11, no. 7, p. 1154, Jul. 2019, doi: 10.3390/polym11071154.

[36] H. Xia, J. Lu, S. Dabiri, and G. Tryggvason, “Fully resolved numerical simulations of fused deposition modeling. Part I: fluid flow,” *Rapid Prototyping Journal*, vol. 24, no. 2, pp. 463–476, Jan. 2018, doi: 10.1108/RPJ-12-2016-0217.

[37] J. Yin, C. Lu, J. Fu, Y. Huang, and Y. Zheng, “Interfacial bonding during multi-material fused deposition modeling (FDM) process due to inter-molecular diffusion,” *Materials & Design*, vol. 150, pp. 104–112, Jul. 2018, doi: 10.1016/j.matdes.2018.04.029.

[38] S. F. Costa, F. M. Duarte, and J. A. Covas, “Thermal conditions affecting heat transfer in FDM/FFE: a contribution towards the numerical modelling of the process,” *Virtual and Physical Prototyping*, Dec. 2014, Accessed: Feb. 19, 2020. [Online]. Available: https://www.tandfonline.com/doi/abs/10.1080/17452759.2014.984042.

[39] T.-M. Wang, J.-T. Xi, and Y. Jin, “A model research for prototype warp deformation in the FDM process,” *Int J Adv Manuf Technol*, vol. 33, no. 11, pp. 1087–1096, Aug. 2007, doi: 10.1007/s00170-006-0556-9.

[40] L. Xinhua, L. Shengpeng, L. Zhou, Z. Xianhua, C. Xiaohu, and W. Zhongbin, “An investigation on distortion of PLA thin-plate part in the FDM process,” *Int J Adv Manuf Technol*, vol. 79, no. 5, pp. 1117–1126, Jul. 2015, doi: 10.1007/s00170-015-6893-9.

[41] S. Xiaoyong, C. Liangcheng, M. Honglin, G. Peng, B. Zhanwei, and L. Cheng, “Experimental Analysis of High Temperature PEEK Materials on 3D Printing Test,” in *2017 9th International Conference on Measuring Technology and Mechatronics Automation (ICMTMA)*, Changsha, China, Jan. 2017, pp. 13–16, doi: 10.1109/ICMTMA.2017.0012.

[42] S. Martin *et al.*, “The consequences of different printing chamber temperatures in extrusion-based additive manufacturing,” in *International Conference on Polymers and Moulds Innovations-PMI 2018*, Institute of Polymers and Composites, University of Minho, Portugal, 2018, p. 6.

[43] A. E. Costa, A. Ferreira da Silva, and O. Sousa Carneiro, “A study on extruded filament bonding in fused filament fabrication,” *Rapid Prototyping Journal*, vol. 25, no. 3, pp. 555–565, Jan. 2019, doi: 10.1108/RPJ-03-2018-0062.

[44] A. Armillotta, M. Bellotti, and M. Cavallaro, “Warpage of FDM parts: Experimental tests and analytic model,” *Robotics and Computer-Integrated Manufacturing*, vol. 50, pp. 140–152, Apr. 2018, doi: 10.1016/j.rcim.2017.09.007.

[45] O. A. Mohamed, S. H. Masood, and J. L. Bhowmik, “Optimization of fused deposition modeling process parameters: a review of current research and future prospects,” *Adv. Manuf.*, vol. 3, no. 1, pp. 42–53, Mar. 2015, doi: 10.1007/s40436-014-0097-7.

[46] H. E. Bair, G. E. Johnson, and R. Merriweather, “Water sorption of polycarbonate and its effect on the polymer’s dielectric behavior,” *Journal of Applied Physics*, vol. 49, no. 10, p. 4976, 1978, doi: 10.1063/1.324443.

[47] M. M. Qayyum and J. R. White, “Effect of water absorption and temperature gradients on polycarbonate injection moldings,” *Journal of Applied Polymer Science*, vol. 43, no. 1, pp. 129–144, Jul. 1991, doi: 10.1002/app.1991.070430111.

[48] E. Ito and Y. Kobayashi, “Changes in physical properties of polycarbonate by absorbed water,” *Journal of Applied Polymer Science*, vol. 22, no. 4, pp. 1143–1149, 1978, doi: 10.1002/app.1978.070220423.

[49] M. Narkis, L. Nicolais, A. Apicella, and J. P. Bell, “Hot water aging of polycarbonate,” *Polymer Engineering & Science*, vol. 24, no. 3, pp. 211–217, 1984, doi: 10.1002/pen.760240308.

[50] C. Li, Y. Zhang, and Y. Zhang, “Boiling water aging of polycarbonate and polycarbonate/acrylonitrile–butadiene–styrene resin and polycarbonate/low-density polyester blends,” *Journal of Applied Polymer Science*, vol. 89, no. 3, pp. 589–595, 2003, doi: 10.1002/app.11825.

[51] S. N. A. M. Halidi and J. Abdullah, “Moisture effects on the ABS used for Fused Deposition Modeling rapid prototyping machine,” in *2012 IEEE Symposium on Humanities, Science and Engineering Research*, Jun. 2012, pp. 839–843, doi: 10.1109/SHUSER.2012.6268999.

[52] E. Kim, Y.-J. Shin, and S.-H. Ahn, “The effects of moisture and temperature on the mechanical properties of additive manufacturing components: fused deposition modeling,” *Rapid Prototyping Journal*, vol. 22, no. 6, pp. 887–894, Jan. 2016, doi: 10.1108/RPJ-08-2015-0095.

[53] A. P. Valerga, M. Batista, J. Salguero, and F. Girot, “Influence of PLA Filament Conditions on Characteristics of FDM Parts,” *Materials*, vol. 11, no. 8, p. 1322, Aug. 2018, doi: 10.3390/ma11081322.

[54] H. Li *et al.*, “Bonding quality and fracture analysis of polyamide 12 parts fabricated by fused deposition modeling,” *Rapid Prototyping Journal*, vol. 23, no. 6, pp. 973–982, Jan. 2017, doi: 10.1108/RPJ-03-2016-0033.

[55] C. Ziemian, M. Sharma, and S. Ziemian, “Anisotropic Mechanical Properties of ABS Parts Fabricated by Fused Deposition Modelling,” *Mechanical Engineering*, Apr. 2012, [Online]. Available: https://digitalcommons.bucknell.edu/fac_books/72.

[56] J. C. Riddick, M. A. Haile, R. V. Wahlde, D. P. Cole, O. Bamiduro, and T. E. Johnson, “Fractographic analysis of tensile failure of acrylonitrile-butadiene-styrene

fabricated by fused deposition modeling," *Additive Manufacturing*, vol. 11, pp. 49–59, Jul. 2016, doi: 10.1016/j.addma.2016.03.007.

[57] R. Hashemi Sanatgar, C. Campagne, and V. Nierstrasz, "Investigation of the adhesion properties of direct 3D printing of polymers and nanocomposites on textiles: Effect of FDM printing process parameters," *Applied Surface Science*, vol. 403, pp. 551–563, May 2017, doi: 10.1016/j.apsusc.2017.01.112.

[58] J. Kotlinski, "Mechanical properties of commercial rapid prototyping materials," *Rapid Prototyping Journal*, vol. 20, no. 6, pp. 499–510, Jan. 2014, doi: 10.1108/RPJ-06-2012-0052.

[59] C. S. Davis, K. E. Hillgartner, S. H. Han, and J. E. Seppala, "Mechanical strength of welding zones produced by polymer extrusion additive manufacturing," *Additive Manufacturing*, vol. 16, pp. 162–166, Aug. 2017, doi: 10.1016/j.addma.2017.06.006.

[60] T. Letcher, B. Rankouhi, and S. Javadpour, "Experimental Study of Mechanical Properties of Additively Manufactured ABS Plastic as a Function of Layer Parameters," presented at the ASME 2015 International Mechanical Engineering Congress and Exposition, Mar. 2016, doi: 10.1115/IMECE2015-52634.

[61] M. Bertoldi, M. Yardimci, C. M. Pistor, S. I. Guceri, and G. Sala, "Mechanical Characterization of Parts Processed via Fused Deposition," 1998, doi: http://dx.doi.org/10.26153/tsw/646.

[62] B. M. Tymrak, M. Kreiger, and J. M. Pearce, "Mechanical properties of components fabricated with open-source 3-D printers under realistic environmental conditions,"

Materials & Design, vol. 58, pp. 242–246, Jun. 2014, doi: 10.1016/j.matdes.2014.02.038.

[63] A. Lanzotti, M. Grasso, G. Staiano, and M. Martorelli, "The impact of process parameters on mechanical properties of parts fabricated in PLA with an open-source 3-D printer," *Rapid Prototyping Journal*, vol. 21, no. 5, pp. 604–617, Jan. 2015, doi: 10.1108/RPJ-09-2014-0135.

[64] C. E. Duty *et al.*, "Structure and mechanical behavior of Big Area Additive Manufacturing (BAAM) materials," *Rapid Prototyping Journal*, vol. 23, no. 1, pp. 181–189, Jan. 2017, doi: 10.1108/RPJ-12-2015-0183.

[65] X. Deng, Z. Zeng, B. Peng, S. Yan, and W. Ke, "Mechanical Properties Optimization of Poly-Ether-Ether-Ketone via Fused Deposition Modeling," *Materials*, vol. 11, no. 2, p. 216, Feb. 2018, doi: 10.3390/ma11020216.

[66] T. Webbe Kerekes, H. Lim, W. Y. Joe, and G. J. Yun, "Characterization of process–deformation/damage property relationship of fused deposition modeling (FDM) 3D-printed specimens," *Additive Manufacturing*, vol. 25, pp. 532–544, Jan. 2019, doi: 10.1016/j.addma.2018.11.008.

[67] S.-I. Park, D. W. Rosen, S. Choi, and C. E. Duty, "Effective mechanical properties of lattice material fabricated by material extrusion additive manufacturing," *Additive Manufacturing*, vol. 1–4, pp. 12–23, Oct. 2014, doi: 10.1016/j.addma.2014.07.002.

[68] J. F. Rodriguez, J. P. Thomas, and J. E. Renaud, "Characterization of the mesostructure of fused-deposition acrylonitrile-butadiene-styrene materials," *Rapid Prototyping Journal*, vol. 6, no. 3, pp. 175–186, Jan. 2000, doi: 10.1108/13552540010337056.

[69] A. Boschetto and L. Bottini, “Design for manufacturing of surfaces to improve accuracy in Fused Deposition Modeling,” *Robotics and Computer-Integrated Manufacturing*, vol. 37, pp. 103–114, Feb. 2016, doi: 10.1016/j.rcim.2015.07.005.

[70] A. Boschetto and L. Bottini, “Accuracy prediction in fused deposition modeling,” *Int J Adv Manuf Technol*, vol. 73, no. 5, pp. 913–928, Jul. 2014, doi: 10.1007/s00170-014-5886-4.

[71] B. N. Turner and S. A. Gold, “A review of melt extrusion additive manufacturing processes: II. Materials, dimensional accuracy, and surface roughness,” *Rapid Prototyping Journal*, vol. 21, no. 3, pp. 250–261, Jan. 2015, doi: 10.1108/RPJ-02-2013-0017.

[72] J. P. Kruth, M. Bartscher, S. Carmignato, R. Schmitt, L. De Chiffre, and A. Weckenmann, “Computed tomography for dimensional metrology,” *CIRP Annals*, vol. 60, no. 2, pp. 821–842, Jan. 2011, doi: 10.1016/j.cirp.2011.05.006.

[73] S. ASHLEY, “Rapid prototyping for artificial body parts,” *Mech. eng. (N.Y. N.Y., 1919)*, vol. 115, no. 5, pp. 50–53, 1993.

[74] E. Berry *et al.*, “Preliminary experience with medical applications of rapid prototyping by selective laser sintering,” *Medical Engineering & Physics*, vol. 19, no. 1, pp. 90–96, Jan. 1997, doi: 10.1016/S1350-4533(96)00039-2.

[75] H. Taud, R. Martinez-Angeles, J. F. Parrot, and L. Hernandez-Escobedo, “Porosity estimation method by X-ray computed tomography,” *Journal of Petroleum Science and Engineering*, vol. 47, no. 3, pp. 209–217, Jun. 2005, doi: 10.1016/j.petrol.2005.03.009.

[76] D. Rouholamin and N. Hopkinson, “Understanding the efficacy of micro-CT to analyse high speed sintering parts,” *Rapid Prototyping Journal*, vol. 22, no. 1, pp. 152–161, Jan. 2016, doi: 10.1108/RPJ-03-2014-0030.

[77] G. Kerckhofs *et al.*, “The Combined Use of Micro-CT Imaging, In-Situ Loading and Non-Rigid Image Registration for 3D Experimental Local Strain Mapping on Porous Bone Tissue Engineering Scaffolds under Compressive Loading,” p. 10.

[78] A. du Plessis, I. Yadroitsev, I. Yadroitsava, and S. G. Le Roux, “X-Ray Microcomputed Tomography in Additive Manufacturing: A Review of the Current Technology and Applications,” *3D Printing and Additive Manufacturing*, vol. 5, no. 3, pp. 227–247, Jul. 2018, doi: 10.1089/3dp.2018.0060.

[79] H. Nouri, S. Guessasma, and S. Belhabib, “Structural imperfections in additive manufacturing perceived from the X-ray micro-tomography perspective,” *Journal of Materials Processing Technology*, vol. 234, pp. 113–124, Aug. 2016, doi: 10.1016/j.jmatprotec.2016.03.019.

[80] S. A. Tronvoll, N. P. Vedvik, C. W. Elverum, and T. Welo, “A new method for assessing anisotropy in fused deposition modeled parts using computed tomography data,” *Int J Adv Manuf Technol*, vol. 105, no. 1, pp. 47–65, Nov. 2019, doi: 10.1007/s00170-019-04081-7.

[81] R. K. Chen, T. T. Lo, L. Chen, and A. J. Shih, “Nano-CT Characterization of Structural Voids and Air Bubbles in Fused Deposition Modeling for Additive Manufacturing,” presented at the ASME 2015 International Manufacturing Science and Engineering Conference, Sep. 2015, doi: 10.1115/MSEC2015-9462.

[82] H. Villarraga, C. Lee, T. Corbett, J. A. Tarbutton, and S. T. Smith, “ASSESSING ADDITIVE MANUFACTURING PROCESSES WITH X-RAY CT METROLOGY,” vol. 6, p. 6.

[83] J. Soete, B. Badoux, Y. Swolfs, L. Gorbatikh, and M. Wevers, “Defect detection in 3D printed carbon fibre composites using X-ray Computed Tomography,” in *https://www.ndt.net/article/ctc2019/papers/iCT2019_Full_paper_62.pdf*, Feb. 2019, pp. 1–8, Accessed: Feb. 26, 2020. [Online]. Available: https://lirias.kuleuven.be/2372579.

[84] S. Guessasma, S. Belhabib, and H. Nouri, “Significance of pore percolation to drive anisotropic effects of 3D printed polymers revealed with X-ray μ-tomography and finite element computation,” *Polymer*, vol. 81, pp. 29–36, Dec. 2015, doi: 10.1016/j.polymer.2015.10.041.

[85] Z. Quan *et al.*, “Microstructural characterization of additively manufactured multi-directional preforms and composites via X-ray micro-computed tomography,” *Composites Science and Technology*, vol. 131, pp. 48–60, Aug. 2016, doi: 10.1016/j.compscitech.2016.05.015.

[86] S. Yu, Y. H. Hwang, J. Y. Hwang, and S. H. Hong, “Analytical study on the 3D-printed structure and mechanical properties of basalt fiber-reinforced PLA composites using X-ray microscopy,” *Composites Science and Technology*, vol. 175, pp. 18–27, May 2019, doi: 10.1016/j.compscitech.2019.03.005.

[87] Michael D. Hayes, Dale B. Edwards, and Anand R. Shah, *Fractography in Failure Analysis of Polymers*. Elsevier, 2015.

[88] T. J. Coogan and D. O. Kazmer, “Modeling of interlayer contact and contact pressure during fused filament fabrication,” *Journal of Rheology*, vol. 63, no. 4, pp. 655–672, Jun. 2019, doi: 10.1122/1.5093033.

[89] Paul C. Hiemenz and Timothy P. Lodge, *Polymer Chemistry*. CRC Press, 2007.

[90] J. E. Seppala and K. D. Migler, “Infrared thermography of welding zones produced by polymer extrusion additive manufacturing,” *Additive Manufacturing*, vol. 12, pp. 71–76, Oct. 2016, doi: 10.1016/j.addma.2016.06.007.

[91] E. T. J. Klompen, “Mechanical properties of solid polymers : constitutive modelling of long and short term behaviour,” Technische Universiteit Eindhoven, 2005.

[92] Wang C. M., “Timoshenko Beam-Bending Solutions in Terms of Euler-Bernoulli Solutions,” *Journal of Engineering Mechanics*, vol. 121, no. 6, pp. 763–765, Jun. 1995, doi: 10.1061/(ASCE)0733-9399(1995)121:6(763).

[93] C. W. Lim, C. M. Wang, and S. Kitipornchai, “Timoshenko curved beam bending solutions in terms of Euler-Bernoulli solutions,” *Arch. Appl. Mech.*, vol. 67, no. 3, pp. 179–190, Feb. 1997, doi: 10.1007/s004190050110.

[94] C.-L. Tsai and C.-C. Lin, “Diffusion in a Solid Cylinder Part I: Advancing Model,” *Journal of Marine Science and Technology*, vol. 23, no. 2, pp. 133–141, Apr. 2015, doi: 10.6119/JMST-014-0117-1.

[95] J.D. Dymond, K.N. Marsh, and R.C. Wilhoit, *Virial Coefficients of Pure Gases and Mixtures*. Springer, 2003.

[96] F. Peng, B. D. Vogt, and M. Cakmak, “Complex flow and temperature history during melt extrusion in material extrusion additive manufacturing,” *Additive*

Manufacturing, vol. 22, pp. 197–206, Aug. 2018, doi: 10.1016/j.addma.2018.05.015.

[97] P. G. Kusalik, F. Liden, and I. M. Svishchev, "Calculation of the third virial coefficient for water," *The Journal of Chemical Physics*, vol. 103, no. 23, pp. 10169–10175, Dec. 1995, doi: 10.1063/1.469919.

[98] A. H. Harvey and E. W. Lemmon, "Correlation for the Second Virial Coefficient of Water," *Journal of Physical and Chemical Reference Data*, vol. 33, no. 1, pp. 369–376, Mar. 2004, doi: 10.1063/1.1587731.

[99] D. R. Cox and D. Oakes, *Analysis of Survival Data*. CRC Press, 1984.

[100] R. J. Gardner and J. R. Martin, "Humid aging of plastics: Effect of molecular weight on mechanical properties and fracture morphology of polycarbonate," *Journal of Applied Polymer Science*, vol. 24, no. 5, pp. 1269–1280, 1979, doi: 10.1002/app.1979.070240512.

Vita

Lichen Fang was born in Beijing, China on October 14th, 1992 to parents Shuishun Fang and Xiaodan Zhang. Lichen graduated from the High School Affiliated to Renmin University of China in 2011 and attended Tsinghua University to study Engineering Mechanics. In 2014 he spent half a year in Harvard University as a student researcher, and later he earned his Bachelor of Engineering degree in 2015. After spending 23 years in Beijing, in August 2015 he moved to Baltimore to join the Department of Mechanical Engineering and Hopkins Extreme Materials Institute at Johns Hopkins University, for his doctoral study under the advice of Professor Sung Hoon Kang. In May 2018 he earned his Master of Science in Engineering degree and continued to pursue his Doctor of Philosophy degree in Mechanical Engineering, which is expected to be completed in May 2020. Lichen's research interests include architected functional materials, additive manufacturing, and finite element analysis.